AN ANISOTROPIC DAMAGE MECHANICS MODEL FOR CONCRETE WITH APPLICATIONS FOR FATIGUE LOADING AND FREEZE-THAW EFFECTS

A Thesis
Submitted to the Graduate Faculty
of the
North Dakota State University
of Agriculture and Applied Science

By

Andrew Steven Reberg

In Partial Fulfillment of the Requirements
for the Degree of
MASTER OF SCIENCE

Major Department:
Civil Engineering

May 2013

Fargo, North Dakota

North Dakota State University
Graduate School

Title

An Anisotropic Damage Mechanics Model for Concrete with Applications
for Fatigue Loading and Freeze-Thaw Effects

By

Andrew Steven Reberg

The Supervisory Committee certifies that this ***disquisition*** complies with North Dakota State University's regulations and meets the accepted standards for the degree of

MASTER OF SCIENCE

SUPERVISORY COMMITTEE:

Dr. Frank Yazdani
Chair

Dr. Mijia Yang

Dr. Magdy Abdelrahman

Dr. Jerry Gao

Approved:

05/10/2013	Dr. Eakalak Khan
Date	Department Chair

ABSTRACT

It is well known that the formation and propagation of microcracks within concrete is anisotropic in nature, and has a degrading effect on its mechanical performance. In this thesis an anisotropic damage mechanics model is formulated for concrete which can predict the behavior of the material subjected to monotonic loading, fatigue loading, and freeze-thaw cycles. The constitutive model is formulated using the general framework of the internal variable theory of thermodynamics. Kinetic relations are used to describe the directionality of damage accumulation and the associated softening of mechanical properties. The rate independent model is then extended to cover fatigue loading cycles and freeze-thaw cycles. Two simple softening functions are used to predict the mechanical properties of concrete as the number of cyclic loads as well as freeze-thaw cycles increases. The model is compared with experimental data for fatigue and freeze-thaw performance of plain concrete.

ACKNOWLEDGMENTS

I would like to thank my advisor, Dr. Frank Yazdani, for his wisdom, guidance, and for asking me to continue my education two years ago. Also, I want to express my appreciation to the other members of my graduate committee: Dr. Mijia Yang, Dr. Magdy Abdelrahman, and Dr. Jerry Gao for their constructive comments on this work. I would like to thank Mr. Ashkan Saboori for his help in compiling and formatting much of the experimental data used in this thesis. This work was partially supported by a DOT-MPC grant to the Department of Civil Engineering. The author is grateful for their support.

DEDICATION

I would like to dedicate this thesis to my parents, Steve and Renee Reberg, without whom I would not have tried to further my education as much as I have. Their love and support has been a constant in my life and has allowed me to pursue goals I would not have pursued otherwise.

TABLE OF CONTENTS

LIST OF TABLES

LIST OF FIGURES

CHAPTER 1. INTRODUCTION

Concrete is the most widely used material in the construction industry today. Its applications as a structural material, ease of production, and ecological benefits are several reasons it continues to be used in such vast quantities. It is used in buildings, bridges, roads, dams, tunnels, power plants and many other structures that are vital to our infrastructure. Despite our continuous use of concrete, our knowledge of its behavior is not yet as thorough as perhaps it should be. Researchers continue to search for effective ways to understand the complex behavior of concrete. With the use of the computers, constitutive models have been established that have given engineers an economic alternative to expensive experimental analysis of complex structures. Although there are existing models that describe the nonlinear behavior of concrete, none have gained common acceptance among researchers and engineers as they have some weaknesses and are continually being refined. Furthermore, structures are continually loaded and unloaded in what is termed “fatigue loading” which further complicates the behavior of concrete. The need for a simple and effective constitutive model that can be used to predict the behavior of concrete is apparent (Mehta and Monteiro, 1993).

Concrete has some unique mechanical behaviors that differ from other structural materials such as metals. It is much stronger in compression than it is in tension. Both the strength and the stiffness of concrete are affected by the loading condition to which it is subjected. Strength and stiffness properties may be enhanced if confining pressure is applied to the concrete. Concrete typically undergoes brittle failure, but the ductility of the material can also be enhanced in the presence of confining pressure.

Another unique characteristic of concrete is concrete's resistance to water with respect to corrosion. Although concrete is chemically resistant to water, it is highly susceptible to the infiltration of water into its voids and cracks. As water infiltrates concrete it can have the following effects: Corrosion of reinforcing steel, freeze-thaw damage, and chemical attack from various chemicals that are transported into the concrete by water. Of these effects, this paper will deal primarily with the effect the freeze-thaw process has on concrete. Water occupies 9% more volume when frozen than when it is in its liquid state. This moisture expansion causes internal stress on concrete and can cause damage to occur. As more damage occurs in the form of microcracks, the infiltration of moisture into the concrete can increase, which can further exacerbate the damage caused by the freeze-thaw process (Yang, 2004).

Concrete is considered a composite material because it is composed of an aggregate material that is dispersed within a cement paste matrix. Because of this unique makeup, concrete behaves different than an isotropic material such as metals. The nonlinear behavior of concrete is the result of two modes of irreversible changes that occur within the concrete matrix, microcracking and plastic flow. The propagation and formation of microcracks within concrete cause material bonds to be destroyed which results in increased material compliance. Because the propagation and formation of microcracks is highly dependent on the direction of loading, so is the reduction in the material stiffness. Continuum damage mechanics is used to describe the growth of microcracks within the concrete matrix. Unlike plasticity theory, which prior to continuum damage mechanics was the primary means of modeling the nonlinear behavior of concrete, damage mechanics illustrates the continual weakening of the "damaged" material. This weakening is shown in the form of reduced stiffness.

The second mode of irreversible change that occurs within concrete, termed “plastic flow”, is the dislocation of concrete that occurs along slip planes under internal shear stresses during loading. When the dislocation occurs along the slip plane it is assumed that, for the most part, the same amount of material bonds are destroyed and then again created, effectively allowing strain to occur, but not damaging the material in the sense that the material stiffness is reduced (Yazdani and Schreyer, 1988). This phenomenon can be modeled well by the theory of plasticity and is used in many existing concrete models today, though it is not considered in this paper as only uniaxial and biaxial stress spaces are considered. With these points in mind, it is appropriate to assume that a combined model, utilizing both plasticity theory and continuum damage mechanics should be used to describe the nonlinear behavior of concrete subjected to confining pressure as plastic flow is more prevalent in this case.

Although fracture mechanics has been used in modeling the behavior of concrete, it is not considered as appropriate as continuum damage mechanics prior to the formation of a major crack or fault zone. Fracture mechanics is based on the ability to know the amount of energy that is required for an existing crack to propagate, and is applied to concrete once a major crack forms (Yazdani, 1993). While some energy is dissipated during the propagation of an existing crack, the majority of energy is dissipated during the creation of new microcracks which is better described using continuum damage mechanics (Thapa, 2010). Recently there has been an effort by some researchers to combine continuum damage mechanics and fracture mechanics in the modeling of concrete.

In order to have a thorough understanding of the behavior of concrete for various loading conditions the mechanical behavior of concrete for uniaxial tension and compression, biaxial compression, biaxial tension, triaxial compression, fatigue loading, and freeze-thaw effects are discussed in Chapter 2. As this thesis is an extension of the Yazdani model (1993) and the Wen model (2011), they will be discussed in detail in Chapter 3 along with a review of some basic principles of thermodynamics and damage mechanics. The Yazdani model (1993) produced good correlation with experimental results for monotonic loading of concrete which is shown in Chapter 3. Chapter 4 deals with the thermodynamics of materials, which is the basis of the aforementioned models. In Chapters 5 and 6 a new model will be presented to model the fatigue and freeze-thaw behavior of concrete. A softening function will be used to manipulate the strength and compliance of concrete accordingly. This model will be compared with the experimental data presented in Chapter 2. Conclusions and future work will be discussed in Chapter 6, followed by a list of references.

Before continuing on it should be made clear that in the absence of the consideration of plastic flow, the model discussed in this paper deals with uniaxial and biaxial load cases. Biaxial stresses are common in engineering application and can range from a bridge deck to a nuclear containment structure. The model presented in this paper captures the essential characteristics of concrete in uniaxial and biaxial stress space.

CHAPTER 2. MECHANICAL BEHAVIOR OF CONCRETE

2.1. Introduction

Part of the difficulty of formulating a constitutive model for concrete is that it needs to capture the mechanical and phenomenological behavior of concrete under various loading conditions. A thorough understanding of the mechanical behavior of concrete is vital to the formulation of a comprehensive and robust model based on the theory of damage mechanics. To help in the formulation of a phenomenological model, the effects of microcracking need to be understood, as this is what damage mechanics ultimately involves. The direction of microcracking and eventually larger cracking is highly dependent on the direction of loading. Further, the extent of the cracking that occurs is greatly affected by the loading conditions the concrete is subjected to. This microcracking and plastic flow that occurs during the external loading is thought to be the cause of the nonlinear behavior of concrete. Though this paper does not go into detail discussing the plastic flow mechanisms it is considered to be negligible for loading with relatively low confining pressure.

Prior to the discussion of how concrete behaves under various loading conditions, it is important to know how microcracks progress within concrete. It is known that prior to any external loading, microcracks exist within the transition zone of concrete, also known as the aggregate mortar interface (Mehta and Monteiro, 1993; Dhir and Sangha, 1974). This preexisting damage is known to be caused by several things, namely shrinkage, thermal expansion, segregation, and volume changes. The onset of damage in concrete is initiated in the form of microcracking that can occur throughout the cement matrix. The first forms of microcracking are preexisting and will typically occur where concrete is the weakest, along the interface of the aggregate and the cement matrix. At a certain local stress level, the internal stress reaches a point at which the microcrack can propagate into the cement matrix. The cracks that occur or propagate into the cement matrix are stopped by the aggregate, which has the highest strength of the individual components that make up concrete. As loading increases, or the number of cycles increases in the case of fatigue loading, the microcracks continue to propagate and crack coupling occurs until a failure occurs on a macro scale.

In this chapter the mechanical behavior of concrete during uniaxial compression, uniaxial tension, biaxial compression, biaxial tension, triaxial compression, fatigue loading, and freeze-thaw effects will be discussed in detail. As stated before, it is vital to understand the differences in the mechanical behavior of concrete subjected to differing loading conditions in order to formulate a meaningful damage mechanics model for concrete. The water cement ratio, admixtures, type of aggregate, and cement type also have a large effect on the behavior and performance of concrete, but are not discussed in this study. The affects of these variables are considered to be captured in the experimental parameters used in this paper.

2.2. Plastic Flow vs. Microcracking

Prior to any investigation of the mechanical behavior of concrete subjected to various load paths, the two major sources of nonlinear stress-strain behavior need to be discussed. Plastic flow in aggregates and void closures is considered the primary form of inelastic deformation under loading conditions with relatively large confining pressures. An important feature of this type of deformation is that it does not affect the overall stiffness of the material. This is well demonstrated by the stress-strain curves of concrete loaded with hydrostatic pressure. The slope of the loading-unloading curve is relatively unchanged while large amounts of permanent deformation caused by plastic flow are observed. While this form of deformation demonstrates an increased ductility in concrete, it is neglected in this paper as the model presented is based on continuum damage mechanics theory and not plasticity theory.

The second source of nonlinear deformation behavior is known as microcracking and is best quantified by damage mechanics theory. While this is thought to be the more prevalent of the two forms of inelastic deformation in brittle materials, it is known to be nearly nonexistent during hydrostatic loading. Microcracking is termed "damage" in this paper and has a dramatic effect on the compliance of concrete. As microcracking accumulates in a particular direction (parallel to the direction of primary loading for concrete in compression; perpendicular to the direction of loading for concrete in tension) the stiffness in that direction decreases giving rise to increased strain, though this strain is thought to be recoverable upon unloading assuming complete crack closure (Yazdani and Karnawat, 1996).

While plastic flow is not considered in this paper; permanent deformations are quantified using kinematic relations. The permanent deformation is considered to be the result of imperfect crack closure and misfit surfaces. This aspect of the model will be discussed further in Chapters 3 and 4.

2.3. Uniaxial Compression

A stress-strain curve for a typical concrete specimen subjected to uniaxial monotonic compression is shown in Figure 2.1. One can divide the stress-strain curve into four major zones in the progression of microcracking in concrete. They occur at less than 30% of the maximum compressive strength (f'c), between 30% and 50% of f_c', between 50% and 75% of f_c', and greater than 75% of f_c' (Mehta and Monteiro, 1993). These stress levels are approximate but provide realistic boundaries for the various stages in the development of the microcracking phenomenon.

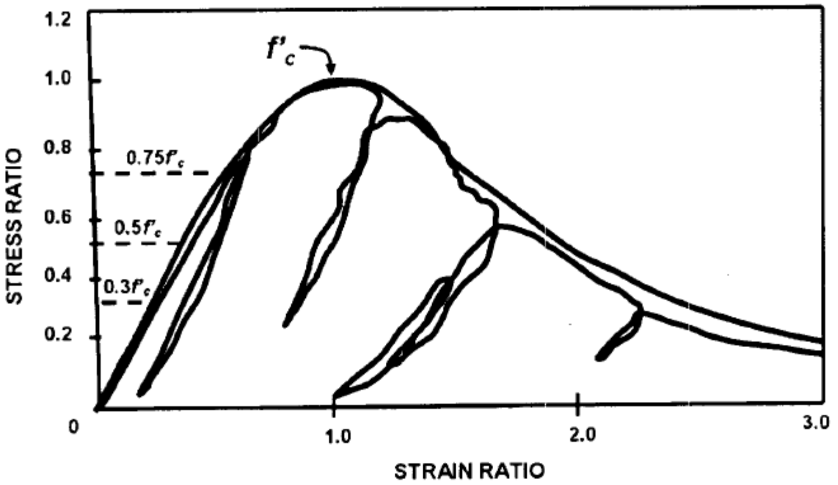

Fig. 2.1. Stress vs. axial strain for a concrete specimen loaded in uniaxial compression (Bahn and Hsu, 1998)

In the first stage of crack development, at stress levels less than 30% of the maximum compressive load, the preexisting microcracks are largely unaffected by loading. This can be seen in the stress-strain curve as it shows a nearly linear relationship between stress and axial strain at this load level. It can also be taken that the stress level within the concrete is not yet high enough for the preexisting cracks to propagate or for new cracks to form along the aggregate mortar interface. It is not until localized stress reaches 30% of f_c' that localized cracking begins occurring in the transition zone.

During the second stage of crack development, at stress levels between 30% and 50% of f_c', stress levels at cracks tips in the transition zone reach critical levels and begin to propagate. Also, new cracks begin to develop as the strength of the bond between aggregate and mortar matrix is reached. At this stage cracks within the mortar matrix are still insignificant as this region is stronger than the interface region. As more cracks form, stress redistribution occurs and the nonlinear stress-strain behavior of concrete begins.

The third stage of crack development occurs when stress levels are between 50% and 75% of f_c'. At this stage cracks begin to propagate and form in the mortar matrix. Cracks continue to develop on the aggregate-mortar interface and can become unstable. Stress redistribution continues to occur and as a result, the compliance of the concrete continues to increase.

The fourth stage occurs at stresses greater than 75% of f_c'. At this stage, the internal energy within the concrete is greater than the crack-release energy of the mortar. Cracks continue to propagate in the mortar and combine to form larger cracks. As crack formation becomes unstable there are decreases areas within the concrete for stress to be redistributed to. At this level of loading the cracks between the mortar and the transition zone can combine allowing for complete fracture of the concrete.

One will notice another unique behavior of concrete illustrated in Figure 2. When stresses reach a critical point, near 75% of f_c', crack propagation begins to reach an unstable rate. Until this point the volumetric strain has nearly a linear relationship with the applied stress. Once cracking reaches an unstable rate of propagation the lateral strain begins to increase rapidly which causes the volumetric strain curve to reverse as seen in Figure 2.2. This signifies that at this critical stress level the volumetric strain is at its maximum compressed state, after which the volume of the concrete begins to expand.

Another interesting note, well documented by Price (1951), is that under sustained stress conditions the maximum load concrete can endure may be less than the short term compressive strength f_c'. He found that at 90% of the short term compressive strength, the concrete specimen failed after one hour and at 75% it failed after 30 years.

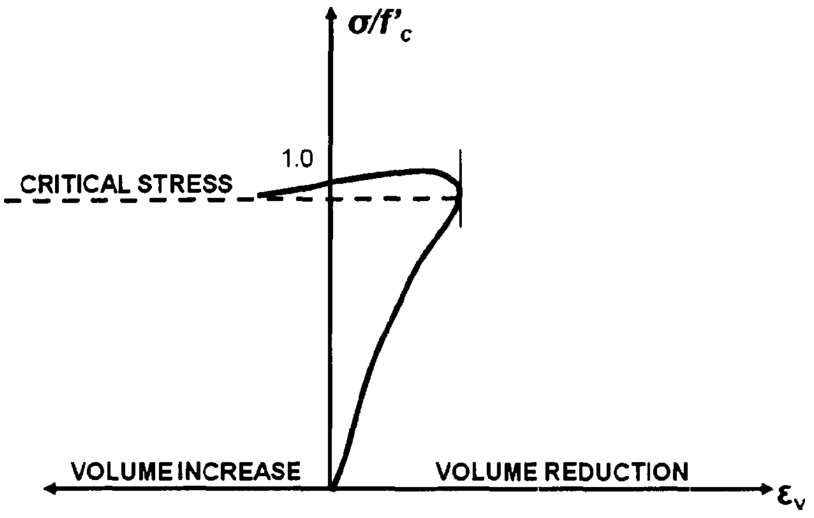

Fig. 2.2. Typical stress vs. volumetric strain plot of concrete subjected to uniaxial compression

For uniaxial compression of concrete, microcracking occurs approximately parallel to the direction of loading. Because of the shape of the aggregate within the concrete matrix, cracking occurs at a slight angle. Shear stresses occurring along the interface of cracks causes shear sliding and crack separation.

2.4. Uniaxial Tension

It is well known that concrete is much weaker in tension than it is in compression. The main reason for this is that the tensile strength of the aggregate-mortar interface is less than that of the mortar itself. This is because under a tensile load cracks are arrested much less frequently than when subjected to a compressive load. Where cracking occurs nearly parallel to the loading during for uniaxial compression, it occurs transverse to the loading direction for uniaxial tension. This means that the propagation or formation of new cracks dramatically reduces the available load-carrying area, which than causes stress increases near existing crack tips. As a result, failure of concrete occurs by bridging relatively few cracks, as opposed to many cracks as in uniaxial compression.

One can see in Figure 2.3 that the stress-strain behavior, and corresponding Poisson's ratio and elastic modulus, of concrete in uniaxial tension are similar to concrete in uniaxial compression. For stresses less than approximately 60% of the maximum tensile strength of concrete, f_t, the formation and propagation of cracks beyond the preexisting cracks is minimal and the stress-strain curve is nearly linear. As stresses reach 75% of f_t crack propagation becomes unstable. This unstable crack propagation can be seen in the increased compliance of the concrete at this load level. Once the maximum tensile strength of the concrete is reached the stress-strain curve often becomes erratic as brittle failure ensues (Mehta and Monteiro, 1993). Figure 3 shows the stress-strain curve for direct-tension testing of a concrete specimen performed by Shkolnik (2007). Various loading rates were used.

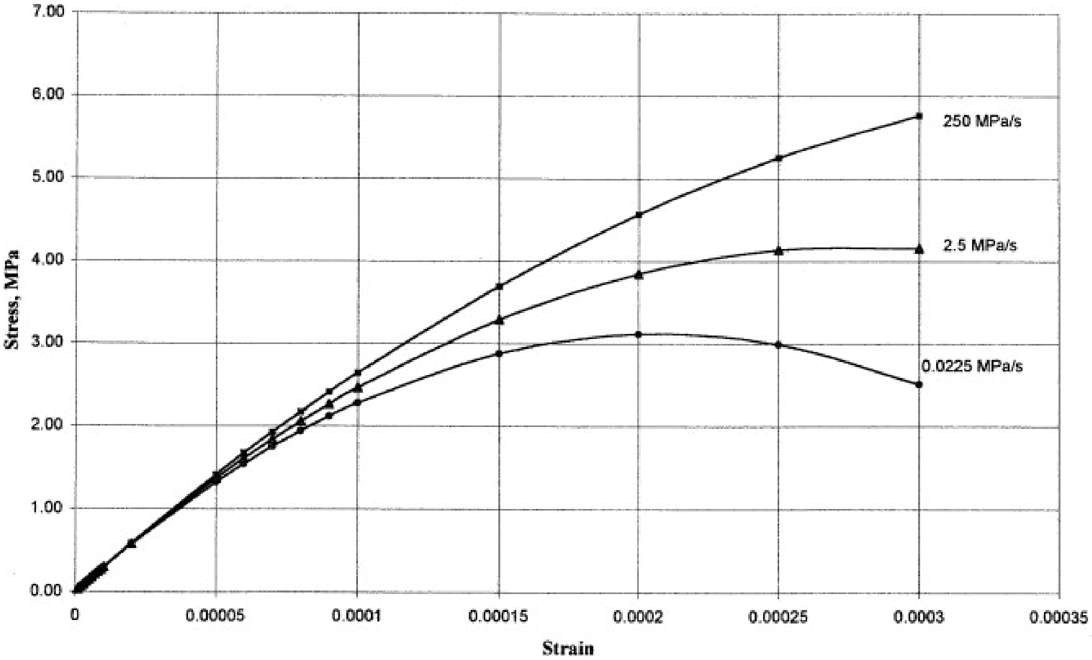

Fig. 2.3. Stress-strain curve for direct tension testing of concrete specimen with varying loading rates (Shkolnik, 2005)

In general, the maximum compressive strength of concrete is about 10 to 20 times that of its maximum tensile strength. Both the compressive and tensile strength of concrete can be affected by the preloading effect. The preloading effect takes place when concrete is subjected to at least one loading and unloading sequence in any direction. Given the concrete is loaded in compression or tension in a given direction, the strength of the concrete in the orthogonal direction is now reduced for the opposite type of loading (Thapa, 2010). For example, if a specimen is loaded vertically with a compressive load and then unloaded cracking will occur in the vertical direction. Now if the same specimen is loaded horizontally with a tensile load, the preexisting cracks in the vertical direction will reduce the tensile strength in the horizontal direction. In effect, the formation of damage within concrete is highly dependent on the direction of loading and is considered anisotropic. This is a unique and important characteristic that should be captured by an effective damage mechanics model for concrete.

2.5. Biaxial Compression

A biaxial stress state is essentially when concrete is being loaded in two orthogonal directions without the presence of confining pressure. This type of loading is very common in actual structural application. It is well documented that concrete's compressive strength can be enhanced during biaxial compression. This strength enhancement is dependent upon the biaxial stress ratio $\frac{\sigma_1}{\sigma_2}$. One can see from Figure 2.4 that concrete reaches its maximum strength, about 20% to 30% increase, when the biaxial load ratio $\frac{\sigma_1}{\sigma_2} = 0.5$. For equal biaxial loading the compressive strength still increased, but not as significantly as the strength for $\frac{\sigma_1}{\sigma_2} = 0.5$.

Another interesting note is that the overall shape of the curve in Figure 2.4 is not affected by the uniaxial compressive strength of the concrete.

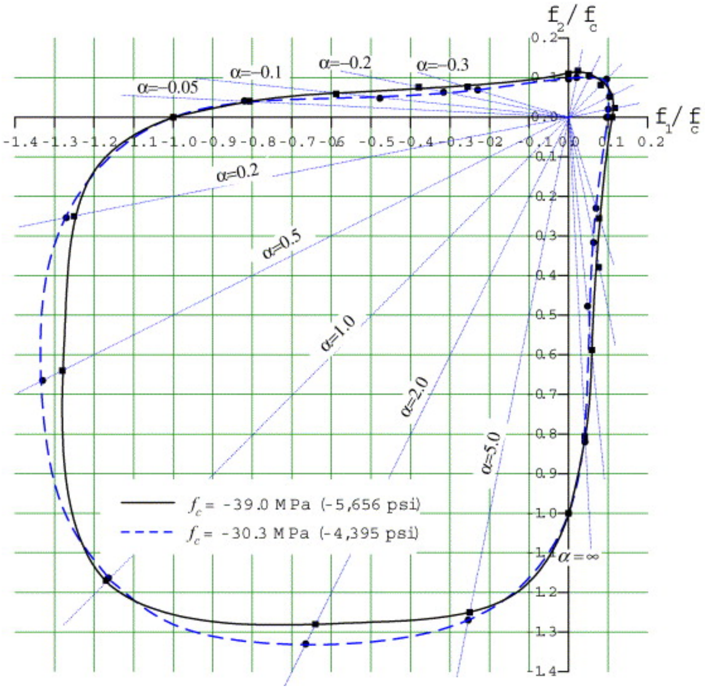

Fig. 2.4. Biaxial strength envelope of concrete (Lee et al., 2004)

If one thinks about the mode of cracking in concrete subjected to uniaxial compression, the strength enhancement provided by biaxial loading is logical. Compressive loading in one direction creates cracks the direction parallel to loading. These cracks propagate in an attempt to split open further as lateral strain increases. With the addition of a confining load in an orthogonal direction, at least some crack opening is prevented requiring larger loads for complete fracture to occur. This becomes even more evident during triaxial loading.

In addition to strength enhancement, concrete becomes more ductile in this stress state. Similar to the strength enhancement during biaxial loading, the maximum strain occurs at $\frac{\sigma_2}{\sigma_3} = 0.5$ while equal biaxial loading experiences some enhanced ductility it is not as great. The change in the stress-strain behavior can be seen in Figure 2.5 for varying load ratios.

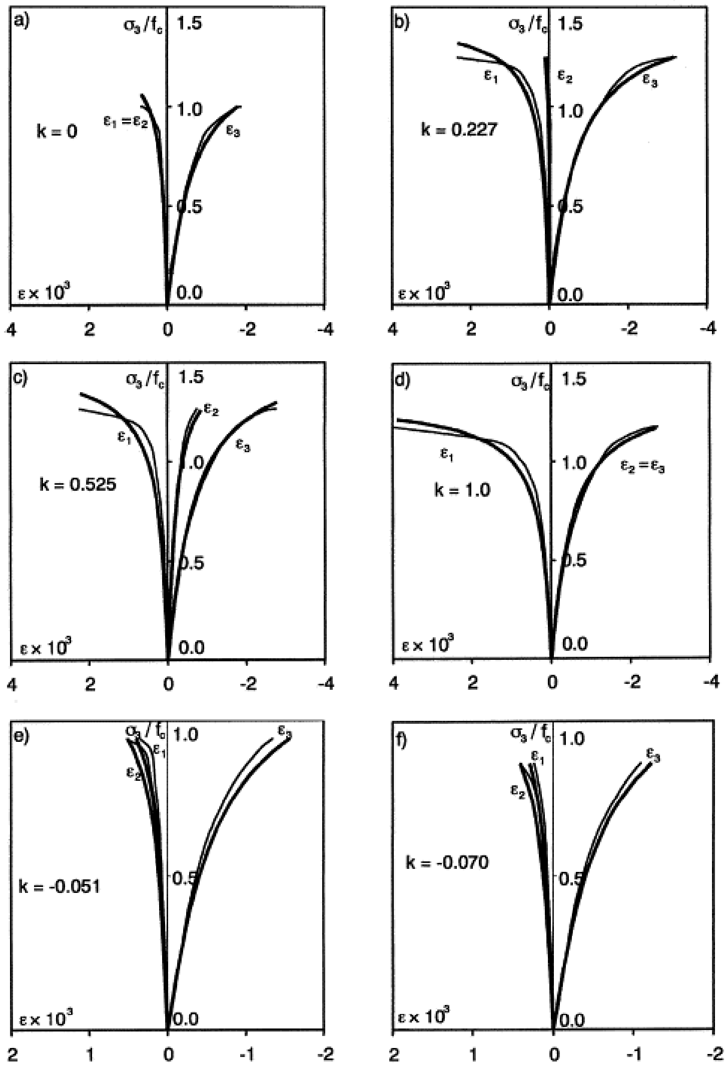

Fig. 2.5. Stress-strain curves for concrete subjected to various biaxial load ratios, $k = \frac{\sigma_2}{\sigma_3}$ (Litewka and Debinski, 2003)

2.6. Biaxial Tension

Concrete in biaxial tension is known to possess some interesting properties. Looking at the biaxial strength envelope shown in Figure 2.4, the strength of concrete is clearly affected by multi-axis tension loading. For equal biaxial loading the strength appears to be close to that of the uniaxial rupture strength of concrete, perhaps slightly less. Some strength enhancement is shown for proportional biaxial tension loading, with the largest increase in strength occurring at load proportions $\frac{\sigma_1}{\sigma_2} = 0.25$. At this point the strength of concrete can increase by as much as 5 to 10%.

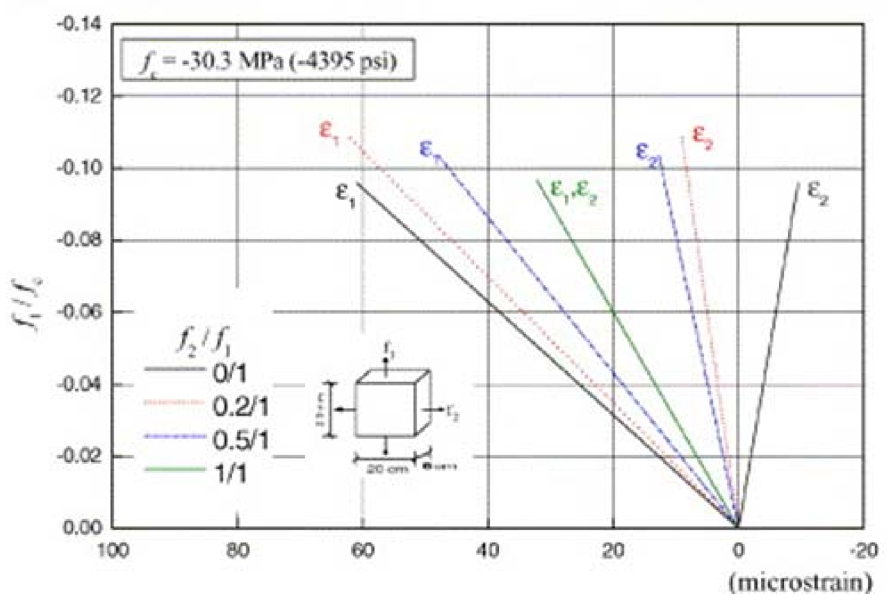

Fig. 2.6. Stress-strain curve for concrete in biaxial tension (Lee et al., 2004)

The strain behavior of concrete subjected to biaxial tension is shown in Figure 2.6. The figure shows nearly linear stress-strain behavior of concrete prior to rupture. This type of behavior is logical as little inelastic deformation will occur prior to failure of the material. Since microcrack propagation is not inhibited as in compression loading, they will quickly propagate into larger cracks that quickly lead to complete rupture of the specimen.

2.7. Triaxial Compression

A material that has loading applied in three orthogonal directions is considered to be triaxially loaded. In a laboratory environment a specimen is usually loaded with a certain confining pressure while being loaded with an additional axial load in one or two directions. Concrete subjected to triaxial compression loading can behave differently depending on the level of confining pressure that is being applied. Papanikolaou and Kappos (2007) performed triaxial compression tests on concrete at low to mid-level confining pressures, shown in Figure 2.7. Figure 2.8 shows a triaxial test with higher confining pressure. One can see that concrete behaves differently depending on the level of confining pressure used. For lower levels of confining pressure strain-softening is easily seen for the portion of the curve on the right side of the maximum load. Strain-softening is known as a decrease in the load carrying capacity of a material that coincides with an increase in strain. Strain-hardening is also prevalent in these curves. This is the portion of the stress-strain curve that consists of and increased rate of strain while the load carrying capacity continues to increase. This happens prior to the peak load being reached. At high levels of confining pressure concrete can fail by the crushing of the mortar rather than cleavage.

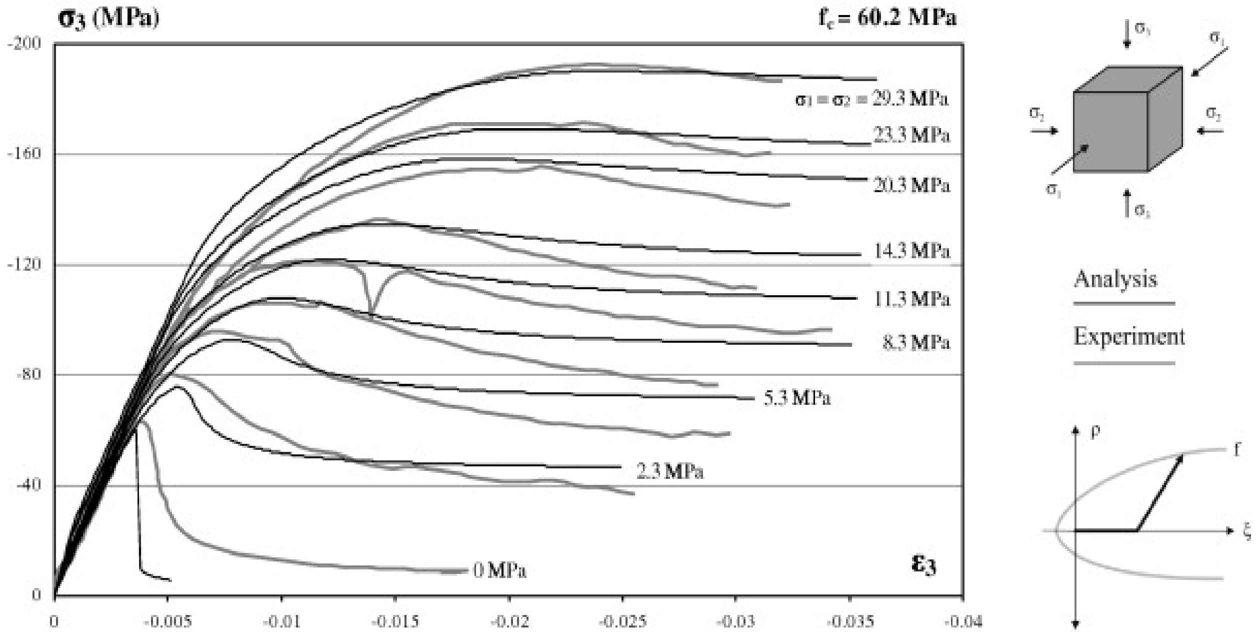

Fig. 2.7. Stress vs. strain plot for triaxial compression tests on concrete for low to mid-level confining pressures (Papanikolaou and Kappos, 2007)

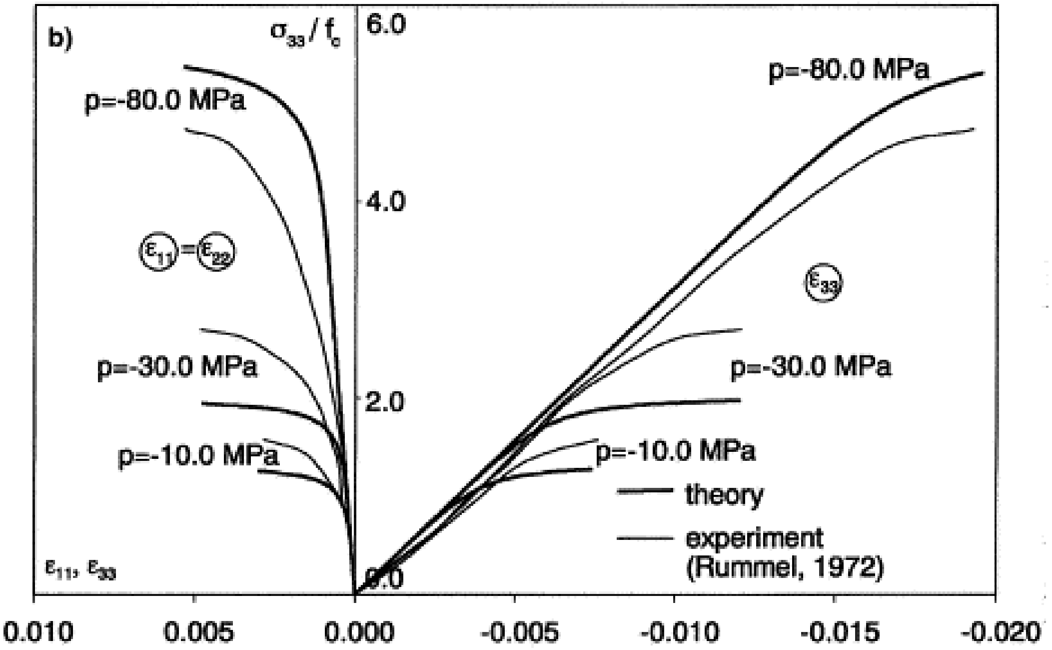

Fig. 2.8. Stress vs. strain plot for triaxial compression tests on concrete for larger confining pressure (Litewka and Debinski, 2003)

An important note should be made about concrete under pure hydrostatic pressure. Under this type of loading cracking in the concrete is considered to be minimal. With this consideration in mind the concrete is relatively undamaged, having the stiffness of the material seemingly unaffected. This phenomenon is supported by research conducted by Yurtadas et al. (2004) which shows the unloading curve to be nearly parallel to the initial loading curve (Figure 2.9). The unrecovered strain is coming predominately from the inelastic shear sliding along preferred slip planes. Shear-enhanced compaction occurs in the presence of non-hydrostatic loading. Because shear stresses are a more effective means of voids closure than pure hydrostatic pressure, concrete will experience larger volumetric strains if one component of stress is greater than the others.

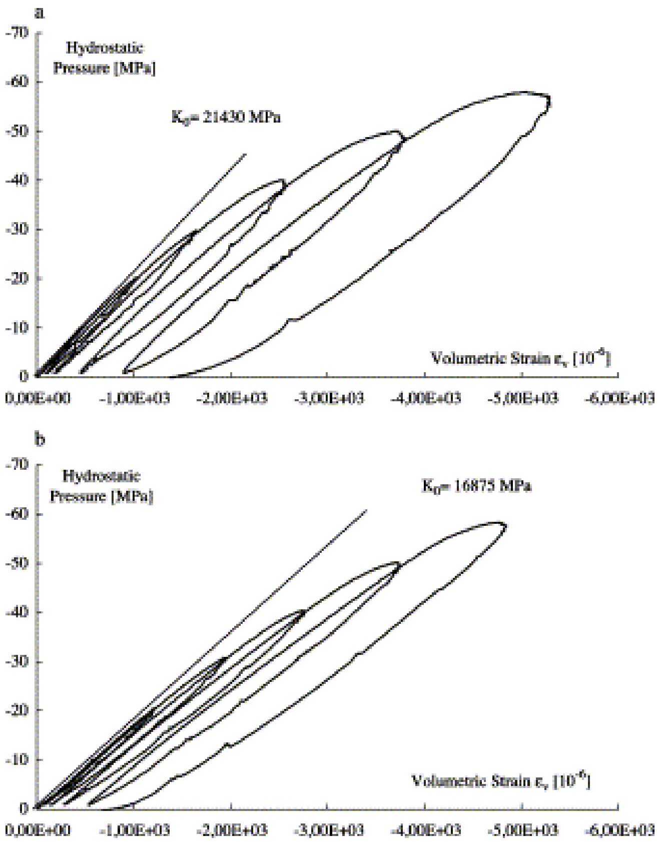

Fig. 2.9. Hydrostatic pressure vs. volumetric strain (Yurtdas et al., 2004)

2.8. Fatigue Loading

When there are repeated loading and unloading cycles on a structure, fatigue damage may be a controlling factor in the structures performance. Fatigue loading is prevalent in many concrete structures, though design engineers usually design a structure with sufficient strength so that the extent of fatigue damage is negligible. In practice this is a conservative approach and, although safe, can lead to uneconomical design of structures.

It is known that at certain load levels fatigue loading can have a detrimental effect on concrete's structural integrity. Song et al. (2005) performed an extensive test program to obtain several S-N curves for various fatigue loading conditions. Concrete specimens were subject to tension-compression cyclic loading in addition to varying levels of lateral loads. An S-N curve is a plot of the strength of a material vs. the number of cyclic loads for that given load case. Their results can be seen in Figure 2.10.

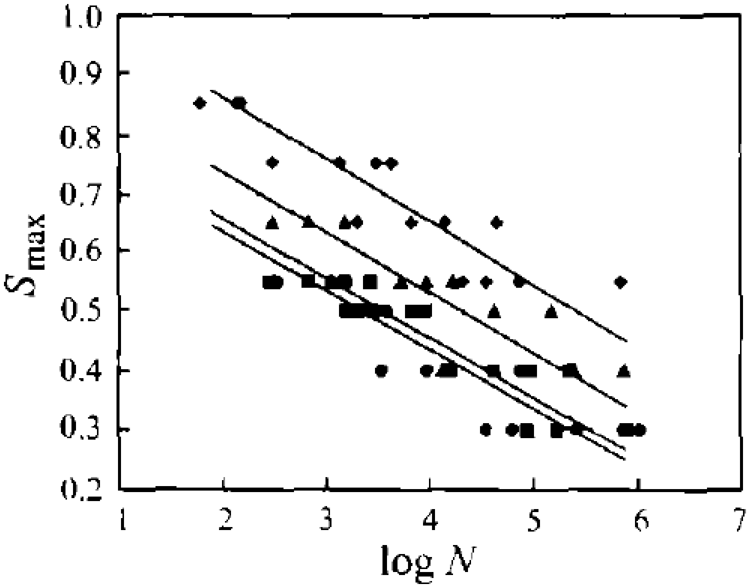

Fig. 2.10. S-N curve, $S_{max} = \sigma_{max}/f_t$, $0.1f_c$ lateral pressure, $0.2f_c$ lateral pressure, and $0.3f_c$ lateral pressure corresponds to square, triangle, and circle (Song et al., 2005)

The onset of damage within the concrete occurs at higher rates for larger load magnitudes. This can be seen in the strain vs. number of load cycles plot (Figure 2.11). In the figure one can see that the strain curve has three stages corresponding with the number of load cycles. The first stage occurs over approximately the first 10% of the concrete's life. In this stage the strain increases rapidly, as preexisting cracks in the transition zone propagate until they reach a stable phase. In the second stage, during the next 80% of the concrete's life, the crack development is slowed but continues at a stable rate. It is thought that the stronger mortar arrests the rapid propagation of the interface cracks. In the final stage cracks propagate unstably throughout the mortar and lead to failure. The final stage occurs during the final 10% of life (Song et al., 2005).

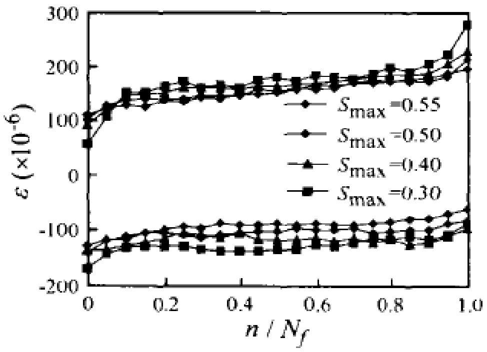

(a) Under the same lateral loading($R = 0.3$)

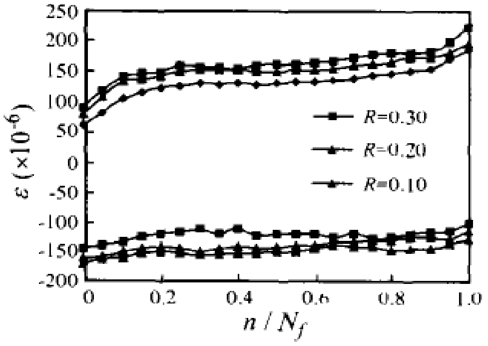

Fig. 2.11. Strain vs. number of cycles, R = lateral load ratio = σ_{lat}/f_c, $S_{max} = \sigma_{max}/f_t$ (Song et al., 2005)

In addition to the data presented by Song et al. (2005), Lee and Barr (2002) also compiled meaningful fatigue data for plain concrete from a variety of researchers. Table 1 shows the approximate amount of fatigue loading that occurs for a given structure including airport pavements, bridges, highway and mass transit structures, and sea structures.

Table 2.1. Approximate number of loading cycles for a given structure or loading condition

Low-cycle fatigue			High-cycle fatigue				Super-high-cycle fatigue		
1	10^1	10^2	10^3	10^4	10^5	10^6	10^7	10^8	10^9
Structures subjected to earthquakes			Airport pavements and bridges		Highway and railway bridges, highway pavements		Mass rapid transit structure		Sea structures

Source: Lee M. K. & Barr B. I. G. (2002). An overview of the fatigue behaviour of plain and fibre reinforced concrete. *Cement and Concrete Composites*, *26*, 299-305.

Figure 2.12 shows a compilation of experimental data for plain concrete subjected to uniaxial compressive fatigue loading presented by several researchers including Paskova and Meyer (1997),Grzybowski and Meyer (1993), Cachim (1999), and Do et al. (1993). The dimensionless term, $S = (\frac{\sigma_{app}}{f_c'})$, is thought to give the best possible description of fatigue behavior for various types of plain concrete because it eliminates the influence of important factors like water-cement ratio, type of aggregate, curing conditions, etc (Lee and Barr, 2004). It is important to notice that the relationship between the stress ratio, S, has a logarithmic relationship with the number of cyclic loads. It is logical then that at some load level the fatigue life of the material approaches infinity. In a practical sense infinity can be taken as a point at which the fatigue life far exceeds that of a realistic number of cyclic loads that may be experienced throughout the lifespan of a structure.

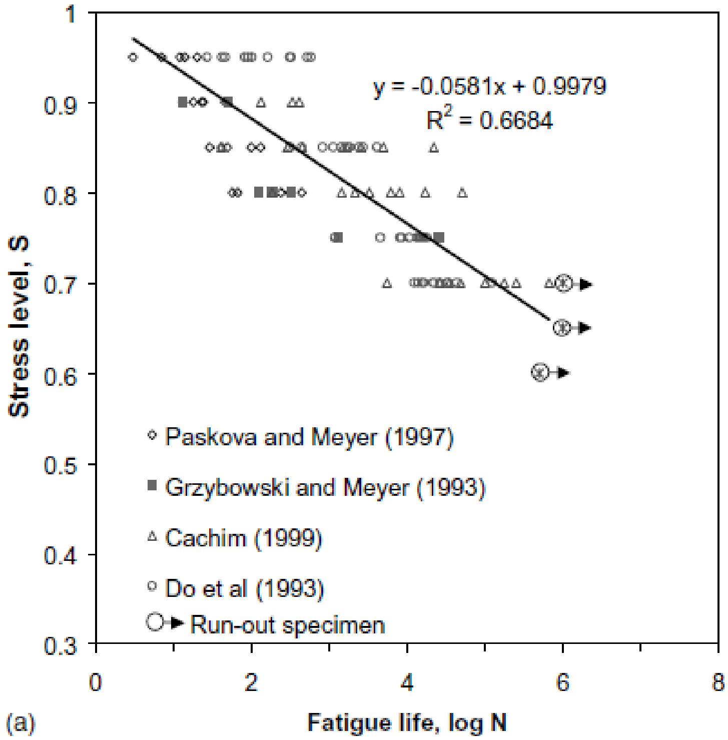

Fig. 2.12. Compilation of fatigue life data for uniaxial compressive loading of plain concrete (Lee and Barr, 2002)

Figure 2.13 shows a similar compilation of experimental data for flexural loading. It is important to provide data for various types of loading as concrete has different mechanical behavior in tension as opposed to compression. One should notice that the experimental data has a fairly large deviation. This may be caused by a variety of factors including testing methodology, specimen fabrication, or data errors. The goal of any fatigue life modeling of concrete should be to capture the essential features of the fatigue life behavior of concrete and not to duplicate the data.

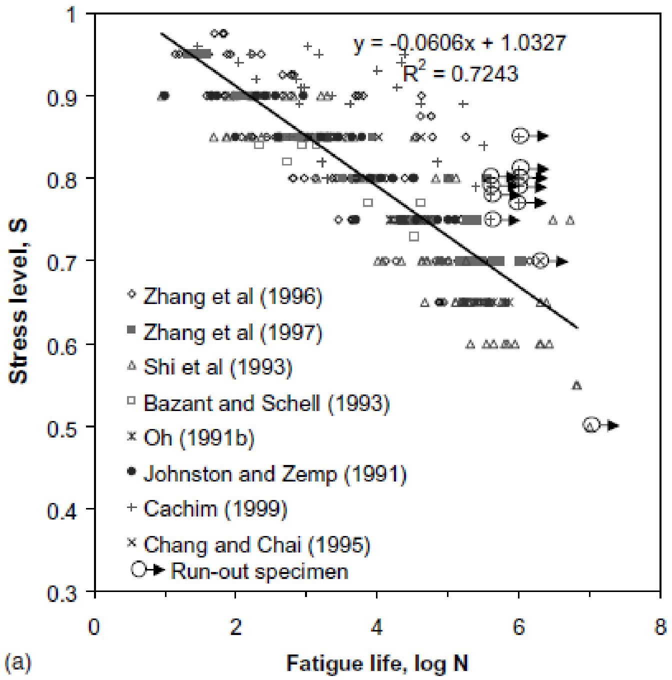

Fig. 2.13. Compilation of fatigue life data for flexural loading of plain concrete (Lee and Barr, 2002)

2.9. Freeze-Thaw Process

In recent years an increased focus is being given to the effect freeze-thaw cycles have on the stiffness and strength properties of concrete. Damage caused by frost expansion is a primary concern when designing concrete structures in cold weather regions. In essence, the freeze-thaw process can be thought of as a complex form of fatigue loading. The onset of damage within concrete can be accelerated when a freeze-thaw cycle occurs while a structure is subject to significant external loading (Miao et al., 2002). Shang et al. investigated the stiffness and strength performance of concrete after 25, 50, and 75 freeze-thaw cycles subjected to biaxial compression and axisymmetric triaxial compression.

Table 2.2. Effect of freeze-thaw on tensile performance of concrete

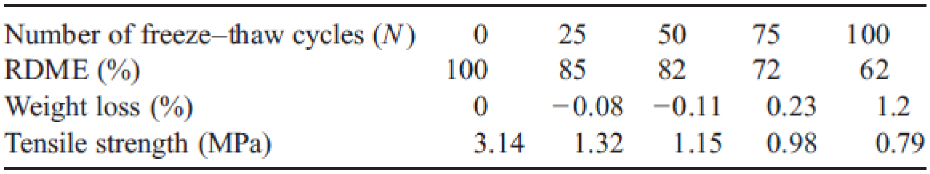

Number of freeze–thaw cycles (N)	0	25	50	75	100
RDME (%)	100	85	82	72	62
Weight loss (%)	0	−0.08	−0.11	0.23	1.2
Tensile strength (MPa)	3.14	1.32	1.15	0.98	0.79

Source: Shang H. S. & Song Y. P. (2006). Experimental study of strength and deformation of plain concrete under biaxial compression after freezing and thawing cycles. *Cement and Concrete Research*, 36, 1857-1864.

From the experimental data presented by Shang et al. (2006) for biaxial compression, it shows that the decrease in strength of the material decreases nearly linearly with increasing freeze-thaw cycles. This may hint at a nearly constant rate of microcrack propagation within the concrete matrix.

Table 2.3. Ultimate strength and strain of plain concrete subjected to biaxial compression for varying number of freeze-thaw cycles (Shang et al., 2006)

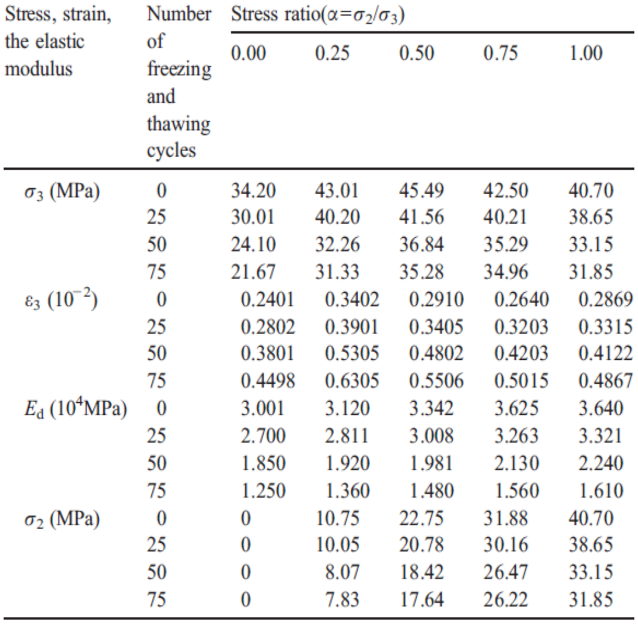

Stress, strain, the elastic modulus	Number of freezing and thawing cycles	Stress ratio($\alpha=\sigma_2/\sigma_3$)				
		0.00	0.25	0.50	0.75	1.00
σ_3 (MPa)	0	34.20	43.01	45.49	42.50	40.70
	25	30.01	40.20	41.56	40.21	38.65
	50	24.10	32.26	36.84	35.29	33.15
	75	21.67	31.33	35.28	34.96	31.85
ε_3 (10^{-2})	0	0.2401	0.3402	0.2910	0.2640	0.2869
	25	0.2802	0.3901	0.3405	0.3203	0.3315
	50	0.3801	0.5305	0.4802	0.4203	0.4122
	75	0.4498	0.6305	0.5506	0.5015	0.4867
E_d (10^4MPa)	0	3.001	3.120	3.342	3.625	3.640
	25	2.700	2.811	3.008	3.263	3.321
	50	1.850	1.920	1.981	2.130	2.240
	75	1.250	1.360	1.480	1.560	1.610
σ_2 (MPa)	0	0	10.75	22.75	31.88	40.70
	25	0	10.05	20.78	30.16	38.65
	50	0	8.07	18.42	26.47	33.15
	75	0	7.83	17.64	26.22	31.85

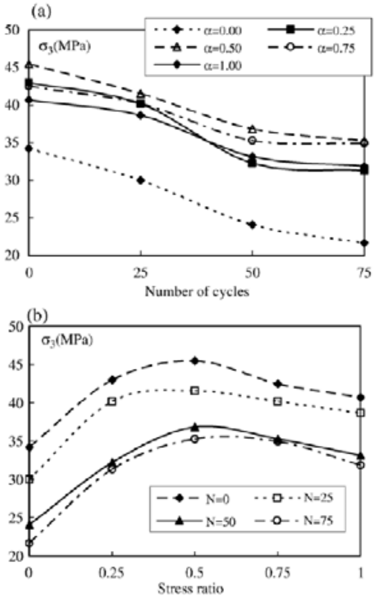

Source: Shang H. S. & Song Y. P. (2006). Experimental study of strength and deformation of plain concrete under biaxial compression after freezing and thawing cycles. *Cement and Concrete Research*, 36, 1857-1864.

Table 2.4. Ultimate strength and strain of plain concrete subjected to triaxial compression for varying number of freeze-thaw cycles (Shang et al., 2008)

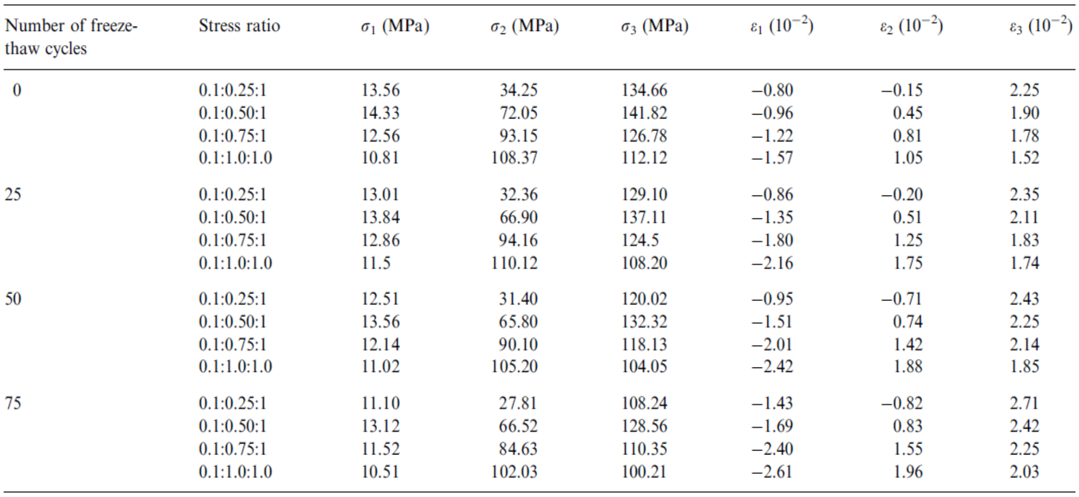

Number of freeze-thaw cycles	Stress ratio	σ_1 (MPa)	σ_2 (MPa)	σ_3 (MPa)	ε_1 (10^{-2})	ε_2 (10^{-2})	ε_3 (10^{-2})
0	0.1:0.25:1	13.56	34.25	134.66	−0.80	−0.15	2.25
	0.1:0.50:1	14.33	72.05	141.82	−0.96	0.45	1.90
	0.1:0.75:1	12.56	93.15	126.78	−1.22	0.81	1.78
	0.1:1.0:1.0	10.81	108.37	112.12	−1.57	1.05	1.52
25	0.1:0.25:1	13.01	32.36	129.10	−0.86	−0.20	2.35
	0.1:0.50:1	13.84	66.90	137.11	−1.35	0.51	2.11
	0.1:0.75:1	12.86	94.16	124.5	−1.80	1.25	1.83
	0.1:1.0:1.0	11.5	110.12	108.20	−2.16	1.75	1.74
50	0.1:0.25:1	12.51	31.40	120.02	−0.95	−0.71	2.43
	0.1:0.50:1	13.56	65.80	132.32	−1.51	0.74	2.25
	0.1:0.75:1	12.14	90.10	118.13	−2.01	1.42	2.14
	0.1:1.0:1.0	11.02	105.20	104.05	−2.42	1.88	1.85
75	0.1:0.25:1	11.10	27.81	108.24	−1.43	−0.82	2.71
	0.1:0.50:1	13.12	66.52	128.56	−1.69	0.83	2.42
	0.1:0.75:1	11.52	84.63	110.35	−2.40	1.55	2.25
	0.1:1.0:1.0	10.51	102.03	100.21	−2.61	1.96	2.03

Source: Shang H. S., Song Y. P., & Qin L. K. (2008). Experimental study on strength and deformation of plain concrete under triaxial compression after freeze-thaw cycles. *Building and Environment*, *43*, 1197-1204.

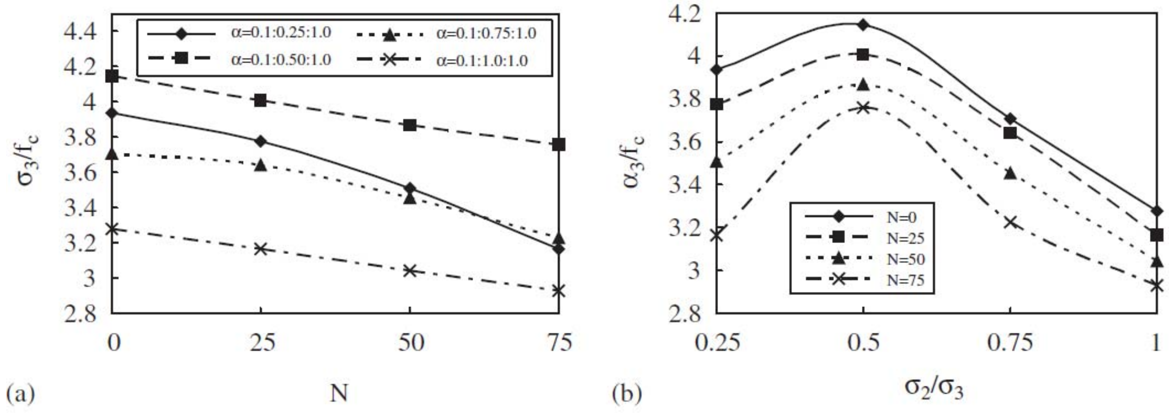

Fig. 2.14. (a) Normalized compressive strength, σ_3/f_c, vs. freeze-thaw cycles, (b) normalized compressive strength vs. lateral load ratio, σ_2/σ_3 (Shang et al., 2006)

For the experimental data shown by Shang et al. (2008) σ_3 is the primary loading direction, σ_2 adjusted throughout testing, and σ_1 is constant throughout the testing procedure. One notices that prior to the application any frost expansion damage the specimens behave as expected under variable biaxial loading. The maximum value for σ_3 occurs when $\sigma_2/\ \sigma_3$ is 0.5, corresponding to what was discussed previously about biaxial compression. With the onset of damage caused by the ensuing freeze-thaw cycles one can see a noticeable drop in the compressive strength in the primary loading direction. The greatest decrease in strength occurs when the lowest secondary load, σ_2, is applied. Shang et al. (2008) emphasize that confining loads reduce the damage caused by freeze-thaw stating that after 50 freeze-thaw cycles the uniaxial compressive strength is reduced to 70.5% of its original strength, while for the same number of cycles and with load ratio 0.1:0.5:1.0 the strength in the primary direction is reduced to 93.3% of the original strength. The reduced strength loss for higher confining loads can be explained at the microscopic level. Water infiltrates voids along the aggregate-mortar interface or within the cement matrix itself and as freezing sets in the volume of the entrapped moisture will expand. The increase in volume can do two things. If there is additional unfilled space available within the concrete voids the expanding moisture can spread without causing much damage or if no additional space is present the expanding moisture can apply internal stresses onto the tips of the encompassing voids. This can cause the voids or cracks to propagate, explaining the decreased load carrying capacity of concrete with increased freeze-thaw cycles. The reduced loss of strength with higher confining loads is the result of crack closer caused by the confining loads once the water thaws and its volume is once again reduced. Crack closure returns the overall volume of voids within the concrete to nearly what it originally was, allowing minimal addition water into the concrete.

Table 2.5. Percentage drop of ultimate strength of plain concrete subjected to triaxial compression loading with varying freeze-thaw cycles (Shang et al., 2008)

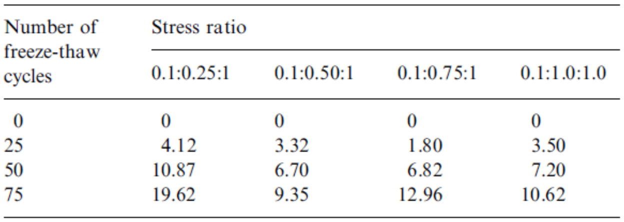

Number of freeze-thaw cycles	Stress ratio			
	0.1:0.25:1	0.1:0.50:1	0.1:0.75:1	0.1:1.0:1.0
0	0	0	0	0
25	4.12	3.32	1.80	3.50
50	10.87	6.70	6.82	7.20
75	19.62	9.35	12.96	10.62

Source: Shang H. S., Song Y. P., & Qin L. K. (2008). Experimental study on strength and deformation of plain concrete under triaxial compression after freeze-thaw cycles. *Building and Environment*, *43*, 1197-1204.

Similar conclusions can be taken from the deformation characteristics of the concrete, shown in Figures 2.15 and 2.16. The onset of damage caused by the freeze-thaw cycles causes an increase in strain under all loading conditions. The overall compressive strain at failure is larger for specimens subjected to freeze-thaw damage. With increased freeze-thaw damage, the plastic-hardening phase of the stress-strain curve occurs at much lower stress levels, which can be seen in Figure 2.16. The strains in the lateral directions also show an increase in magnitude with more freeze-thaw cycles. This illustrates the fact that, with no prior external loading and preexisting damage being of an isotropic nature, the freeze-process induces damage in all directions. This may not be the case if concrete is loaded, causing anisotropic damage, followed by freeze-thaw damage. Under this condition, the freeze-thaw damage may occur primarily in the direction damage is already occurring, as the moisture expansion will cause existing cracks to propagate.

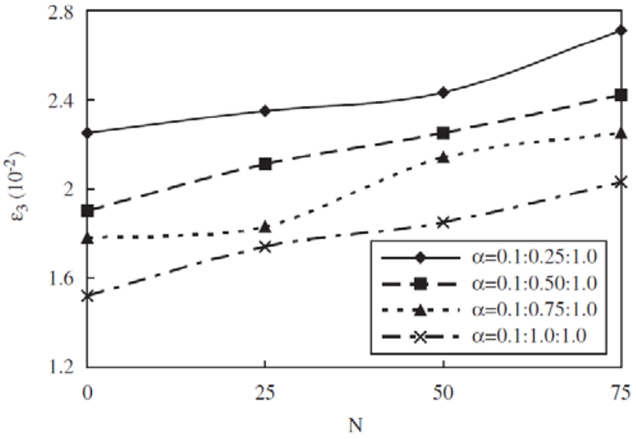

Fig. 2.15. Strain in the primary loading direction vs. number of freeze-thaw cycles (Shang et al., 2008)

Figure 2.17 includes uniaxial compressive strength data for freeze-thaw damage presented by Shang et al. (2009). The uniaxial compressive strength of air-entrained concrete was measured after 0, 50, 100, 150, 200, 300, 350, and 400 freeze-thaw cycles. After 400 cycles the compressive strength was found to decrease by 53%. The tabulated results are also shown.

Table 2.6. Uniaxial compressibe strength of air-entrained concrete for various number of freeze-thaw cycles

Numbers of freeze-thaw cycles	0	50	100	150	200	300	350	400
Cubic compressive strength	34.2	33.4	31.67	27.60	26.38	21.10	19.13	16.22
Compressive strength	26.3	25.9	25.9	24.8	23.33	22.63	17.50	14.25

Source: Shang H. S., Song Y. P., & Qin L. K. (2008). Behavior of Air-Entrained Concrete After Freeze-Thaw Cycles. *Acta Mechanica Solida Sinica*, *22(3)*, 261-266.

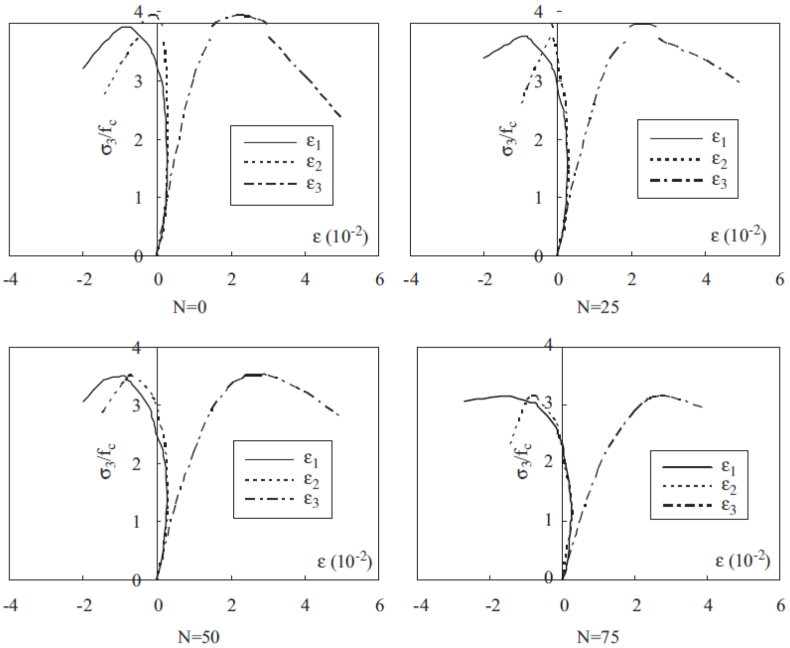

Fig. 2.16. Strain vs. principle stress ratio for various number of freeze-thaw cycles (Shang et al., 2002)

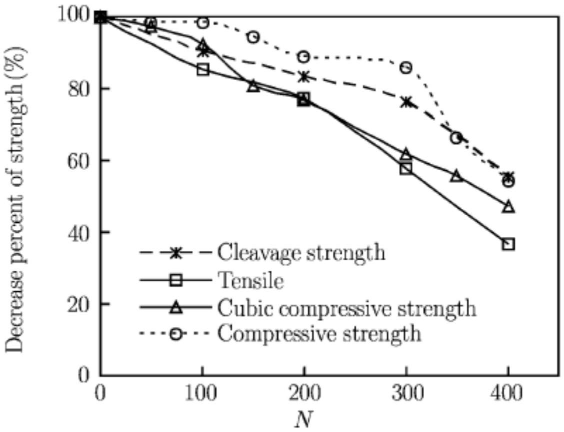

Fig. 2.17. Strength vs. number of freeze-thaw cycles for uniaxial tension and compressive loading of air-entrained concrete (Shang et al., 2009)

Research performed by Detwiler et al. (1989) explains that there are two forms of freeze-thaw damage. The first is termed hydraulic pressure and is much more prevalent during rapid freezing processes. It is well known that water that has been absorbed into the capillary pores of the cement matrix expands once frozen. If the required volume that is needed for the expansion is not available, the excess frozen water is transported away by internal pressure. The magnitude of pressure created, as well as the resulting damage, is related to the permeability of the cement matrix, the rate of freezing, the degree of saturation, and the location of the nearest unfilled void within the cement matrix. Local cracking will occur if the resultant pressure exceeds the tensile strength of the concrete. Progressive damage occurs within the concrete because as cracking occurs, more volume is available for water to infiltrate and freeze, causing the existing cracks to propagate (Detwiler et al., 1989).

The second form of freeze-thaw damage is termed ice accretion and is more prevalent during long freeze periods and when the rate of freezing is relatively slow. Water in gel pores requires a much lower temperature to freeze, -78^{o} C according to Cordon (1966). This is due to the surface tension forces present in these regions of extremely small radii. For most realistic applications water in the gel pore zones will remain in a liquid state while it remains in the gel pore. As temperature drops below 0^{o} C the water in the gel pores becomes supercooled and has a higher free energy than the ice in the capillaries which allows the water to move from the gel pores into the capillaries where it is more likely to freeze (Detwiler et al., 1989). The overall effect of this process is a reduced volume of the concrete in the form of gel water and an increase in the volume of the capillaries due to expansion of frozen water. Upon thawing, some of the water may return to the gel pores, but the original state of the material will not be obtained as this process is not reversible.

Detwiler et al. (1989) also discuss several ASTM methods for assessing the durability of concrete subjected to freeze-thaw effects. ASTM C 666 "Resistance of Concrete to Rapid Freezing and Thawing" is the most common for assessing the durability of concrete. It consists of 2 to 5 hour freeze-thaw cycles in which damage is assessed periodically throughout testing by visual observation and testing of the dynamic modulus of elasticity. ASTM C 671 “Critical dilation of Concrete Specimens Subjected to Freezing,” is another test in which cylindrical specimens are cooled and warmed at a controlled rate while the length change of the specimen is tabulated for each cycle. A similar test can be performed on a variety of mix designs to see how various aggregate types perform on various environmental conditions.

The critical saturation test is the measurement of the volume of evaporable water in pores as a ratio of the total void space at which freeze-thaw cycles will damage the concrete. The amount of time it takes a given type of concrete to reach critical saturation of determined by a series of absorption tests. The frost resistance is considered to be difference between the existing degree of saturation and the critical degree of saturation at a given time.

Detwiler et al. (1989) concluded that the usefulness of these tests are questionable if one is trying to determine the performance of a given concrete mix for actual service applications. The tests give engineers the ability to qualitatively compare various concrete types for their durability with respect to freeze-thaw effects. The tests do not, however, give engineers the ability to predict the service life of that concrete quantitatively.

From the experimental data presented by Shang et al. (2008) and the discussion presented by Detwiler et al. (1989) it is clear that a meaningful constitutive model needs to be developed to help predict the behavior and performance of concrete under these unique conditions. The design life of the concrete needs to be taken into consideration so a more efficient, yet safe, design can be obtained.

CHAPTER 3. REVIEW OF RELEVANT LITERATURE

3.1. Continuum Damage Mechanics

When discussing the use of continuum damage mechanics for concrete modeling it first becomes necessary to define the term "damage" as it applies to concrete. There are three types of damage that can be distinguished within concrete, each having optimum theories used to model its corresponding type of damage (Krajcinovic, 1989):

1. Atomic voids and defects in the crystal structure. This form of damage can be modeled using material science models at the atomic scale.
2. Microcracks and microvoids, these can be modeled using continuum damage mechanics. The crack, or damage, density can be quantified using damage theory.
3. Cracks on a macro scale. This form of damage can be modeled using fracture mechanics, which can predict the propagation of a discrete crack within concrete.

As stated earlier, because damage in the form of microcracks and microvoids governs the majority of concretes nonlinear behavior, continuum damage mechanics is considered an appropriate foundation for the formulation of a working concrete model. Continuum damage mechanics uses a number of internal variables to define the local distribution of microcracks or microvoids in terms of an averaged density. Because damage occurring within concrete is highly anisotropic, a simple scalar variable representing damage accumulation will not suffice. The use of a fourth order tensor to represent damage is necessary to illustrate the true directionally dependent behavior of damage accumulation within brittle materials. The Yazdani and Schreyer model (1988) uses a fourth order compliance tensor to illustrate the accumulation of damage within concrete and is explained in Section 3.2.

Damage mechanics is supported by various thermodynamic theories based on the theory of irreversible processes. The primary irreversible process within concrete, which is termed damage, is microcracking. In Chapter 4 these thermodynamic theories are presented in detail and a dissipation inequality is introduced which is supported by the Clausius-Duhem inequality. These inequalities place certain restrictions upon the set of internal variables that are used to define the state of the material.

Previously, damage accumulation resulting from monotonic loading was discussed. Fatigue loading can simply be thought of as additional accumulation of damage at a given load level for repeated cycles. In order to capture the softening phenomenon that occurs with the onset of fatigue damage a novel solution will be used that was presented by Wen (2011) for use in modeling both carbon fiber reinforced composites and steel fiber reinforced concrete. In his model a simple softening function is used to reduce the solid's ultimate strength as the number of fatigue cycles increases. The function follows classical S-N curve behavior and correlates well with experimental data.

3.2. Yazdani Damage Mechanics Model (1993)

Several simple, yet powerful changes were made to the previously discussed Yazdani and Schreyer model (1988) in Yazdani's newer model (1993). The main deficiency of the previous model was that it exhibited a "snap back" in the deformation of concrete in the softening regime of the stress-strain curve. The closed form solution for uniaxial compressive strain of concrete is given below for the previous model (Yazdani and Schreyer, 1988) and a figure follows.

$$\varepsilon_1 = -\left(\frac{1}{E_0} + ck\right)\boldsymbol{\sigma}_{\mathbf{1}}^{-} \tag{3.1}$$

where c is a constant and k is a scalar value related to the damage density

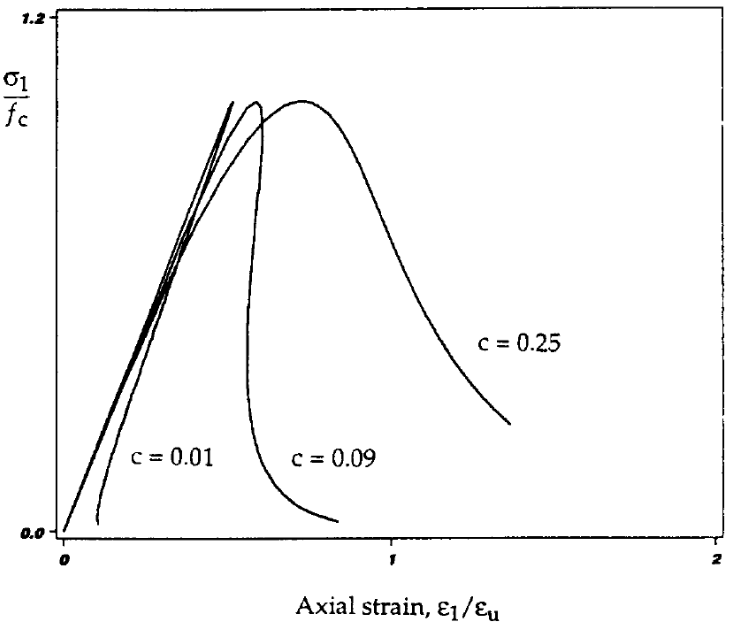

Fig. 3.1. Apparent “snap back” behavior present in Yazdani and Schreyer model (1988)

This behavior is not intended and is remedied in Yazdani’s revision (1993) using new forms of the response tensors and the damage function. Using similar notations as in Yazdani and Schreyer (1988) the following is given for the response tensor corresponding to tension loading regime:

$$\boldsymbol{R_I} = \frac{\boldsymbol{\sigma}^+ \otimes \boldsymbol{\sigma}^+}{\boldsymbol{\sigma}^+ : \boldsymbol{\sigma}^+} + \gamma H(\lambda_1)(\boldsymbol{I} - \boldsymbol{i} \otimes \boldsymbol{i}) \tag{3.2}$$

where $H(\lambda_1)$ is a heavyside function with λ_1 being the maximum eigenvalue of the positive cone of stress. A rate form of inelastic strain is also defined in this model (inelastic strain for tension loading was assumed to be negligible in the previous model).

$$\dot{\boldsymbol{\varepsilon}}^i = \dot{k}\boldsymbol{M} = \dot{k}(\boldsymbol{M}_I + \boldsymbol{M}_{II}) \tag{3.3}$$

where the decomposed forms of a response tensor $\boldsymbol{M}$, I and II, are for tension loading and compression loading, respectively.

$$\boldsymbol{M_I} = \beta_1 \boldsymbol{\sigma}^+ \tag{3.4}$$

β_1 is a material parameter used to account for the inelastic strains resulting from imperfect crack closure and misfit surfaces. For damage occurring under compression loading the following response tensor is utilized:

$$\boldsymbol{R}_{II}^{d} = \frac{\widetilde{\boldsymbol{\sigma}} \otimes \widetilde{\boldsymbol{\sigma}}}{\widetilde{\boldsymbol{\sigma}} : \widetilde{\boldsymbol{\sigma}}} \qquad where\ \widetilde{\boldsymbol{\sigma}} = \boldsymbol{\sigma}^- - \lambda \boldsymbol{i} \tag{3.5}$$

$$\boldsymbol{R_{II}^{h}} = \alpha H(-\bar{\lambda})(\mu \boldsymbol{I} - \boldsymbol{i} \otimes \boldsymbol{i}) \tag{3.6}$$

λ and $\bar{\lambda}$ are considered to be the maximum eigenvalue and minimum eigenvalue of the negative cone of stress, respectively. The response tensor representing inelastic strains for compression loading is the same as in the previous model and is given as the following:

$$\boldsymbol{M_{II}} = \boldsymbol{S}^- + \beta_2 \boldsymbol{S}^+ \tag{3.7}$$

The addition of a transition function to the damage function in this model allows for the varying strength properties of concrete to be utilized within the model. Previously a “cross effect coefficient” c was used in the response tensor to differentiate between the relative strength of concrete in tension and compression. This was the main cause of the “snap back” behavior that is present in the Yazdani Schreyer model. In this model a transition function which reflects the appropriate strength parameter of concrete corresponding to appropriate load case is used.

$$t(\boldsymbol{\sigma}, k) = A(\boldsymbol{\sigma}) e \frac{\ln{(1 + E_0 k)}}{1 + E_0 k} \tag{3.8}$$

This logarithmic form is the same as that used in the Yazdani and Schreyer (1988) model with the exception of the transition function, $A(\boldsymbol{\sigma})$. $A(\boldsymbol{\sigma})$ is the maximum value of the function

$t(\boldsymbol{\sigma}, k)$ and changes depending on the load path. The range of the transition function, $A(\boldsymbol{\sigma})$, can be determined from the biaxial damage surface. As in the Yazdani and Schreyer model:

$$\psi(\boldsymbol{\sigma}, k) = \frac{1}{2}\boldsymbol{\sigma}:\boldsymbol{R}:\boldsymbol{\sigma} + \boldsymbol{M}:\boldsymbol{\sigma} - \frac{1}{2}t^2(k) = 0 \tag{3.9}$$

Inserting the appropriate forms of the response tensors the following is obtained:

$$\begin{aligned}\psi(\boldsymbol{\sigma}, k) = \tfrac{1}{2}(1+\beta_1)\boldsymbol{\sigma}^+:\boldsymbol{\sigma}^+ + \tfrac{1}{2}\boldsymbol{\sigma}^-:\tfrac{\tilde{\boldsymbol{\sigma}}\otimes\tilde{\boldsymbol{\sigma}}}{\tilde{\boldsymbol{\sigma}}:\tilde{\boldsymbol{\sigma}}}:\boldsymbol{\sigma}^- + \tfrac{1}{2}\left(\gamma H(\lambda_1) + \alpha H\left(-\bar{\lambda}\right)\right)\boldsymbol{\sigma}:\boldsymbol{\sigma} - \\ \tfrac{1}{2}\left(\gamma H(\lambda_1) + \alpha H\left(-\bar{\lambda}\right)\right) tr^2(\boldsymbol{\sigma}) + (\boldsymbol{S}^- + \beta_2\boldsymbol{S}^+):\boldsymbol{\sigma} - \tfrac{1}{2}t^2(k) = 0\end{aligned} \tag{3.10}$$

At the limit state if $t(\boldsymbol{\sigma}, k)$ is solved for in uniaxial tension, $A^2(\boldsymbol{\sigma}) = (1+\beta_1)f_t^2 = F_t$; if $t(\boldsymbol{\sigma}, k)$ is solved for in uniaxial compression, $A^2(\boldsymbol{\sigma}) = (\frac{7}{3})f_c^2 = F_c$. Now that the range of the transition function has been determined, the form of the function is given as

$$A^2(\boldsymbol{\sigma}) = \frac{(1+\zeta^2+2\alpha\zeta)F_t^2}{1+\zeta^2\left(\frac{F_t}{F_c}\right)^2 + 2\alpha\zeta\left(\frac{F_t}{F_c}\right)^2} \quad where \;\; \zeta = \left\|\frac{tr\boldsymbol{\sigma}^-}{tr\boldsymbol{\sigma}^+}\right\| \tag{3.11}$$

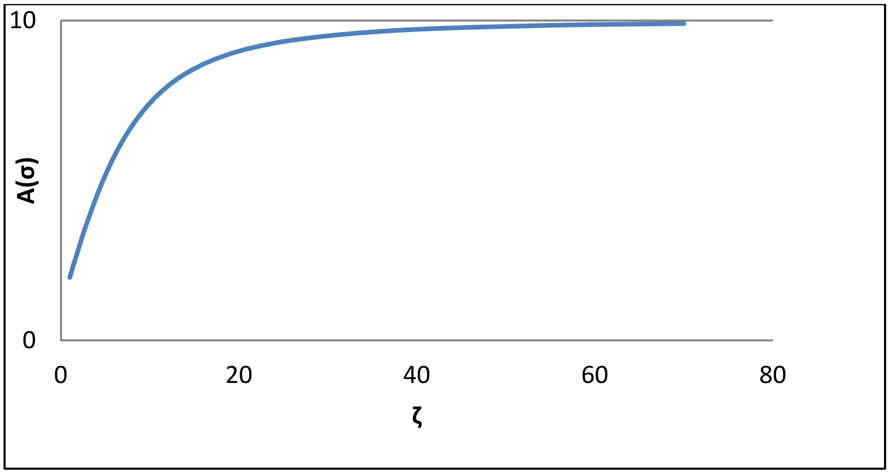

Fig. 3.2. Behavior of transition function, A, with respect to $\boldsymbol{\zeta}$

The behavior of the transition function, $A(\boldsymbol{\sigma})$, is such that when $\zeta = 0$ (tension loading), $A(\boldsymbol{\sigma}) = F_t$; when $\zeta \to \infty$ (compression loading), $A(\boldsymbol{\sigma}) = F_c$. Figure 3.2 shows the behavior of the transition function. It shows a smooth transition from the strength characteristics present under tension loading and compression loading.

Using the equation for the damage surface and for strain, the following model outputs are compared with experimental results.

Parameters
$\alpha = 0.985$
$\gamma = 0.2$
$\beta 1 = 1.2$
$\beta 2 = 1.2$
$\nu = 0.2$ (Poisson's Ratio)
$E_0 = 40{,}000$ Mpa
$f'_c = 32$ Mpa
$f_t = 3.2$ Mpa
$\varepsilon_{cu} = 0.003$
$\varepsilon_{tu} = 0.0003$

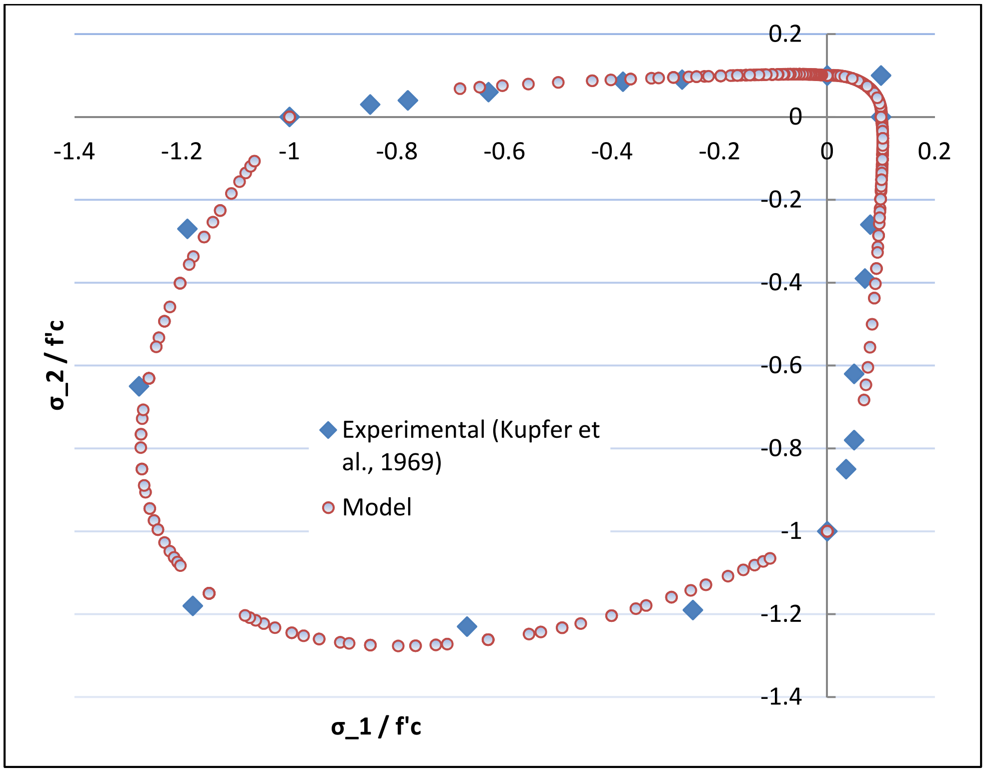

Fig. 3.3. Biaxial strength surface

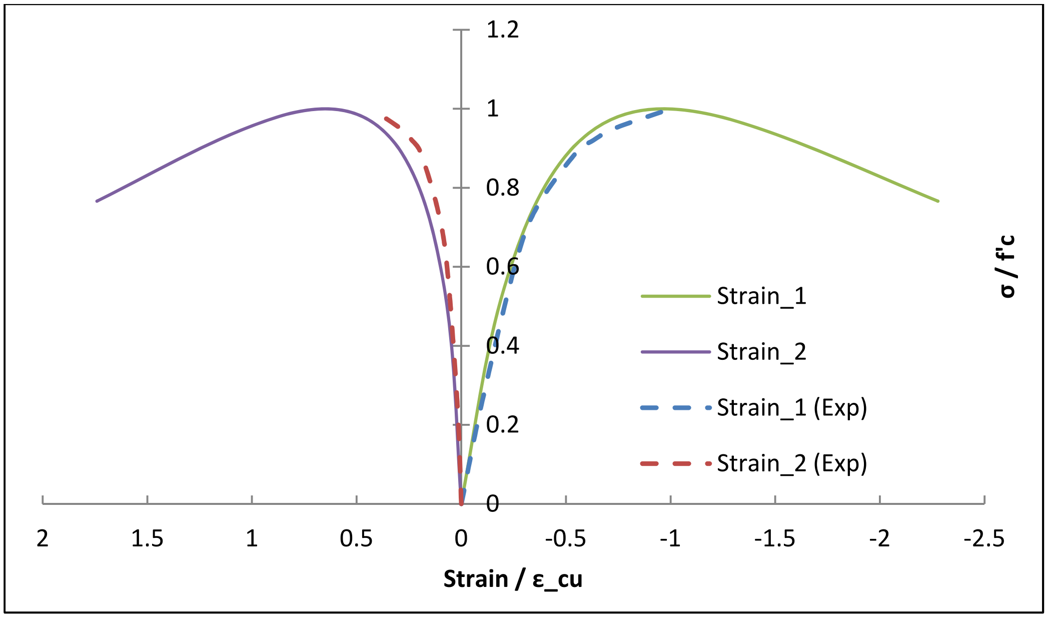

Fig. 3.4. Stress vs. strain behavior for concrete in uniaxial compression (experimental data: Litewka and Debinski, 2003)

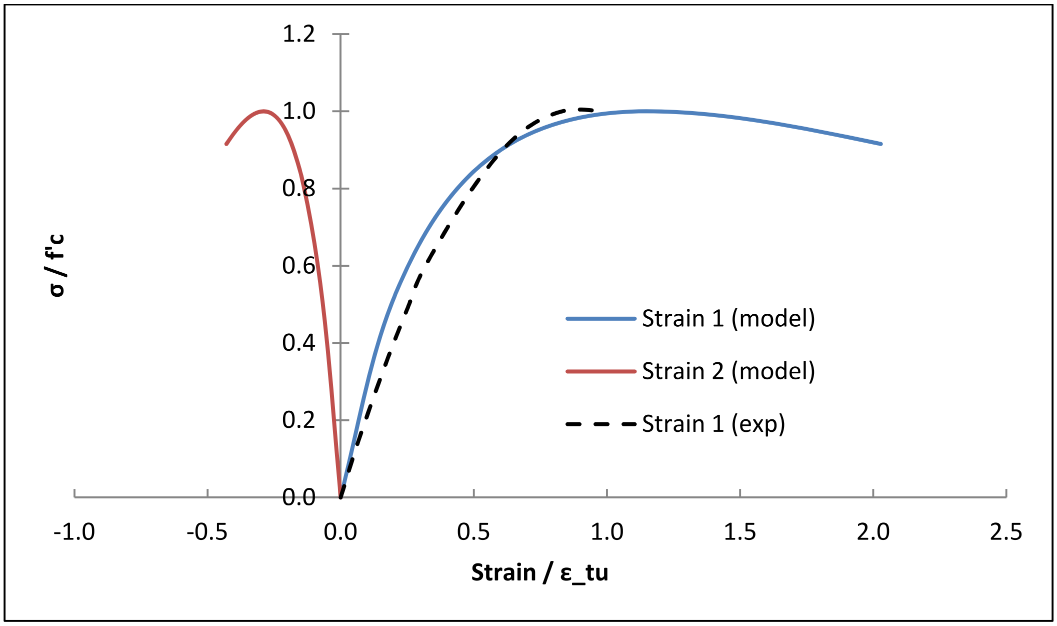

Fig. 3.5. Stress vs. strain for concrete in uniaxial tension (experimental data: Litewka and Debinski, 2003)

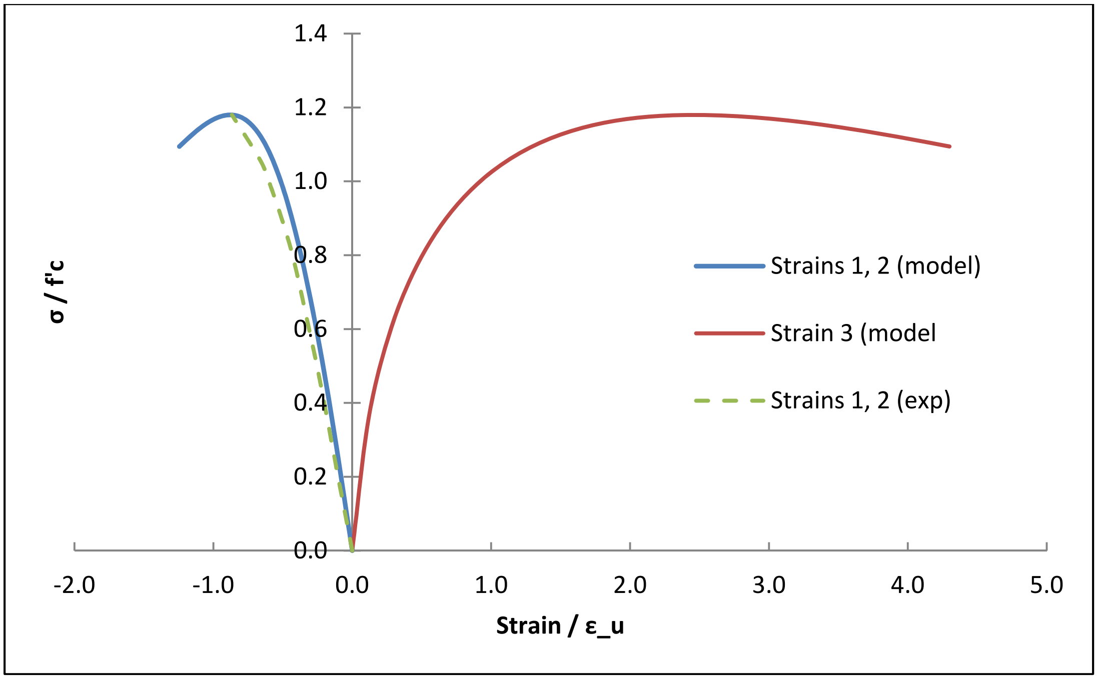

Fig. 3.6. Stress vs. strain for concrete in equal-biaxial compression (experimental data: Lee et al., 2004)

This model shows good correlation with the experimental behavior of concrete for monotonic loading. However, theIn Chapter 5 it will be extended to include fatigue and freeze-thaw behavior of concrete.

3.3. Wen Damage Mechanics Model (2011)

As stated previously, Wen's model (2011) is similar to the Yazdani and Schreyer model (1988), but he incorporates a softening function that is able to account for fatigue damage and its effects on the mechanical properties of the material being modeled. In this section Wen's model for the fatigue behavior of woven fiber composites will be discussed. Though his model is not formulated specifically for structural concrete, it will be shown in later chapters that his use of a softening function can be similarly used in damage modeling of concrete. It will be seen that Wen's model (2011) differs from the Yazdani and Schreyer model (1988) in several ways including the form of the response tensors describing total strain (elastic, damage, and inelastic strains), the damage function used to describe the onset of damage or the limit surface, and the incorporation of the softening function for fatigue loading applications.

The form of Gibbs Free Energy is the same as that in the previous model and is shown as the following:

$$G(\boldsymbol{\sigma}, k) = \frac{1}{2}\boldsymbol{\sigma}:\boldsymbol{C}(k):\boldsymbol{\sigma} + \boldsymbol{\sigma}:\boldsymbol{\varepsilon}^i(k) - A^i(k) \tag{3.12}$$

Wen (2011) uses a form of compliance tensor used by Ortiz as the following:

$$\boldsymbol{C}(k) = \boldsymbol{C}^{\boldsymbol{0}} + \boldsymbol{C}^c(k) \qquad (Ortiz, 1985) \tag{3.13}$$

In this equation $\boldsymbol{C}^{\boldsymbol{0}}$ is the initial compliance and $\boldsymbol{C}^c(k)$ results from the occurrence of damage in the material. Differentiating GFE with respect to stress we can obtain the total strain of the system.

$$\boldsymbol{\varepsilon} = \boldsymbol{C}^{\boldsymbol{0}}:\boldsymbol{\sigma} + \boldsymbol{C}^c(k):\boldsymbol{\sigma} + \boldsymbol{\varepsilon}^{\boldsymbol{i}}(k) \tag{3.14}$$

In Equation 3.21 above, the first term is the elastic strain, the second term is recoverable strain caused by elastic damage (microcracking), and the third term is the inelastic strain which is similar to the Yazdani and Schreyer model (1988). A form of the additional flexibility $\boldsymbol{C}^c(k)$ is used. He introduces the added flexibility at two parts, one for each microcrack mode caused by either compression or tension. Compression microcracking occurs parallel to the loading direction, while tension microcracking occurs perpendicular to the loading direction.

$$\boldsymbol{C}^c = \boldsymbol{C}_{\boldsymbol{I}}^{\boldsymbol{c}} + \boldsymbol{C}_{\boldsymbol{II}}^{\boldsymbol{c}} \tag{3.15}$$

Wen (2011) also introduces response tensors, which predict the direction of damage, that form the rate independent damage:

$$\dot{\boldsymbol{C}}_{\boldsymbol{I}}^{\boldsymbol{c}} = \dot{k}\boldsymbol{R}_I \qquad \dot{\boldsymbol{C}}_{\boldsymbol{II}}^{\boldsymbol{c}} = \dot{k}\boldsymbol{R}_{\boldsymbol{II}} \tag{3.16}$$

For irreversible damage, $\dot{k} \geq 0$.

Further, a rate form of inelastic strain is proposed by Yazdani and Karnawat (1996):

$$\dot{\boldsymbol{\varepsilon}}^i = \dot{k}\boldsymbol{M} \qquad (3.17)$$

Where M is another response tensor used to describe the inelastic strain. Also, the following equation is proposed to represent the scalar function A^i and is termed the softening law.

$$t(k)^2 = 2\frac{\partial A^i}{\partial k} \qquad (3.18)$$

Using the equations above and the GFE equation, Wen (2011) gives the following damage function.

$$\varphi(\boldsymbol{\sigma}, k) = \frac{1}{2}\boldsymbol{\sigma}^+ : \boldsymbol{R_I} : \boldsymbol{\sigma}^+ + \frac{1}{2}\boldsymbol{\sigma}^- : \boldsymbol{R_{II}} : \boldsymbol{\sigma}^- + \boldsymbol{\sigma} : \boldsymbol{M} - \frac{1}{2}t(k)^2 \geq 0 \qquad (3.19)$$

$\boldsymbol{\sigma}^+$ and $\boldsymbol{\sigma}^-$ are the positive (tension) and negative (compression) parts of the stress tensor. This equation basically states that if this equation is true, damage is occurring, and if not, the material is in its elastic range. The damage function above is considered a damage surface by which an elastic domain is contained. Two conditions must be met for damage to occur. First, the point of stress must fall on this surface and second, the stress increment must point outside the damage surface, away from the elastic domain.

$$\varphi(\boldsymbol{\sigma}, k) = 0 \qquad \frac{\partial \varphi}{\partial \boldsymbol{\sigma}} : \dot{\boldsymbol{\sigma}} > 0 \qquad (3.20)$$

Wen only considers uniaxial and biaxial tension loading in his research. For this, $\boldsymbol{R}_{II}$ is left out of the function. To obtain the form of the response tensor, Wen uses classical kinetic theory. He proposes the following form:

$$\boldsymbol{R}_I = \frac{\boldsymbol{\sigma}^+ \otimes \boldsymbol{\sigma}^+}{\boldsymbol{\sigma}^+ : \boldsymbol{\sigma}^+} - \alpha(\boldsymbol{I} - \boldsymbol{i} \otimes \boldsymbol{i}) \qquad (3.21)$$

$\boldsymbol{I}$ and **i** are fourth and second order identity tensors, respectively. α is a material parameter. The second term of the response tensor is used to illustrate the change that occurs in the Poisson's

Ratio once damage accumulates. The response tensor above is able to predict the crack behavior shown on the left side of the figure below. The crack formation under compression loading can be illustrated by $\boldsymbol{R_{II}}$ which has been left out of this formulation.

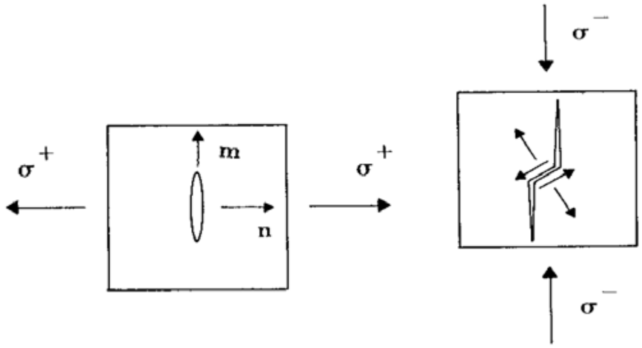

Fig. 3.7. Crack modes illustrated by response tensors I (left) and II (right)

The response tensor **M** for the rate of inelastic strain is given below.

$$\boldsymbol{M} = \beta\boldsymbol{\sigma} \tag{3.22}$$

β is also a material parameter that can be determined experimentally.

3.3.1. Fatigue Modeling (Wen, 2011)

The fatigue life model proposed by Wen (2011) specifies failure criteria for woven fabric composites. His model is capable of accurately predicting the fatigue life for multi-axial loading along the principle fiber directions. It is important to note that it has not yet been checked with off-axis loading or shear. This study is primarily limited to uniaxial and biaxial tensile loading of the composite.

As stated earlier, one of the advantages of these types of composites is that their strength properties are able to be tailored to their specific application. For this reason, it is important that Wen's model is capable of incorporating these differing strengths in different directions into the fatigue model. Wen uses a simple direction function to accomplish this and will be explained in the upcoming formulation.

Bounding surface theories in damage mechanics claim that a loading point in stress space is enclosed by a bounding surface that represents the surface at which damage will occur, or in this case, fatigue failure will occur. For this particular model, the bounding surface will evolve in correspondence with the state variables representing loading and material conditions as well as the model's material properties.

With this idea in mind, Wen (2011) represents his model in the 2-Dimensional loading (biaxial loading) environment. The envelope produced by his model creates a limit surface, or ultimate surface, which represents a series of biaxial load combinations at which failure will occur under static loading. A representation of his boundary surface can be seen below in the figure. Note that for n = 1 (first cycle) the failure envelope is the same as it would be for monotonic loading, while at n = N (fatigue life) the failure envelope is reduced.

From the earlier formulation of the dissipation inequality, and with the introduction of a softening function to illustrate the reduction in strength with fatigue loading, this bounding surface can be formed. The following sections develop a bounding surface and show its simplicity in 2-dimensional application. Comparisons with experimental data performed by Smith and Pascoe (1989) are made.

The formulation of the fatigue life model is done under the assumption of any deformation in the material being small and thermal effects having a negligible effect on the system. These are reasonable assumptions for low frequency loading. In addition, the bounding surface is found for tension loading only. From the earlier formulation, Wen (2011) starts with Gibbs Free Energy (GFE) to obtain a dissipation inequality.

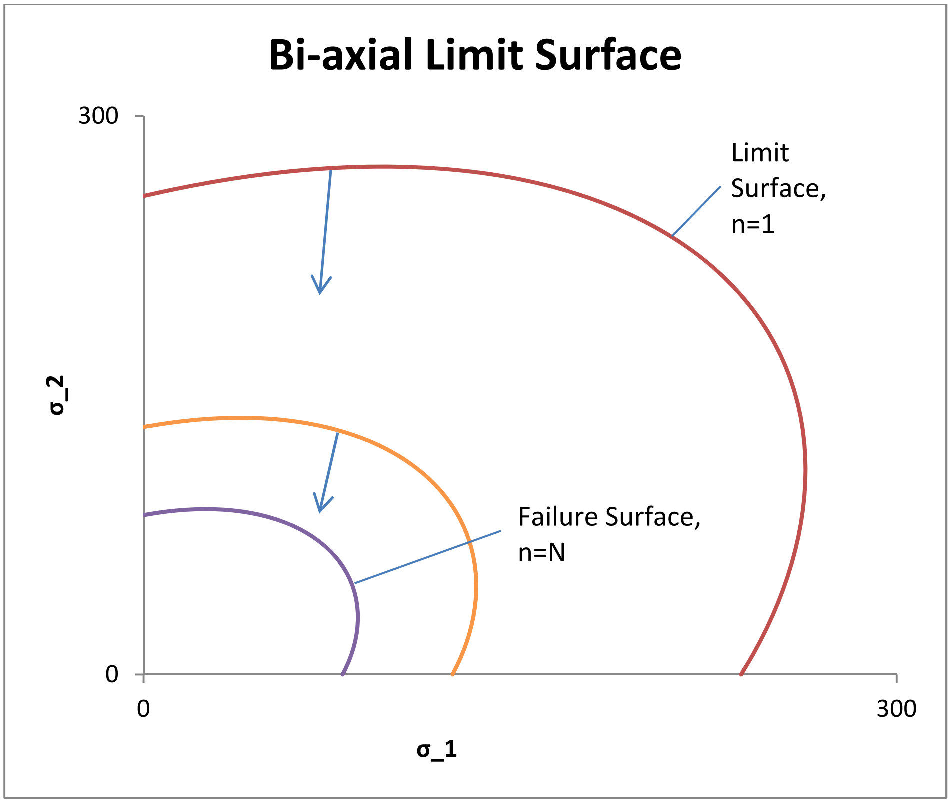

Fig. 3.8. Boundary surface representation, N = fatigue life (cycles)

$$G = \frac{1}{2}\boldsymbol{\sigma}:\boldsymbol{C}:\boldsymbol{\sigma} + \boldsymbol{\sigma}:\boldsymbol{\varepsilon^{i}} - A^{i}(k) \tag{3.23}$$

In this equation, **C** is the compliance tensor, $\boldsymbol{\varepsilon^{i}}$ is the inelastic strain tensor, $\boldsymbol{\sigma}$ is the stress tensor, $A^{i}(k)$ is a scalar damage function, and k is the fatigue damage accumulated in the system. The ":" symbol is a tensor contraction operator.

As stated previously, the dissipation inequality can be given in terms of differentiating GFE in terms of k.

$$\frac{\partial G}{\partial k}\dot{k} \geq 0 \tag{3.24}$$

The dissipation inequality becomes:

$$\frac{1}{2}\boldsymbol{\sigma}:\frac{\partial \boldsymbol{C}}{\partial k}:\boldsymbol{\sigma} + \boldsymbol{\sigma}:\frac{\partial \boldsymbol{\varepsilon^{i}}}{\partial k} - \frac{\partial A^{i}}{\partial k} \geq 0 \tag{3.25}$$

If we introduce the compliance tensor as an initial undamaged fourth order tensor and an additional flexibility tensor that is influenced by the damage we can develop the dissipation inequality further.

$$\boldsymbol{C}(k) = \boldsymbol{C}^{\boldsymbol{0}} + \boldsymbol{C}^{c}(k) \tag{3.26}$$

If tension loading is assumed we can show $\boldsymbol{C^c}$ in terms of the response tensor **R**. It is given as the following equation.

$$\dot{C}^{c} = \dot{k}R \tag{3.27}$$

Also, from earlier the inelastic strain tensor is expressed in terms of a response tensor M.

$$\dot{\boldsymbol{\varepsilon}}^{\boldsymbol{\iota}} = \dot{k}\boldsymbol{M} \tag{3.28}$$

These response tensors are meant to introduce damage into the system in the proper directions. Applying the equations with the response tensors the dissipation function becomes the following:

$$\frac{1}{2}\boldsymbol{\sigma}:\boldsymbol{R}:\boldsymbol{\sigma} + \boldsymbol{\sigma}:\boldsymbol{M} - \frac{\partial A^{i}}{\partial k} \geq 0 \tag{3.29}$$

As stated earlier, the two response functions take the following form.

$$\boldsymbol{R} = \frac{\boldsymbol{\sigma}^{+}\otimes\boldsymbol{\sigma}^{+}}{\boldsymbol{\sigma}^{+}:\boldsymbol{\sigma}^{+}} - \alpha(\boldsymbol{I} - \boldsymbol{i}\otimes\boldsymbol{i}) \qquad \boldsymbol{M} = \beta\boldsymbol{\sigma} \tag{3.30}$$

The failure of the composite can be shown by introducing a damage function (*t*) to obtain a potential function (ψ).

$$\psi(\boldsymbol{\sigma}, k) = \frac{1}{2}\boldsymbol{\sigma}:\boldsymbol{R}:\boldsymbol{\sigma} + \boldsymbol{\sigma}:\boldsymbol{M} - \frac{1}{2}t^{2}(\boldsymbol{\sigma}, k) = 0 \tag{3.31}$$

The damage function can be represented in terms of a strength function and a shape function which describe the failure of the material.

$$t(\boldsymbol{\sigma}, k) = L(\boldsymbol{\sigma})q(k) \tag{3.32}$$

q is a shape function that is equal to 1 at the failure surface. L is a strength function that takes the following form.

$$L(\boldsymbol{\sigma}) = \frac{\boldsymbol{\sigma}:\boldsymbol{S}}{Tr(\boldsymbol{\sigma})} \tag{3.33}$$

S is a strength tensor, and the stress tensor and the trace of the stress tensor are again meant to use the proper strength properties for a given load path.

$$\boldsymbol{S} = \begin{bmatrix} F_{t1} \\ F_{t2} \\ F_{t3} \end{bmatrix} \tag{3.34}$$

The F coefficients in the strength tensor are scalar parameters that are related to the strengths of the materials in directions 1, 2, and 3. These can be solved for and determined by performing a simple monotonic uniaxial tensile load test in the corresponding directions.

With these response tensors and damage function established, the potential function $\psi(\boldsymbol{\sigma}, k)$ can be further developed.

$$\begin{aligned} \psi(\boldsymbol{\sigma}, k) = {} & \frac{1}{2}\frac{\boldsymbol{\sigma}:\boldsymbol{\sigma}\otimes\boldsymbol{\sigma}:\boldsymbol{\sigma}}{\boldsymbol{\sigma}:\boldsymbol{\sigma}} + \frac{1}{2}\alpha * \boldsymbol{\sigma}:\boldsymbol{I}:\boldsymbol{\sigma} - \frac{1}{2}\alpha * \boldsymbol{\sigma}:\boldsymbol{i}\otimes\boldsymbol{i}:\boldsymbol{\sigma} + \beta\boldsymbol{\sigma}:\boldsymbol{\sigma} \\ & - \frac{1}{2}\left(\frac{\boldsymbol{\sigma}:\boldsymbol{S}}{Tr(\boldsymbol{\sigma})}q(k)\right)^2 = 0 \end{aligned} \tag{3.35}$$

$$\psi(\boldsymbol{\sigma}, k) = \boldsymbol{\sigma}:\boldsymbol{\sigma} + \alpha * \boldsymbol{\sigma}:\boldsymbol{\sigma} - \alpha * Tr(\boldsymbol{\sigma})^2 + 2\beta\boldsymbol{\sigma}:\boldsymbol{\sigma} - \left(\frac{\boldsymbol{\sigma}:\boldsymbol{S}}{Tr(\boldsymbol{\sigma})}q(k)\right)^2 = 0 \tag{3.36}$$

$$\psi(\boldsymbol{\sigma}, k) = \boldsymbol{\sigma}:\boldsymbol{\sigma}(1 + \alpha + 2\beta) - \alpha * Tr(\boldsymbol{\sigma})^2 - \frac{1}{2}\left(\frac{\boldsymbol{\sigma}:S}{Tr(\boldsymbol{\sigma})}q(k)\right)^2 = 0 \tag{3.37}$$

To solve for the strength coefficients we can introduce uniaxial loading in direction 1. The potential function is reduced to the following equation.

$$\psi(\boldsymbol{\sigma}, k) = \begin{bmatrix} \sigma_1 \\ 0 \\ 0 \end{bmatrix}:\begin{bmatrix} \sigma_1 \\ 0 \\ 0 \end{bmatrix}(1 + \alpha + 2\beta) - \alpha * \left(Tr\begin{bmatrix} \sigma_1 \\ 0 \\ 0 \end{bmatrix}\right)^2 - \left(\frac{\begin{bmatrix} \sigma_1 \\ 0 \\ 0 \end{bmatrix}:\begin{bmatrix} F_{t1} \\ F_{t2} \\ F_{t3} \end{bmatrix}}{Tr\begin{bmatrix} \sigma_1 \\ 0 \\ 0 \end{bmatrix}}q(k)\right)^2 = 0 \tag{3.38}$$

This becomes

$$(1+2\beta)\sigma_1^2 - F_{t1}^2 q^2(k) = 0 \tag{3.39}$$

For monotonic loading and at the limit state, q(k) = 1 and $\sigma_1 = f_{t1} = tensile\ strength.$ The strength coefficient becomes

$$F_{t1} = f_{t1}(1+2\beta)^{0.5} \tag{3.40}$$

This can be done for uniaxial tests in directions 2 and 3 as well.

$$F_{t2} = f_{t2}(1+2\beta)^{0.5} \qquad F_{t3} = f_{t3}(1+2\beta)^{0.5} \tag{3.41}$$

These strength coefficients are then reintroduced into the potential function and are what gives the model strength anisotropy.

To incorporate fatigue into Wen's model, he introduces a softening function, F(n), that is assumed to be the form of a power function.

$$F(n) = n^A \tag{3.42}$$

A is a material parameter that can be solved for by solving for a uniaxial fatigue test. "n" is the number of load cycles. The potential function becomes the following equation.

$$\psi(\boldsymbol{\sigma},k) = \boldsymbol{\sigma}:\boldsymbol{\sigma}(1+\alpha+2\beta) - \alpha * Tr(\boldsymbol{\sigma})^2 - \frac{1}{2}\left(\frac{\boldsymbol{\sigma}:\boldsymbol{S}}{Tr(\boldsymbol{\sigma})} n^A q(k)\right)^2 = 0 \tag{3.43}$$

The softening function is introduced into the final term. Solving for the softening function the following is obtained.

$$n^A = \frac{\sigma_1}{f_{t1}} \tag{3.44}$$

$$A = \frac{\ln\left(\frac{\sigma_1}{f_{t1}}\right)}{\ln(n)} \tag{3.45}$$

So for a given fatigue loading test, A can be determined by using the applied stress and the number of cycles the cause failure.

The material parameter α can be determined by performing a monotonic equal-biaxial tension test in directions 1 and 2.

$$\alpha = 1 - \frac{1}{8}\left(\frac{\sigma_0}{f_{t1} + f_{t2}}\right)^{-2} \tag{3.46}$$

σ_0 is the applied stress in directions 1 and 2.

3.3.2. Numerical Simulation of Wen Model

Experimental data obtained by Smith and Pascoe (1989) is used to both obtain the required material parameters, and validate the effectiveness of the model. Using the equations provided in the previous section the material parameters A, α, and β can be obtained.

A is found by performing a uniaxial fatigue test. α is determined from a monotonic equal biaxial test. β is determined by measuring the inelastic strain of the material after unloading. The following table shows the values for the model parameters.

Known Values
f_{tx} = 238 Mpa f_{ty} = 257 Mpa α = 0.3841 B = 0.1 A = -0.0955

The numerical results in the paper are limited to the fatigue life and strain of the woven fabric composite. The following S-N curves are obtained solving for "n" (number of loading cycles) in the potential function. γ is the ratio between loading in direction 1 and direction 2. For example, for equal biaxial loading γ is equal to 1. The following equation is obtained and yields the ensuing S-N curves.

Figures 3.9, 3.10, and 3.11 are from solving for the number of cycles (n) in the potential function. The equation used in Figure 3.12 is obtained by solving for the applied stress from the potential function. The stress tensor and the final equations are seen below.

$$\boldsymbol{\sigma} = \begin{bmatrix} \sigma \\ \gamma\sigma \\ 0 \end{bmatrix} \qquad where\ \gamma = the\ biaxial\ stress\ ratio \tag{3.47}$$

$$n = \exp\left[\left(\frac{1}{2A}\right)\ln\left(\frac{\sigma^2(1+\gamma)^2(1+\gamma^2+2\beta+2\beta\gamma^2-2\alpha\gamma)}{(1+2\beta)(f_{t1}+\gamma f_{t2})^2}\right)\right] \tag{3.48}$$

$$\sigma = \left[\frac{(1+2\beta)(f_{t1}+\gamma f_{t2})^2 n^{2A}}{(1+\gamma^2+2\beta+2\beta\gamma^2-2\alpha\gamma)(1+\gamma)^2}\right]^{0.5} \tag{3.49}$$

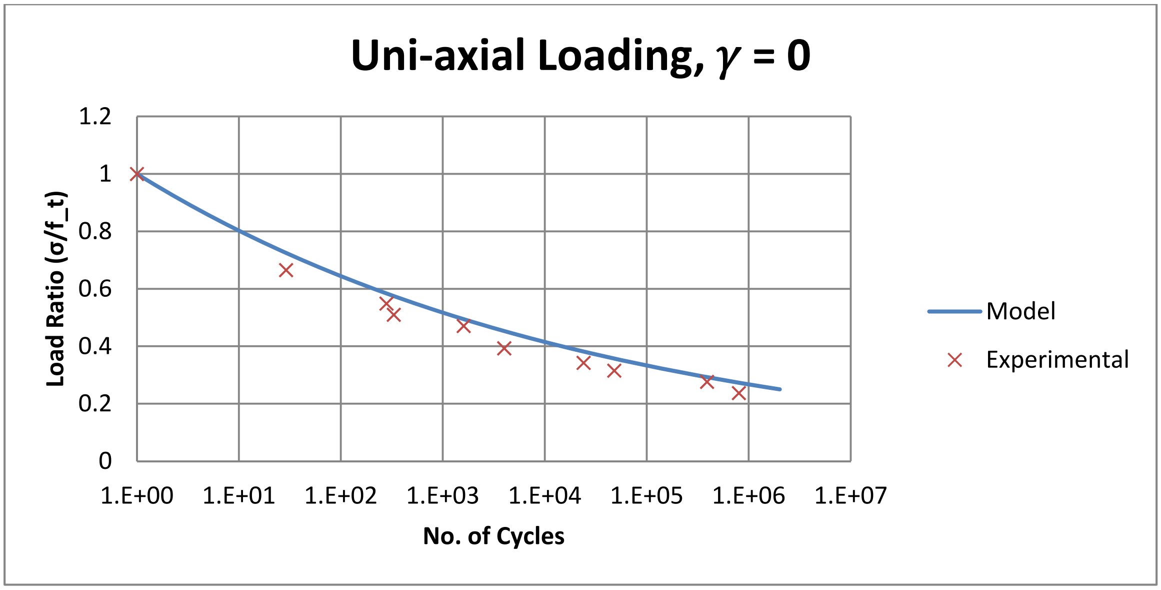

Fig. 3.9. Number of cycles to failure for a given load ratio (Uniaxial loading)

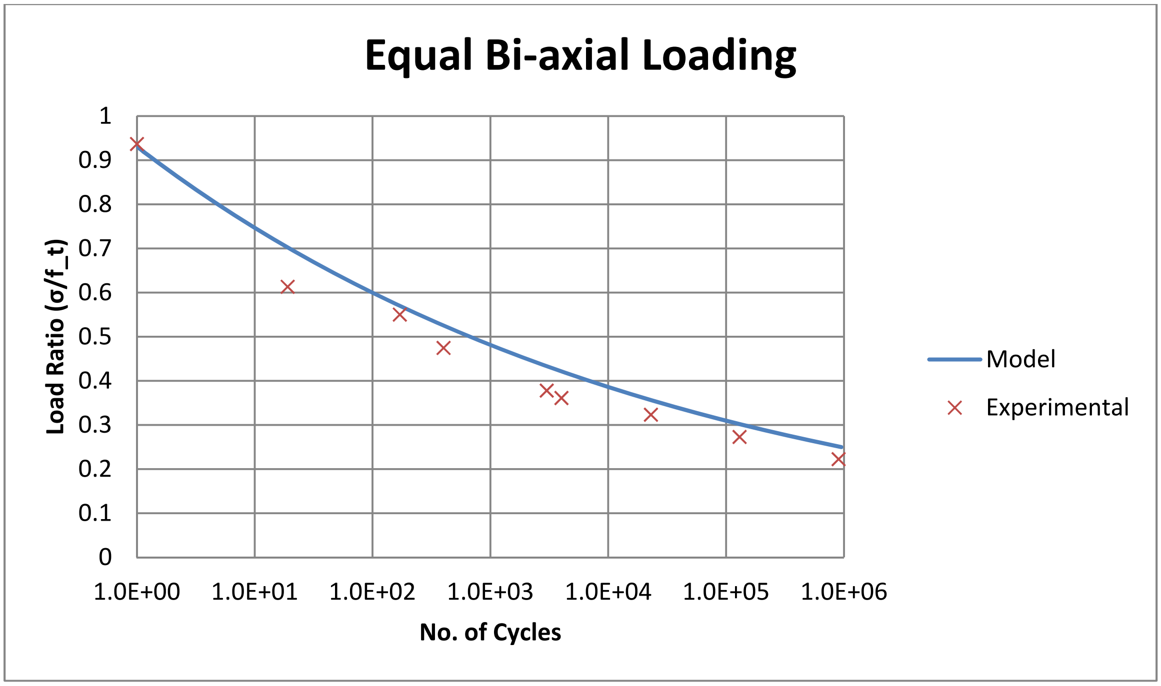

Fig. 3.10. Number of cycles to failure for a given load ratio (Equal-biaxial loading)

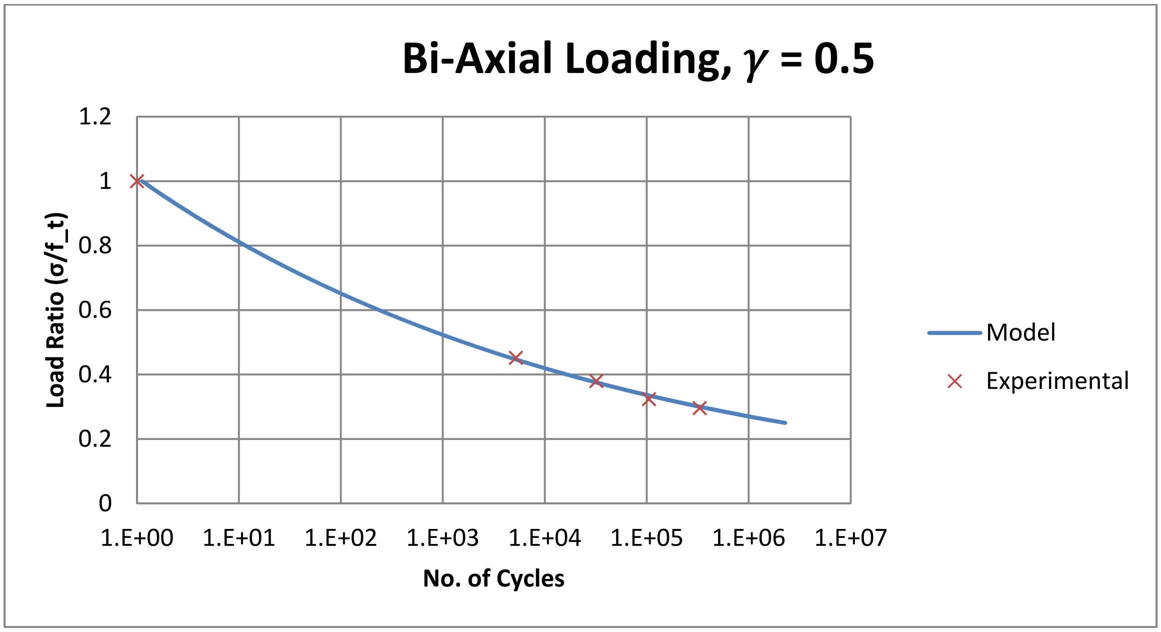

Fig. 3.11. Number of cycles to failure for a given load ratio (Biaxial loading)

One can see that the S-N curves presented above correlate very well to the experimental data. A failure surface can also be obtained if one solves for the applied stress in the potential function. For increasing values of "n" the failure surface is reduced. Figures with the failure surface can be seen in the figure below. The ability of the model to incorporate strength anisotropy can easily be seen in figure below.

The strain occurring in the composite can also be determined by solving for the effective compliance of the system by using the damage parameter, k. The damage parameter is defined by the following equation.

$$\frac{\partial k}{\partial n} = \frac{-An^{-A-1}}{E_0(1+\beta)} \qquad k = \frac{n^{-A}}{E_0(1+\beta)} \tag{3.50}$$

From this one can obtain the effective compliance tensor from the equation derived earlier.

$$\boldsymbol{C} = \boldsymbol{C_0} + k\boldsymbol{R} \tag{3.51}$$

With this equation, the total strain can be found.

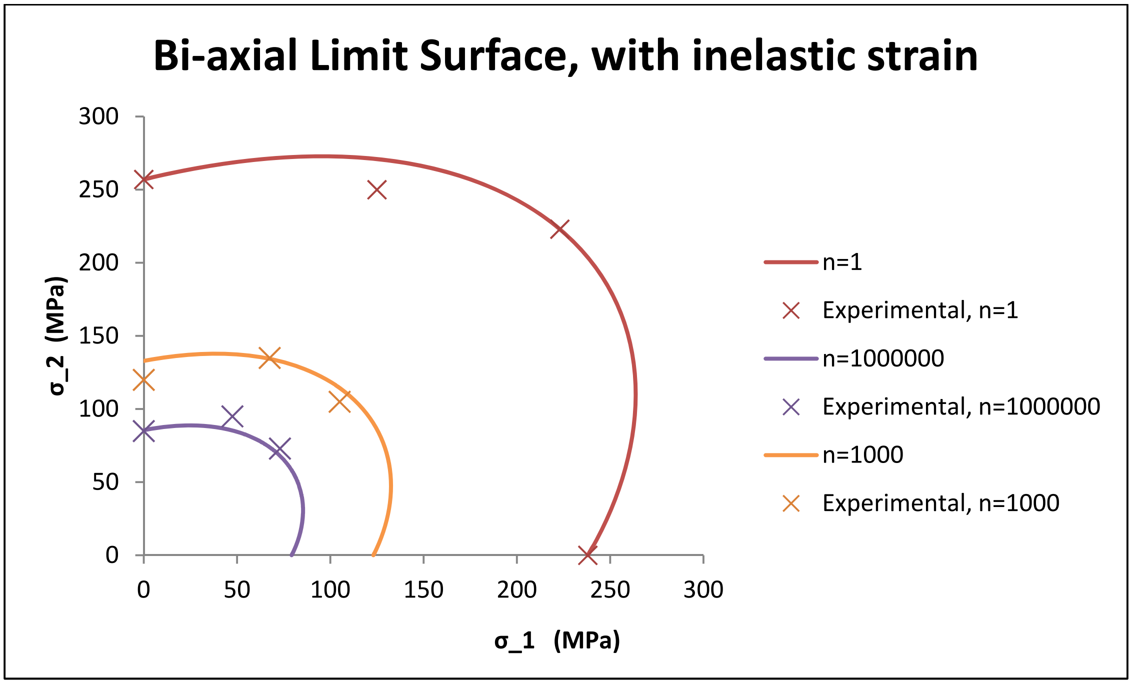

Fig. 3.12. Limit surface or varying number of load cycles

$$\boldsymbol{\varepsilon} = \boldsymbol{C}:\boldsymbol{\sigma} + \boldsymbol{\varepsilon_i} = \boldsymbol{C}:\boldsymbol{\sigma} + k\beta\boldsymbol{\sigma} \tag{3.52}$$

$$\boldsymbol{\varepsilon} = \boldsymbol{C^0}:\boldsymbol{\sigma} + k\left[\frac{\boldsymbol{\sigma}\otimes\boldsymbol{\sigma}}{\boldsymbol{\sigma}:\boldsymbol{\sigma}} - \alpha(\boldsymbol{I} - \boldsymbol{i}\otimes\boldsymbol{i})\right]:\boldsymbol{\sigma} + k\beta:\boldsymbol{\sigma} \tag{3.53}$$

$$where\ \boldsymbol{C^0} = \begin{bmatrix} \frac{1}{E_1} & -\frac{v_{21}}{E_2} & 0 \\ -\frac{v_{21}}{E_2} & \frac{1}{E_2} & 0 \\ 0 & 0 & \frac{1}{G_{12}} \end{bmatrix} \tag{3.54}$$

Using this equation a strain vector can be obtained for the corresponding loading directions. In this case, biaxial loading along the fiber directions is considered. Numerical results have been obtained for several load cases including: Uniaxial loading, equal biaxial loading, and biaxial loading with stress ratio equal to 0.5. In all load cases, the primary applied load is equal to half the tensile strength in the corresponding direction.

In the figures below the strain is seen to increase with the number of loading cycles. As damage accumulates in the material, components of the compliance tensor increases correspondingly, which results and increasing strains magnitudes. Attention should be placed on when failure occurs in the material shown by the red line in the figures.

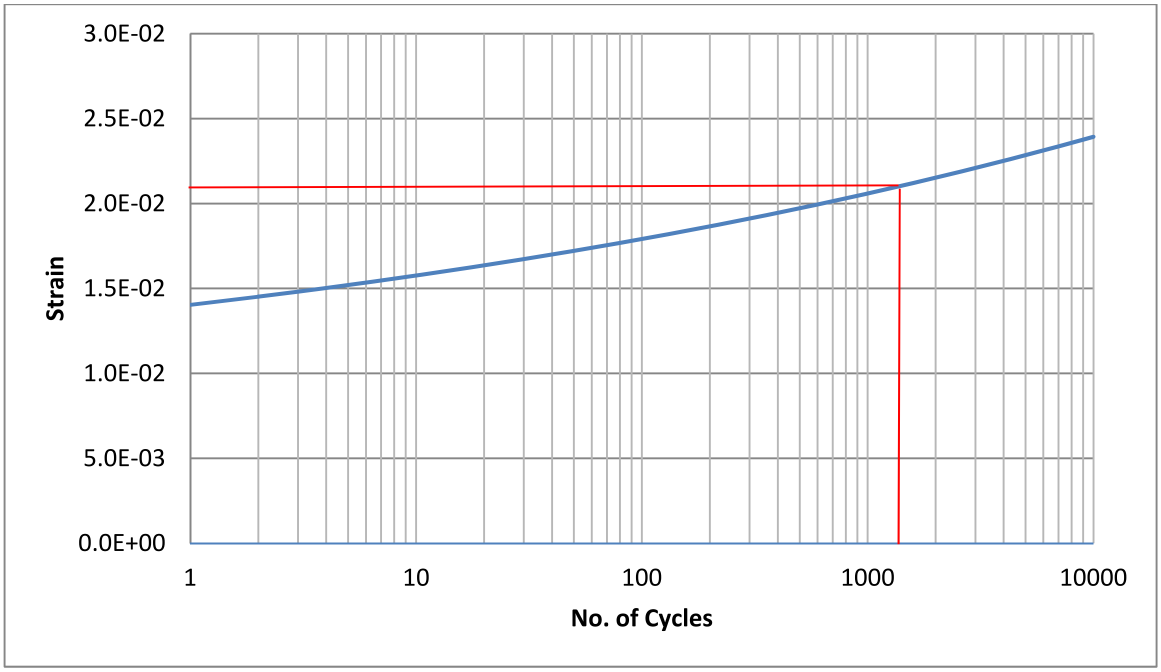

Fig. 3.13. Maximum strain per load cycle vs. number of loading cycles, uniaxial loading

In the figures above, the red lines are located at the number of loading cycles at which failure occurred for the given stress level. An interesting note is that for uniaxial loading the failure strain is about 1.5% while for equal biaxial loading the failure strain is about 0.9%. The failure strain for biaxial loading with load ratio equal to 0.5 is about 1.15%. These failure strains are quite close to those obtained by Smith and Pascoe in their experimental works. Something to note in the equal biaxial figure is that the model captures the anisotropic stiffness properties of the composite. The more flexible direction has slightly more strain. Similar trends are seen in the experimental data (Smith and Pascoe, 1989).

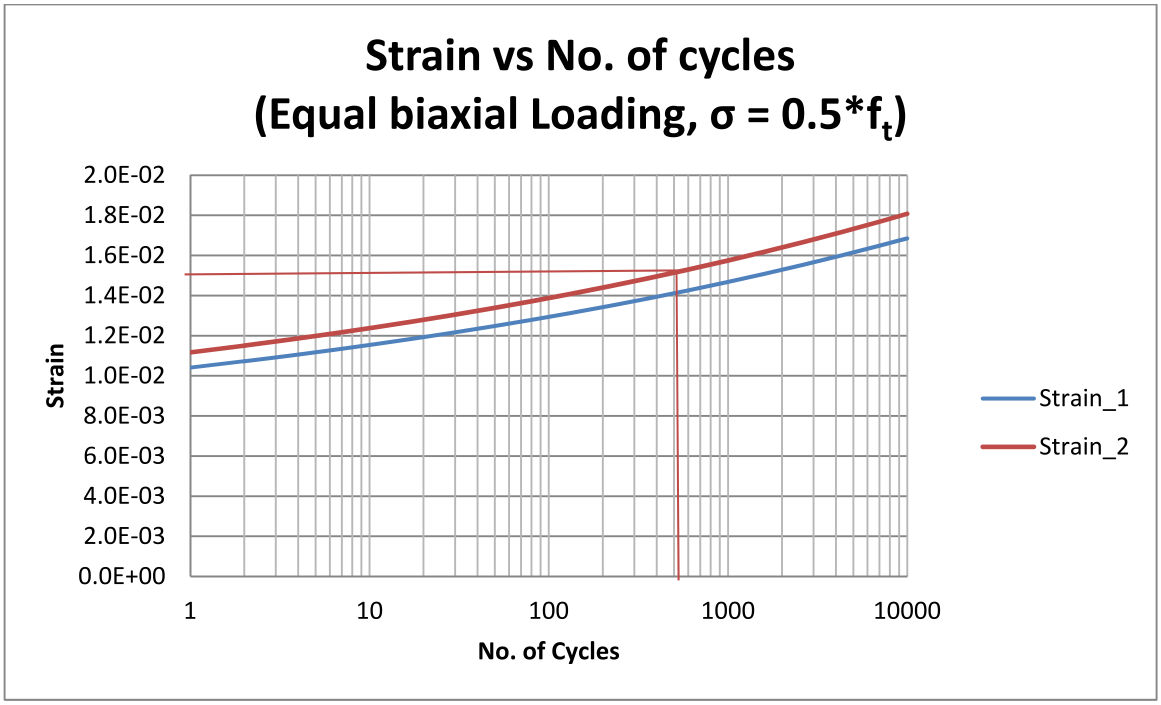

Fig 3.14. Maximum strain per load cycle vs. number of loading cycles, equal biaxial loading

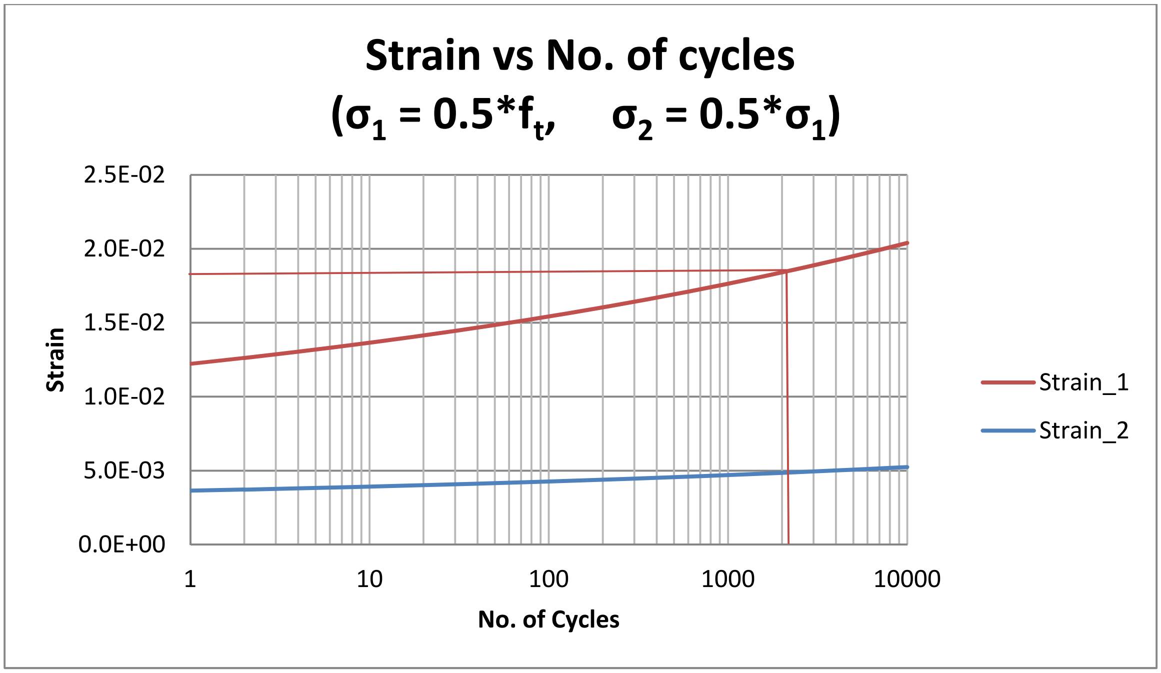

Fig. 3.15. Maximum strain per load cycle vs. number of loading cycles, biaxial loading

CHAPTER 4. THERMODYNAMICS AND DAMAGE MECHANICS

4.1. Introduction to Thermodynamics

In its most general form, thermodynamics is simply a branch of science that establishes relationships between types of energy and properties of systems in equilibrium, including mechanical, chemical, or electrical systems. Thermodynamic systems can be classified into two basic types of systems or processes, reversible and irreversible. An example of a reversible process relating to solid mechanics is the deformation of a perfectly elastic material. In a reversible system a single kinematic variable can define the state of a solid by relating the stresses and strains. In reality, solid materials undergo irreversible changes within their microstructure. For this condition, a single kinematic variable relating stresses and elastic strains cannot fully define the state of a solid in a local sense. A set of internal variables needs to be defined so that these irreversible processes, changes to the solids microstructure, can be fully accounted for and the state of the solid can be described.

The set of internal variables, or state variables, are related using two fundamental laws of thermodynamics: The first law of thermodynamics (conservation of energy) and the second law of thermodynamics (entropy law). This method for defining the state of a system was first used by Onsager (1931) and was expanded into continuum solid mechanics by many more researchers and scientists (Biot, 1954; Coleman and Gurtin, 1967; Kestin and Rice, 1970; Lubliner, 1972, 1980; Nemat-Nasser, 1976).

In this chapter the basic concepts of thermodynamics will first be defined, including Cauchy's first law of motion and the first and second laws of thermodynamics. Thermodynamic potentials will be defined using the Legendre Transformation and their relationship will be given. Relating these thermodynamic concepts a dissipation inequality will be established which can be used to describe the irreversible changes that are taking place within concrete's microstructure during loading. From this the state of damage within concrete can be established within a fourth order compliance tensor as established by Yazdani and Schreyer (1988)

4.1.1. Cauchy's First Law of Motion

The total force acting on a body is known to be a body force f_b and a surface (traction) force f_s.

$$\boldsymbol{f_t} = \boldsymbol{f_b} + \boldsymbol{f_s} \tag{4.1}$$

The body force can be found by integrating a vector field b(r, t) over its volume.

$$\boldsymbol{f_b} = \int_V \boldsymbol{b}\rho \, dV \tag{4.2}$$

V is the volume of the body, ρ is the density of the material, **r** is the position vector, and t is time.

In the same manner, the surface force is obtained by integrating a vector field **t**(r, **n**) acting on the surface of the body.

$$\boldsymbol{f_s} = \int_S \boldsymbol{t}(r, \boldsymbol{n}) dS \tag{4.3}$$

n is the unit normal vector in the above equation. From Cauchy's fundamental theorem we can say that at the surface of the body:

$$\boldsymbol{t} = \boldsymbol{\sigma} \cdot \boldsymbol{n} \tag{4.4}$$

where σ is the Cauchy stress tensor. We can also say that the total force is a function to the body's acceleration.

$$\boldsymbol{f_t} = \int\limits_V \boldsymbol{a}\rho dV = \int\limits_V \boldsymbol{b}\rho\, dV + \int\limits_S \boldsymbol{\sigma} \cdot \boldsymbol{n} dS \tag{4.5}$$

Applying the divergence theorem the surface integral is made into a volume integral:

$$\boldsymbol{f_t} = \int\limits_V \boldsymbol{a}\rho dV = \int\limits_V \boldsymbol{b}\rho\, dV + \int\limits_V \boldsymbol{\sigma} \cdot \nabla dV \tag{4.6}$$

In the equation above ∇ is the divergence operator. Using the equation above we can state Cauchy's first law of motion as the following:

$$\boldsymbol{a}\rho = \boldsymbol{b}\rho + \boldsymbol{\sigma} \cdot \nabla \tag{4.7}$$

4.2. Thermodynamic Formulation

4.2.1. First Law of Thermodynamics

The first law of thermodynamics deals with the conservation of energy in a given process. The total energy within a system is constant, although it may be present in different forms. Transfer or conversion of energy from one form to another is possible and dissipation of energy can occur, but the destruction of energy cannot happen. With respect to solid mechanics, total energy can be represented by mechanical energy and heat energy. It is shown in mathematical form in the following equation.

$$\dot{E} = P_{input} + Q_{input} \tag{4.8}$$

In the equation above P_{input} is the power input from mechanical work and Q_{input} is the heat change rate of the system. P_{input} is produced by the body force and surface force.

$$P_{input} = \int\limits_{V} \boldsymbol{b}\rho \cdot \boldsymbol{v}\, dV + \int\limits_{S} \boldsymbol{v} \cdot \boldsymbol{\sigma} \cdot \boldsymbol{n} dS \tag{4.9}$$

where v is a vector of the displacement rate. Again, with Gauss' divergence theorem the above equation becomes

$$P_{input} = \int\limits_{V} \boldsymbol{b}\rho \cdot \boldsymbol{v}\, dV + \int\limits_{V} (\boldsymbol{v} \cdot \boldsymbol{\sigma}) \cdot \nabla dV \tag{4.10}$$

Working with the right side of the equation above:

$$(\boldsymbol{v} \cdot \boldsymbol{\sigma}) \cdot \nabla = \mathrm{v} \cdot (\boldsymbol{\sigma} \cdot \nabla) + \mathrm{Tr}\big((\mathbf{v}\nabla) \cdot \boldsymbol{\sigma}\big) \tag{4.11}$$

$\mathrm{Tr}\big((\mathrm{V} \cdot \nabla) \cdot \sigma\big)$ is known as the trace of the vector within the parentheses and is the sum of the vectors individual components. Using the equation for Cauchy's law of motion we can get the following:

$$P_{input} = \int\limits_{V} \rho \boldsymbol{a} \cdot \boldsymbol{v}\, dV + \int\limits_{V} \mathrm{Tr}\big((\mathbf{v}\nabla) \cdot \boldsymbol{\sigma}\big) dV \tag{4.12}$$

$$P_{input} = \int\limits_{V} \rho \dot{\boldsymbol{v}} \cdot \boldsymbol{v}\, dV + \int\limits_{V} \mathrm{Tr}\big((\mathbf{v}\nabla) \cdot \boldsymbol{\sigma}\big) dV \tag{4.13}$$

Q_{input} can be assumed to be the sum of the heat rate from an internal source r and the heat flux q through the surface of the system. It is represented in the equation below:

$$Q_{input} = \int\limits_{V} r dV - \int\limits_{V} \boldsymbol{q} \cdot \boldsymbol{n}\, ds \tag{4.14}$$

Applying Gauss' Divergence Theorem the equation becomes

$$Q_{input} = \int\limits_V \boldsymbol{r} dV - \int\limits_V \boldsymbol{q} \cdot \nabla \, dV \tag{4.15}$$

With the equations above we can get a new expression for the rate of change of the energy in the system.

$$\dot{E} = \int\limits_V \rho \dot{\boldsymbol{v}} \cdot \boldsymbol{v} \, dV + \int\limits_V \mathrm{Tr}\big((\mathbf{v}\nabla) \cdot \boldsymbol{\sigma}\big) dV + \int\limits_V r dV - \int\limits_V \boldsymbol{q} \cdot \nabla \, dV \tag{4.16}$$

The total energy of a system can also be represented as the total kinetic energy and internal energy.

$$E = \int_V \frac{1}{2} \rho (\boldsymbol{v} \cdot \boldsymbol{v}) dV + \int_V \rho u dV \tag{4.17}$$

Or in its rate form:

$$\dot{E} = \frac{d}{dt} \int_V \left[\frac{1}{2} \rho (\boldsymbol{v} \cdot \boldsymbol{v}) + \rho u\right] dV = \int\limits_V \rho \dot{\boldsymbol{v}} \cdot \boldsymbol{v} \, dV + \int\limits_V \mathrm{\rho}\dot{\mathrm{u}} dV \tag{4.18}$$

Using the equations for the rate of change of power and heat input with the equation above we can obtain the rate of change of the internal energy:

$$\rho \dot{u} = \mathrm{Tr}\big((\mathbf{v}\nabla) \cdot \boldsymbol{\sigma}\big) + \mathrm{\rho r} - \mathbf{q} \cdot \nabla \tag{4.19}$$

The matrix v∇ can be decomposed into its symmetric and anti-symmetric parts, D (rate of deformation tensor) and W (rate of rotation tensor), respectively. The decomposition is as follows:

$$\begin{aligned} D &= \frac{1}{2} (\boldsymbol{v}\nabla + (\boldsymbol{v}\nabla)^T) \\ W &= \frac{1}{2} (\boldsymbol{v}\nabla - (\boldsymbol{v}\nabla)^T) \end{aligned} \tag{4.20}$$

For very small deformations which are applicable to this study, the rate of deformation tensor D can be assumed to be equal to the rate of strain tensor. Also $tr(W \cdot \boldsymbol{\sigma}) = 0$, therefore the equation for the rate of change of the internal energy becomes the following:

$$\rho \dot{\boldsymbol{u}} = \boldsymbol{\sigma} : \dot{\boldsymbol{\varepsilon}} + \rho r - \boldsymbol{q} \cdot \nabla \qquad (4.21)$$

":" is the tensor contraction operator in the above equation. It can be seen that the rate of change of the internal energy per unit volume is affected by three parts. The mechanical work input into the system is represented by $\boldsymbol{\sigma} : \dot{\boldsymbol{\varepsilon}}$, the heat input by an internal heat source is ρr, and the heat input provided by the heat flow through the boundary of the system is represented by $\boldsymbol{q} \cdot \nabla$.

4.2.2. The Second Law of Thermodynamics

The first law of thermodynamics states that the kinetic and internal energy can be transformed from one form to the other and that no energy is lost to friction or other dissipative mechanisms. This is not the case in reality because friction and other dissipative processes are mostly irreversible. The second law of thermodynamics accounts for this through the Clausius-Duhem inequality.

The second law of thermodynamics states that the rate of increase of entropy in a system must be equal to or greater than the rate at which entropy is added by heat flux through the boundary surface and by a external heat source. The rate entropy that is added is considered to be the rate of heating divided by the absolute temperature. The Clausius-Duhem Inequality is

$$\frac{d}{dt} \int_V \rho s dV \geq \int_V \frac{\rho r}{\theta} dV - \int_S \frac{\boldsymbol{q}}{\theta} \cdot \boldsymbol{n} \, dS \qquad (4.22)$$

In the equation above s is the entropy and θ is the absolute temperature. If the equation above is equal then a reversible process is implied. Since the volume is arbitrary, and applying the divergence theorem:

$$\int_V \rho \dot{s} dV \geq \int_V \frac{\rho r}{\theta} dV - \int_S \left(\frac{\boldsymbol{q}}{\theta}\right) \boldsymbol{\nabla}\, dV \tag{4.23}$$

or

$$\rho \dot{s} \geq \frac{\rho r}{\theta} - \left(\frac{\boldsymbol{q}}{\theta}\right) \cdot \boldsymbol{\nabla} \tag{4.24}$$

A variable $\dot{\eta}$ representing the internal entropy production rate per unit mass is defined. This can be thought of as additional entropy that is not occurring from the internal heat source or heat flux through the system boundary.

$$\rho \dot{\eta} = \rho \dot{s} - \frac{\rho r}{\theta} + \left(\frac{\boldsymbol{q}}{\theta}\right) \cdot \nabla \geq 0 \tag{4.25}$$

As stated previously, the inequality implies that if $\rho \dot{\eta} = 0$ then the process is reversible. With some additional formulation the equation above becomes

$$\rho \dot{\eta} = \rho \dot{s} - \frac{\rho r}{\theta} + \frac{(\nabla \cdot \boldsymbol{q})}{\theta} - \frac{(\nabla \theta) \cdot \mathbf{q}}{\theta^2} \geq 0 \tag{4.26}$$

Furthermore, using the equation for the rate of change of the internal energy we can write the following expression:

$$\dot{\eta} = \dot{s} - \frac{\dot{u}}{\theta} + \frac{\boldsymbol{\sigma} : \dot{\boldsymbol{\varepsilon}}}{\rho \theta} - \frac{\boldsymbol{q} \cdot (\theta \nabla)}{\rho \theta^2} \geq 0 \tag{4.27}$$

4.2.3. Thermodynamic Potentials

The Legendre Transformation is used to obtain varying thermodynamic potentials including Hemholtz Free Energy (A), enthalpy (h), and Gibbs Free Energy (G). The relationship between the thermodynamic potentials is

$$u - A + g - h = 0 \tag{4.28}$$

where u is the internal energy, A is the Helmholtz free energy, g is the free enthalpy, and h is the enthalpy (Lin, 1992). Each thermodynamic potential is defined as follows:

$$A = u(s, \boldsymbol{v_i}) - \theta s \tag{4.29a}$$

$$h = u(s, \boldsymbol{u_i}) - \boldsymbol{\tau_i v_i} \tag{4.29b}$$

$$g = h(s, \boldsymbol{\tau_i}) - \theta s \tag{4.29c}$$

$$G = Gibbs\ Free\ Energy = -g \tag{4.29d}$$

In the equations above v_i represents a set of state variables describing the state of the material. For isothermal processes with small deformations Gibbs Free Energy, Hemholtz Free Energy, and the internal energy can be related in the following way (Yazdani and Schreyer, 1988):

$$A(\boldsymbol{\varepsilon}, \theta, \boldsymbol{v}_i) = U(\boldsymbol{\varepsilon}, s, \boldsymbol{v_i}) - \theta s \tag{4.30}$$

$$G(\boldsymbol{\sigma}, \theta, \boldsymbol{v}_i) = \boldsymbol{\sigma}\!:\boldsymbol{\varepsilon} - A(b, \theta, \boldsymbol{v_i}) \tag{4.31}$$

Using the equations for the thermodynamic potentials and making the assumption that τ_i equals the Cauchy stress tensor, and that for small deformations v_i equals the strain tensor (Yazdani and Schreyer, 1988; Wen, 2011) we can obtain the following:

$$u = \boldsymbol{\sigma}\!:\boldsymbol{\varepsilon} + \theta s - G \tag{4.32}$$

$$\dot{u} = \dot{\boldsymbol{\sigma}}\!:\boldsymbol{\varepsilon} + \boldsymbol{\sigma}\!:\dot{\boldsymbol{\varepsilon}} + \dot{\theta} s + \theta \dot{s} - \dot{G} \tag{4.33}$$

Inserting the equation above into the Clausius-Duhem inequality the following equation is obtained

$$\dot{G} - \dot{\boldsymbol{\sigma}}\!:\boldsymbol{\varepsilon} - \dot{\theta} s - \frac{\boldsymbol{q} \cdot \theta \nabla}{\theta} \geq 0 \tag{4.34}$$

Gibbs free energy can be shown as a function of the stress, absolute temperature, and damage. Differentiating we obtain

$$\dot{G}(\boldsymbol{\sigma},\theta,k)=\frac{\partial G}{\partial \boldsymbol{\sigma}}:\dot{\boldsymbol{\sigma}}+\frac{\partial G}{\partial \theta}\dot{\theta}+\frac{\partial G}{\partial k}\dot{k} \tag{4.35}$$

Putting this into the equation for the Clausius-Duhem inequality

$$\left(\frac{\partial G}{\partial \boldsymbol{\sigma}}-\boldsymbol{\varepsilon}\right):\dot{\boldsymbol{\sigma}}+\left(\frac{\partial G}{\partial \theta}-s\right)\dot{\theta}+\frac{\partial G}{\partial k}\dot{k}-\frac{\boldsymbol{q}\cdot\theta\nabla}{\theta}\geq 0 \tag{4.36}$$

Since this inequality must be greater than or equal to zero for arbitrary $\dot{\sigma}$ and $\dot{\theta}$ we can ascertain the following:

$$\frac{\partial G}{\partial \boldsymbol{\sigma}}-\boldsymbol{\varepsilon}=0 \tag{4.37}$$

$$\frac{\partial G}{\partial \theta}-s=0 \tag{4.38}$$

$$\frac{\partial G}{\partial k}\dot{k}-\frac{\boldsymbol{q}\cdot\theta\nabla}{\theta}\geq 0 \tag{4.39}$$

The last equation is formally known as the dissipation inequality and illustrates dissipative mechanisms. If there is no change in damage, the first term is zero and the second term must be negative. This follows a basic principle of thermodynamics, that is, heat travels from high to low temperatures (Thapa, 2010). The following equations can also be ascertained.

$$\frac{\partial G}{\partial \boldsymbol{\sigma}}=\boldsymbol{\varepsilon} \tag{4.40}$$

$$\frac{\partial G}{\partial \theta}=s \tag{4.41}$$

This shows that differentiating Gibbs Free Energy with respect to stress or temperature represents a potential for strain or entropy, respectively. Further, we can claim that differentiating G twice with respect to stress yields a material compliance tensor C (refer to the first differentiation equaling the strain). Also from the above set of equations we can define a thermal expansion tensor β and the specific heat under a constant voluve as ζ (Wen, 2010).

$$\frac{\partial^2 G}{\partial \boldsymbol{\sigma}^2} = \boldsymbol{C}(k) \tag{4.42}$$

$$\frac{\partial^2 G}{\partial \boldsymbol{\sigma} \partial \theta} = \boldsymbol{\beta}(k) \tag{4.43}$$

$$\theta \frac{\partial^2 G}{\partial \theta^2} = \zeta(k) \tag{4.44}$$

In Yazdani and Schreyer's study (1988), the effect of temperature on the continuum is neglected with low frequency loading however for this formulation the effect of the temperature on the concrete's performance is a key issue. With some further formulation of the set of equations presented above a form of Gibbs Free Energy can be obtained that includes the effect of stress, temperature, and damage on the material's performance.

$$G(\boldsymbol{\sigma}, k, \theta) = \frac{1}{2}\boldsymbol{\sigma}: C(k): \boldsymbol{\sigma} + \boldsymbol{\sigma}: \boldsymbol{\varepsilon}^{\boldsymbol{i}}(k) + \boldsymbol{\sigma}: \beta(k)(\theta - \theta_0) - A^i(k) \tag{4.45}$$

In the equation above θ_0 is the reference temperature and $A^i(k)$ is Hemholtz Free Energy. In this work the temperature that occurs during the freeze-thaw cycles are assumed to be in the range of $20 - 45°$ F and will have a negligible effect on the concrete. Therefore it is not necessary to include the thermal effects in the equation for Gibbs Free Energy. The vast majority of the damage that will be caused by these environmental effects will be from the freeze-thaw moisture expansion and not the effect the lower temperatures will have on the actual concrete specimen. With this assumption in mind Gibbs Free Energy can be reduced to

$$G(\boldsymbol{\sigma}, k) = \frac{1}{2}\boldsymbol{\sigma}: \boldsymbol{C}(k): \boldsymbol{\sigma} + \boldsymbol{\sigma}: \boldsymbol{\varepsilon}^{\boldsymbol{i}}(k) - A^i(k) \tag{4.46}$$

This is the same form of Gibbs Free Energy used in the Yazdani and Schreyer model (1988), Yazdani model (1993), and Wen model (2011).

4.2.4. Consequences of the Second Law of Thermodynamics

The internal dissipation inequality can be represented by Gibbs Free Energy as the following if the effect of heat flow is neglected:

$$\psi(\boldsymbol{\sigma},k)\dot{k} \geq 0 \tag{4.47}$$

where

$$\psi(\boldsymbol{\sigma},k) = \frac{\partial G(\boldsymbol{\sigma},k)}{\partial k} \tag{4.48}$$

It is logical to assume that damage is an irreversible process, or that concrete cannot heal itself, which is expressed in the following equations:

$$\dot{k} \geq 0 \tag{4.49}$$

With the assumption that damage is irreversible and using the equation for the dissipation inequality above two restrictions can be given

$$1)\ if\ \psi < 0 \quad \rightarrow \quad \dot{k} = 0 \tag{4.50}$$

$$2)\ if\ \psi \geq 0 \quad \rightarrow \quad \dot{k} \geq 0 \tag{4.51}$$

With the idea that Gibbs Free Energy describes the energy captured in a material from loading and resultant strains one can say that in the absence of viscous behavior that $\psi \leq 0$. We can than say that if $\psi = 0$ that the material has reached a point on that particular loading path that elastic behavior stops and damage begins to occur. So it can be said that $\psi < 0$ is considered an elastic region and $\psi = 0$ is a damage surface enclosing that region. Therefore the following criteria can be stated:

$$1)\ \psi = 0,\ \frac{\partial\psi}{\partial\boldsymbol{\sigma}}:\dot{\boldsymbol{\sigma}} > 0 \quad \rightarrow \quad \dot{k} > 0 \tag{4.52}$$

$$2)\ Otherwise \quad \rightarrow \quad \dot{k} = 0 \tag{4.53}$$

The softening regime of concrete cannot be modeled using a stress based formulation. Consider at a given stress level, two different strains are possible, one in the hardening regime and one in the softening regime after the maximum load is reached. For this reason a strain-space formulation is used to model the entire range of stress-strain behavior, both hardening and softening. Using the notation from the Yazdani and Schreyer model (1988) the total strain is given as

$$\boldsymbol{\varepsilon} = \boldsymbol{\varepsilon_0} + \boldsymbol{\varepsilon_D} + \boldsymbol{\varepsilon_r} = \boldsymbol{\sigma}\colon C(k) + \boldsymbol{\varepsilon_r} \tag{4.54}$$

where *C(k)* is a fourth order compliance tensor. Since $\boldsymbol{\varepsilon_0}$ is considered to be the elastic part of strain which coincides with the undamaged compliance tensor and $\boldsymbol{\varepsilon_D}$ is considered additional strain resulting from damage accumulation in the material and coincides with the additional compliance in the material resulting from damage the following can be given:

$$\boldsymbol{C}(k) = \boldsymbol{C}^{\boldsymbol{0}} + \boldsymbol{C}^{c}(k) \tag{4.55}$$

$$\dot{\boldsymbol{\varepsilon}}_{\boldsymbol{D}}(k) = \dot{\boldsymbol{C}}^{c}(k)\colon \boldsymbol{\sigma} \tag{4.56}$$

$\dot{\boldsymbol{C}}^{c}(k)$ is defined by a fourth order response tensor as the following:

$$\dot{\boldsymbol{C}}^{c}(k) = \dot{k}\boldsymbol{R}(\boldsymbol{\sigma}) \tag{4.57}$$

With this being said the mathematical form of the damage surface can be given as

$$\psi(\boldsymbol{\sigma}, k) = \frac{1}{2}\boldsymbol{\sigma}\colon \frac{\partial \boldsymbol{C}^{c}(k)}{\partial k}\colon \boldsymbol{\sigma} + \frac{\partial \boldsymbol{\varepsilon}^{r}(k)}{\partial k}\colon \boldsymbol{\sigma} - \frac{\partial A^{i}(k)}{\partial k} \geq 0 \tag{4.58}$$

The formulation of $\dot{\boldsymbol{C}}^{c}(k)$, $\dot{\boldsymbol{\varepsilon}}_{r}(k)$, and the kinetic relations are established in the next section. Setting $\psi(\boldsymbol{\sigma}, k) = 0$ a surface is defined (termed the damage surface) using a damage function, t. Such a surface is capable of describing the onset of damage accumulation and is given as the following equation:

$$\psi(\boldsymbol{\sigma}, k) = \frac{1}{2}\boldsymbol{\sigma}\colon \frac{\partial \boldsymbol{C}^{c}(k)}{\partial k}\colon \boldsymbol{\sigma} + \frac{\partial \boldsymbol{\varepsilon}^{r}(k)}{\partial k}\colon \boldsymbol{\sigma} - \frac{1}{2}t^{2}(\boldsymbol{\sigma}, k) = 0 \tag{4.59}$$

Using the thermodynamic principles discussed in this chapter as the foundation, a damage mechanics model based on Yazdani’s model (1993) and Wen’s model (2011) is presented in Chapters 5 and 6.

CHAPTER 5. FATIGUE MODELING OF CONCRETE USING THE BOUNDING SURFACE APPROACH

5.1. Introduction

The fatigue life of a material is a popular method of describing the performance of a material over its service life. For designers, it is beneficial to establish some failure criteria pertaining to fatigue processes. This information is commonly conveyed in the form of S-N curves which relate the residual strength of a material to the number of cyclic loads being applied. It is natural then that the model presented in this paper should be capable of producing such S-N curves which can accurately portray the failure of concrete for a given number of cyclic loads.

Though there is an abundance of experimental data available describing the fatigue behaviour of plain concrete the vast majority is for uniaxial load cases only. There have been some researchers, including Nelson et al. (1988) and Subramaniam and Shah (2003) that have investigated the fatigue performance of concrete for multiaxial loading, but further experimental research on multiaxial fatigue behaviour of concrete would be beneficial to this field.

5.1.1. Bounding Surface Approach

In this chapter a simple method for modeling monotonic and fatigue loading processes utilizing a bounding surface approach is proposed. In this approach the limit surface (LS) is considered to be a unique case when the number of cyclic loads is equal to one, known as monotonic loading.

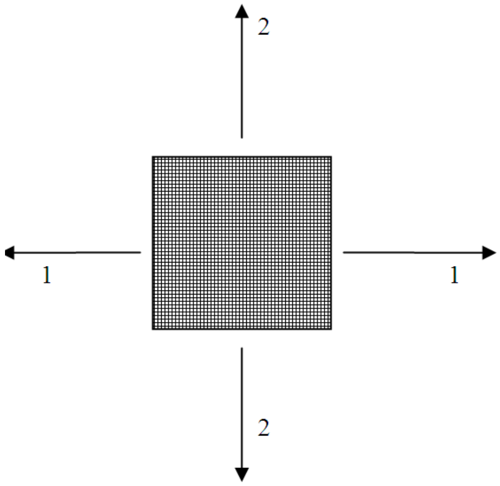

Fig. 5.1. Material element with loading directions 1 and 2 (Wen et al. 2012)

The bounding surface approach is explained in the following paragraphs in short detail. Consider the material element shown in Figure 5.1 and its corresponding limit surface (LS) in biaxial stress space shown in Figure 5.2. As stated previously, the LS corresponds to monotonic loading. This surface represents the ultimate strength of the material under monotonic loading under a variety of biaxial load combinations. As the number of cyclic loads increase, the strength of the material will decrease, which is represented by a reduction, or inward collapse, of the LS. In this paper the collapsing of the LS creates new residual strength surfaces (RS) depending on the level of stress and the number of load cycles. One can see that as the number of cyclic loads increases, shown for the number of cyclic loads n2 > n1, the RS continues to collapse further, representing further strength reduction of the material. At some point failure is reached. This is shown in Figure 5.2 as the failure surface (FS) which corresponds to the case when n = N. N is known as the fatigue life of the material as is a common way to demonstrate the fatigue behavior of materials.

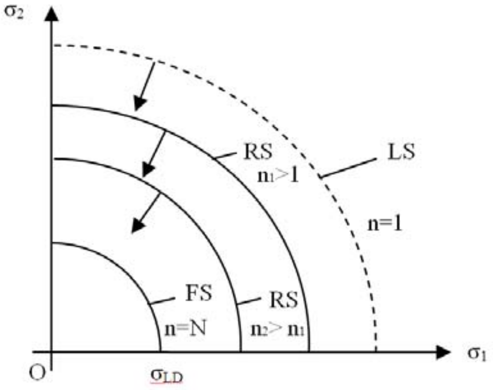

Fig. 5.2. Schematic representation of bounding surfaces in biaxial stress space (Wen et al. 2012)

The aim in this chapter is to utilize an effective constitutive model to obtain a reasonable limit surface based on the principles of mechanics and thermodynamics. Finally, the model should be capable of obtaining a final failure surface when the fatigue life of the material is met.

The model presented in the following sections is regarded as an extension to the work of Yazdani (1993) and Wen (2011). The bounding surface approach and damage mechanics theory are combined to provide a unified method of modeling concrete in the presence of fatigue loading.

In the following sections the bounding surface approach will be applied to the monotonic model discussed in the previous chapter. Several numerical examples will be presented and a sensitivity analysis will be conducted on the model through which the effect of various model parameters on the model output can be seen.

5.2. Formulation of the Model with the Bounding Surface Approach

Following the general formulation presented in Yazdani (1993) several assumptions are made in the development of the model. Loading is assumed to be at a low frequency so that thermal effects can be ignored. Furthermore, it is assumed that neighboring equilibrium states exist for all irreversible processes concerned herein. With these assumptions in mind, and for a stress space formulation, Gibbs Free Energy takes the following form:

$$G(\sigma, k) = \frac{1}{2}\boldsymbol{\sigma}:\boldsymbol{C}(k):\boldsymbol{\sigma} + \boldsymbol{\sigma}:\boldsymbol{\varepsilon^i}(k) - A^i(k) \tag{5.1}$$

where ***C*** is the compliance tensor, ***σ*** is the stress tensor, $\boldsymbol{\varepsilon}^i$ is the irrecoverable strain, *k* is a scalar quantity for damage, and A^i is a scalar function associated with the surface energy of microcracks. The symbol ":" represents a tensor contraction operator. ***C*** is made up of two parts:

$$\boldsymbol{C}(k) = \boldsymbol{C^0} + \boldsymbol{C}^c(k) \tag{5.2}$$

where $\boldsymbol{C}^0$ and $\boldsymbol{C}^c$ are the undamaged compliance tensor of the material and the added flexibility associated with the accumulation of damage, *k*, respectively. The rate form of the added flexibility tensor and irrecoverable strain are defined by a fourth order and second order compliance tensor, ***R*** and ***M***, respectively.

$$\dot{\boldsymbol{C}}(k) = \dot{k}\boldsymbol{R} \tag{5.3}$$

$$\dot{\boldsymbol{\varepsilon}}^{\boldsymbol{i}}(k) = \dot{k}\boldsymbol{M} \tag{5.4}$$

Following the standard argument provided in Yazdani (1993) and Wen and Yazdani (2012) the following form of the damage surface is obtained:

$$\psi = \frac{1}{2}\boldsymbol{\sigma}:\boldsymbol{R}:\boldsymbol{\sigma} + \boldsymbol{M}:\boldsymbol{\sigma} - \frac{1}{2}t^2(k) = 0 \tag{5.5}$$

where *t* is a strength function and is defined as

$$t^2(\boldsymbol{\sigma}, k) = 2\left[\frac{\partial A^i}{\partial k} + g^2(\boldsymbol{\sigma}, k)\right] \tag{5.6}$$

g^2 is some scalar function. Wen (2011) notes that as long as *t* can be obtained experimentally, the determination of the individual components, A^i and *g*, are not necessary.

Further definition of the response tensors is necessary in order to obtain an explicit equation for the damage surface. Identifying damage modes I and II; we propose the following damage response tensors as:

$$R_I = \frac{\boldsymbol{\sigma}^+ \otimes \boldsymbol{\sigma}^+}{\boldsymbol{\sigma}^+ : \boldsymbol{\sigma}^+} + \gamma H(\lambda_1)(\boldsymbol{I} - \boldsymbol{i} \otimes \boldsymbol{i}) \tag{5.7}$$

In eq. (7) σ^+ is the positive cone of the stress tensor, "$\otimes$" is the tensor operator, γ is a material parameter, $H(\lambda_1)$ is defined as the heavyside function of the maximum eigenvalue of σ^+, I and i are the fourth and second order identity tensors, respectively. The form of the tensile part of M is proposed as

$$\boldsymbol{M_I} = \beta_1 \boldsymbol{\sigma}^+ \tag{5.8}$$

where β_1 is a non-negative material parameter. This form of $\boldsymbol{M_I}$ means that for this model, irrecoverable strain under tension loading occurs only in the direction of loading. For the compression mode of cracking the response tensor $\boldsymbol{R_{II}}$ is given as the following:

$$\boldsymbol{R}_{II}^{d} = \frac{\tilde{\boldsymbol{\sigma}} \otimes \tilde{\boldsymbol{\sigma}}}{\tilde{\boldsymbol{\sigma}} : \tilde{\boldsymbol{\sigma}}} + \alpha H(-\lambda_3)(\mu \boldsymbol{I} - \boldsymbol{i} \otimes \boldsymbol{i}) \tag{5.9}$$

$$\tilde{\boldsymbol{\sigma}} = \boldsymbol{\sigma} - \boldsymbol{\lambda_2 i} \tag{5.10}$$

In Eq. (5.9) and (5.10), λ_2 is the maximum eigenvalue of $\boldsymbol{\sigma}^-$, and λ_3 denotes the minimum eigenvalue of $\boldsymbol{\sigma}$. $\boldsymbol{M_{II}}$ is then supposed as

$$\boldsymbol{M_{II}} = \boldsymbol{S}^- + \beta_2 \boldsymbol{S}^+ \tag{5.11}$$

where $\boldsymbol{S}^-$ and $\boldsymbol{S}^+$ are the negative and positive cones of the deviatoric part of $\boldsymbol{\sigma}^-$, respectively, and β_2 is a material parameter that is greater than one. With the response tensors defined and using Eq. (5.5) the damage surface becomes the following in biaxial stress space:

$$\begin{aligned}\psi(\boldsymbol{\sigma}, k) = \tfrac{1}{2}(1+\beta_1)\boldsymbol{\sigma}^{+}:\boldsymbol{\sigma}^{+} + \tfrac{1}{2}\boldsymbol{\sigma}^{-}:\frac{\tilde{\boldsymbol{\sigma}}\otimes\tilde{\boldsymbol{\sigma}}}{\tilde{\boldsymbol{\sigma}}:\tilde{\boldsymbol{\sigma}}}:\boldsymbol{\sigma}^{-} + \tfrac{1}{2}\left(\gamma H(\lambda_1) + \alpha H(-\bar{\lambda})\right)\boldsymbol{\sigma}:\boldsymbol{\sigma} - \\ \tfrac{1}{2}\left(\gamma H(\lambda_1) + \alpha H(-\bar{\lambda})\right) tr^2(\boldsymbol{\sigma}) + (\boldsymbol{S}^{-} + \beta_2\boldsymbol{S}^{+}):\boldsymbol{\sigma} - \tfrac{1}{2}t^2\,(k) = 0\end{aligned} \tag{5.12}$$

5.2.1. Softening Function

In this section two softening functions are proposed which gives the materials residual strength for a given number of load cycles. It will be seen from the experimental data presented in this section that the softening function is most effective when given in the form of a power function. It will be seen that the function proposed by Wen (2011) describes the softening behavior of a material as only a function of the number of cyclic loads. It is seen that this is not the case for concrete as for fatigue loading the residual strength is reduced at a greater rate for biaxial compression load cases than for uniaxial compression load cases. It is logical than that the softening function should be a function of both the number of load cycles as well as the load path. This is the approach taken by this study. In the figures below, both softening functions will be compared and it is seen that the softening function that takes both the number of load cycles as well as the load path into consideration is better suited to predict the fatigue behavior of concrete for multiaxial loading.

Utilizing a similar argument as Wen (2011), a softening function *f(n)* can be defined that effectively reduces the strength of concrete as the number of loading cycles increases. As the softening function affects the strength properties of the material, it is therefore logical to incorporate it into the strength function, *t*. For uniaxial compression and at the limit state the following is obtained from Eq. (5.12):

$$t^2(\boldsymbol{\sigma}, k) = \frac{7}{3} f_c^2 f^2(n) \tag{5.13}$$

which can be shown to result in our expression for the softening function as

$$f(n) = \frac{\sigma}{f_c} \tag{5.14}$$

Eq. (5.14) shows that the softening function can be considered as the ratio of the residual strength after *n* cyclic loads and the ultimate compressive strength under monotonic loading. As previously stated, many researchers have concluded that the strength of concrete has a logarithmic relationship with the number of loading cycles (Figure 5.3).

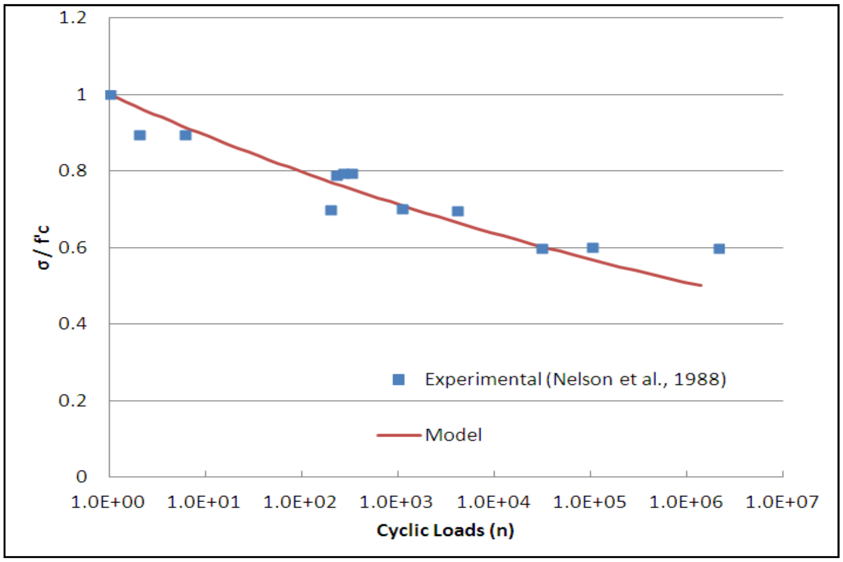

Fig. 5.3. Residual strength vs. number of cyclic loads for stress ratio 1:0 (uniaxial compression)

Guided by the experimental results, two softening functions (one solely as a function of the number of load cycles and the other a function of both the number of load cycles and the load path) are shown below in the form of a power function:

$$f(n) = n^A \tag{5.15}$$

$$f(\boldsymbol{\sigma}, n) = n^{\left[\left(\frac{tr^2(\boldsymbol{\sigma})}{\boldsymbol{\sigma}:\boldsymbol{\sigma}}\right)^B A\right]} \tag{5.16}$$

where A and B are material parameters that can be obtained by solving for it from the damage surface, Eq. (5.12), under uniaxial compression and equal biaxial compression, respectively.

$$A = \frac{1}{\ln{(n)}} \ln\left(\frac{\sigma}{f_c}\right) \tag{5.17}$$

$$B = \frac{1}{\ln{(2)}} \ln\left\{ [\ln(n)\, A]^{-1} \ln\left[\left(\frac{3}{7}\right)^{\frac{1}{2}} \left(\frac{\sigma}{f_c}\right) \left(\frac{10}{3} - 2\alpha\right)^{\frac{1}{2}} \right] \right\} \tag{5.18}$$

where σ (without bold type) is the residual strength at the given number of load cycles. It is argued in this present research work that the softening function presented by Wen (2011) seen in Eq. (5.15) is inadequate in predicting the fatigue behavior of concrete in biaxial stress space because it doesn’t shoe the effect the load path has on strength degradation of concrete. It is because of this that the softening function given in Eq. (5.16) is used in this paper to incorporate the effect the stress path has on strength softening.

Figure 5.3 demonstrates the effect of the softening function on the model for uniaxial compression. The ultimate compression strength of concrete is decreased to its residual strength for a given number of cyclic loads. It is important to note that for uniaxial compression both softening functions equate to the same residual strength. The correlation between the model and the experimental data obtained from Nelson et al. (1988) is good.

The varying effect the two softening functions have on the model is demonstrated in the S-N curves for multiaxial loading. It has been seen that in biaxial stress space concrete experiences larger strength degradation from fatigue loading than in uniaxial compression. With this in mind, the weakness of the softening function based solely as a function of cyclic loading is apparent. In Figures 5.4 and 5.5 the varying effect of the two forms of the softening function can be seen for biaxial loading. The function that is dependent on the load path is capable of capturing the increased strength degradation that occurs in biaxial compression.

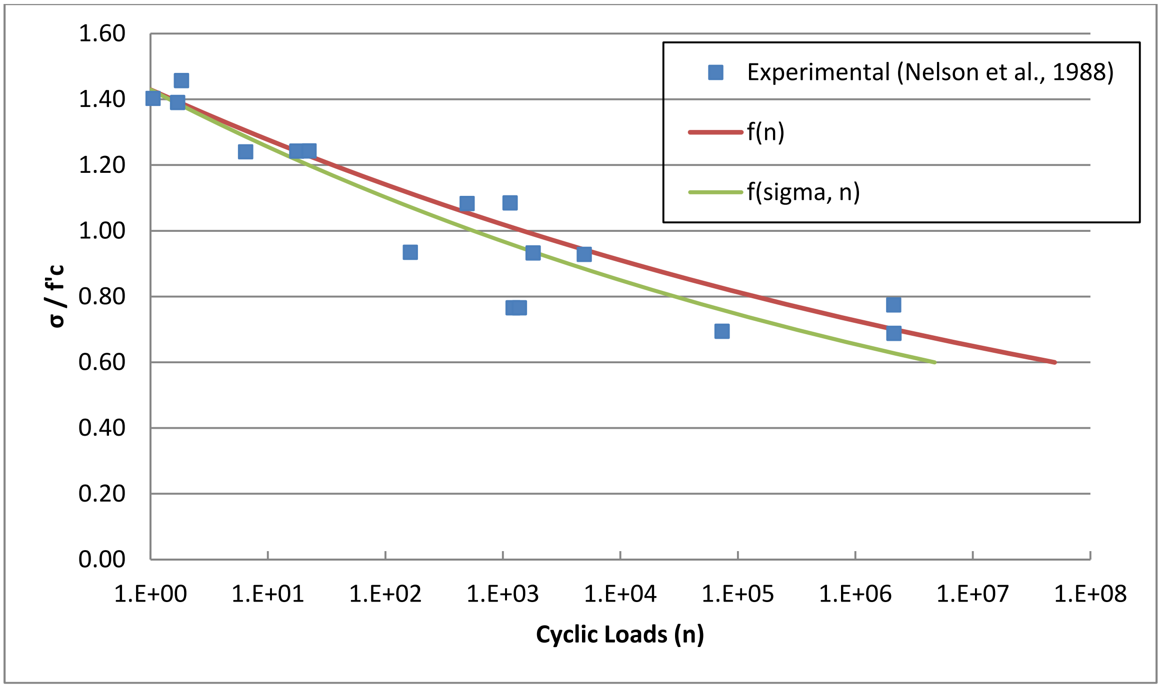

Fig. 5.4. Residual strength vs. number of cyclic loads for stress ratio 1:1

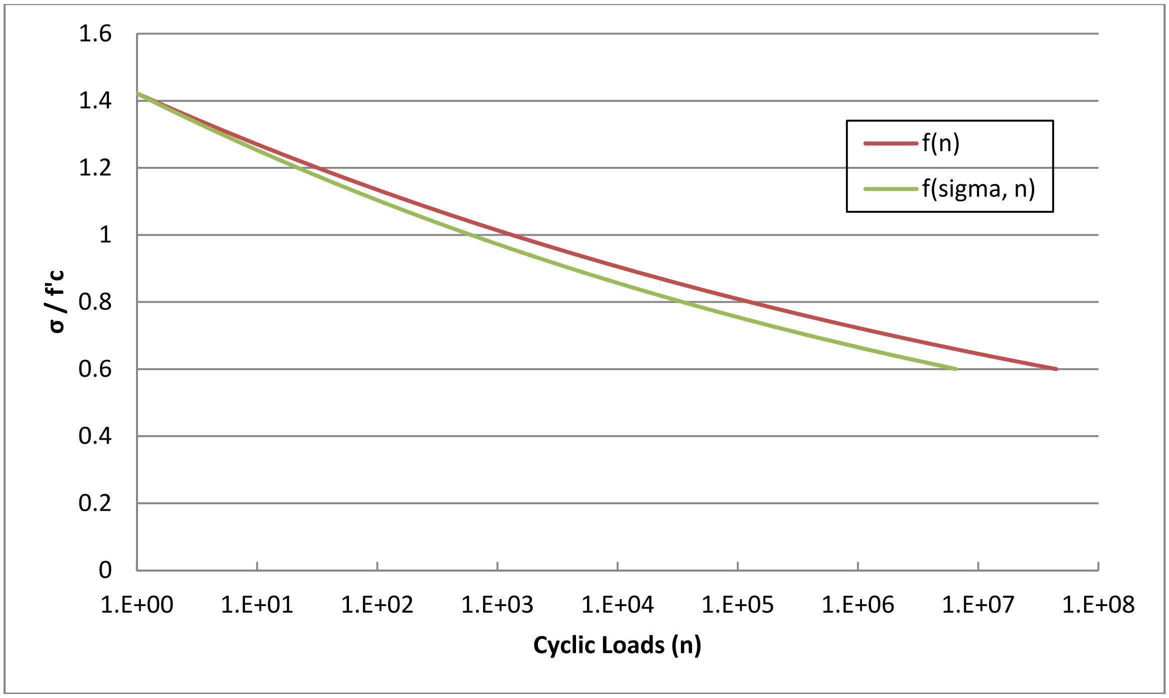

Fig. 5.5. Residual strength vs. number of cyclic loads for stress ratio 1:0.5

The effect of the softening function can be seen easier from the strength surface. This will be presented in the following section along with other numerical examples, including a sensitivity analysis which shows the effect of various model parameters have on the model output.

5.3. Numerical Example

In the previous section the capabilities of the model to predict the fatigue life of concrete were presented for two specific load cases. As seen in Chapter 3, the model is capable of producing a strength surface in 2-dimensional stress space for monotonic loading, and as discussed in Section 5.1.1, the bounding surface approach allows this model to produce residual strength surfaces corresponding to a given number of cyclic loads. This will be presented in detail in this section and compared with experimental data presented by Nelson et al. (1988) where uniaxial and biaxial compression fatigue loading was done on high strength concrete for various biaxial load ratios. The uniaxial compressive strength of the concrete used in their experimental program was 62.7 MPa (9100 psi). The Young's Modulus and Poisson's Ratio are 47.3 GPa (6860 ksi) and 0.31, respectively.

In biaxial compression the function describing the strength surface is similar to Eq. (5.12) given as the following:

$$\begin{aligned}\psi(\boldsymbol{\sigma}, k) = \frac{1}{2}\boldsymbol{\sigma}^{-}:\frac{\tilde{\boldsymbol{\sigma}} \otimes \tilde{\boldsymbol{\sigma}}}{\tilde{\boldsymbol{\sigma}}:\tilde{\boldsymbol{\sigma}}}:\boldsymbol{\sigma}^{-} + \frac{1}{2}\left(\alpha H\left(-\bar{\lambda}\right)\right)\boldsymbol{\sigma}:\boldsymbol{\sigma} - \frac{1}{2}\left(\alpha H\left(-\bar{\lambda}\right)\right) tr^{2}(\boldsymbol{\sigma}) \\ + (\boldsymbol{S}^{-} + \beta_2 \boldsymbol{S}^{+}):\boldsymbol{\sigma} - \frac{1}{2}\left(\frac{7}{3}\right) f_c^2 n^{\left[\left(\frac{tr^2(\boldsymbol{\sigma})}{\boldsymbol{\sigma}:\boldsymbol{\sigma}}\right)^{B} A\right]} = 0\end{aligned} \tag{5.19}$$

where f_c is the uniaxial compressive strength of concrete. Four material parameters are used in biaxial compression: α, β_2, A, and B. As discussed previously, the parameters can be obtained experimentally. α can be solved for from the strength surface for monotonic loading and for this example is the following:

$$\alpha = \frac{5}{3} - \frac{1}{2}\left[\frac{\left(\frac{7}{3}\right)^{0.5} f_c}{\sigma}\right] = 1.096 \tag{5.20}$$

β_2 is a material parameter related to permanent deformations and is taken to be 1.2 for this example. The fatigue parameters A and B can be obtained from Equations (5.17) and (5.18), respectively. For this example A is equal to -0.049 and B is equal to 0.207.

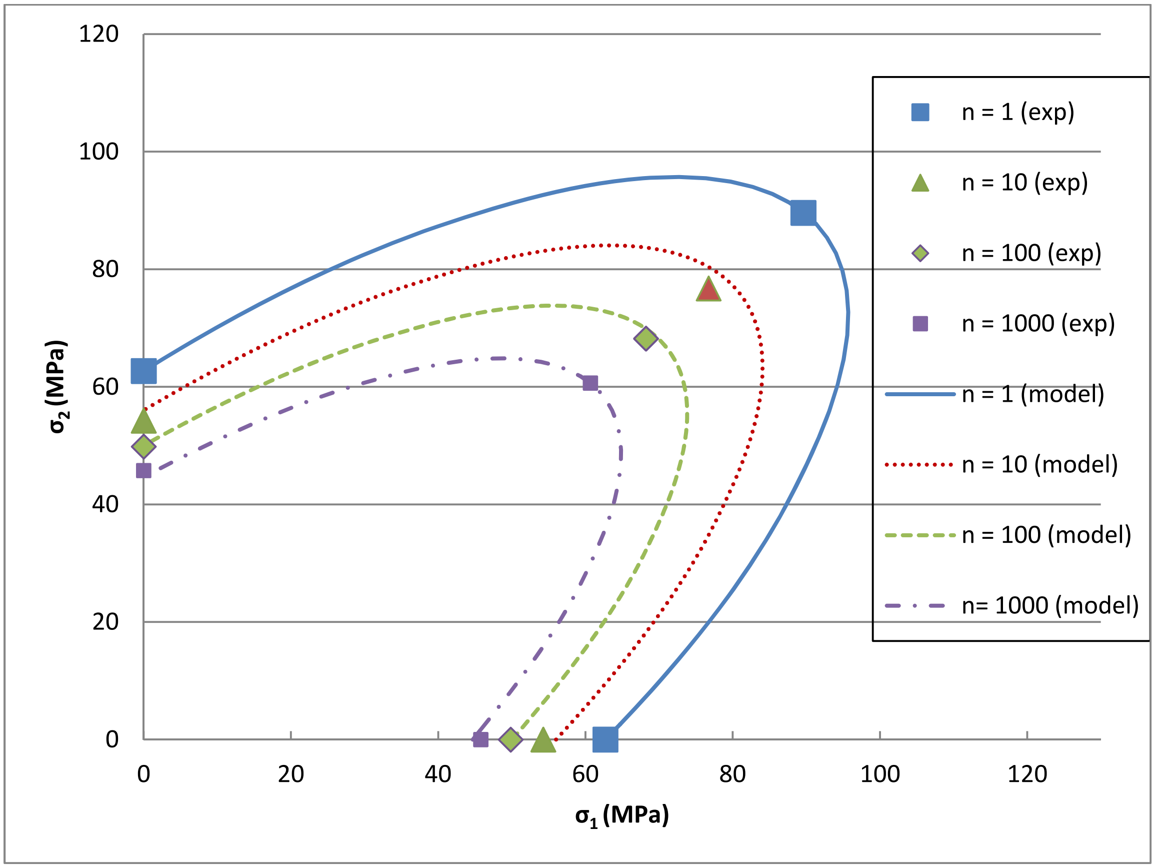

Fig. 5.6. Residual strength surfaces for varying number of cyclic loads in for biaxial compressive fatigue loading

Fatigue also has a dramatic effect on the deformation behavior of concrete. Figures 5.7 and 5.8 show the stress-strain behavior for uniaxial compression and equal-biaxial compression, respectively, in the presence of fatigue loading. In this example the permanent deformations are ignored for simplicity, but one can see the increased compliance occurring with an increasing number of cyclic loads.

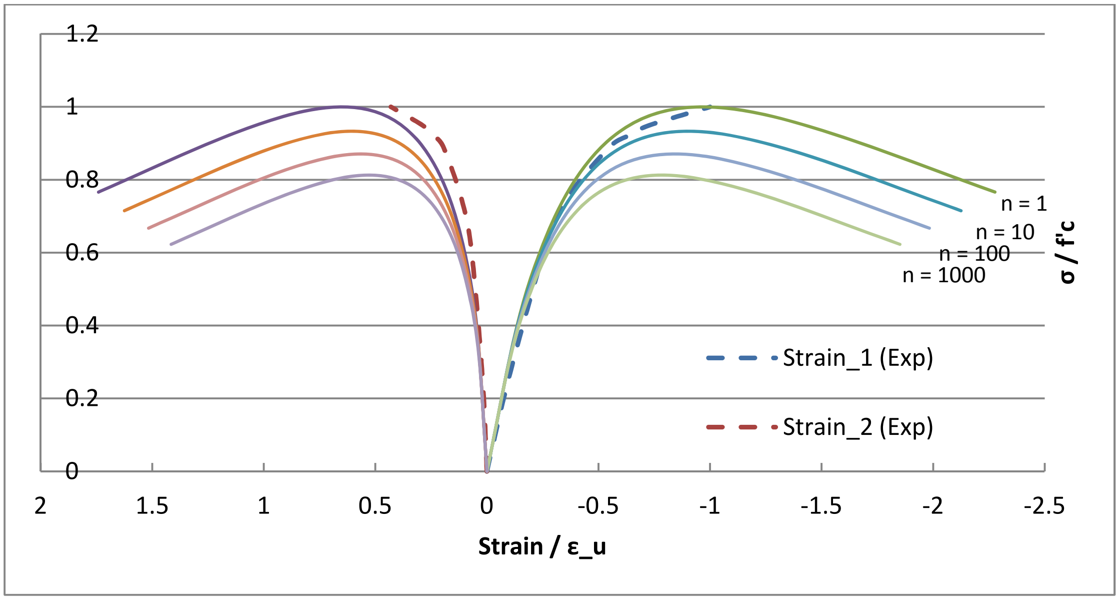

Fig. 5.7. Stress vs. strain for uniaxial compression for multiple number of cyclic loads (Experimental data by Litewka and Dubinski, 2003)

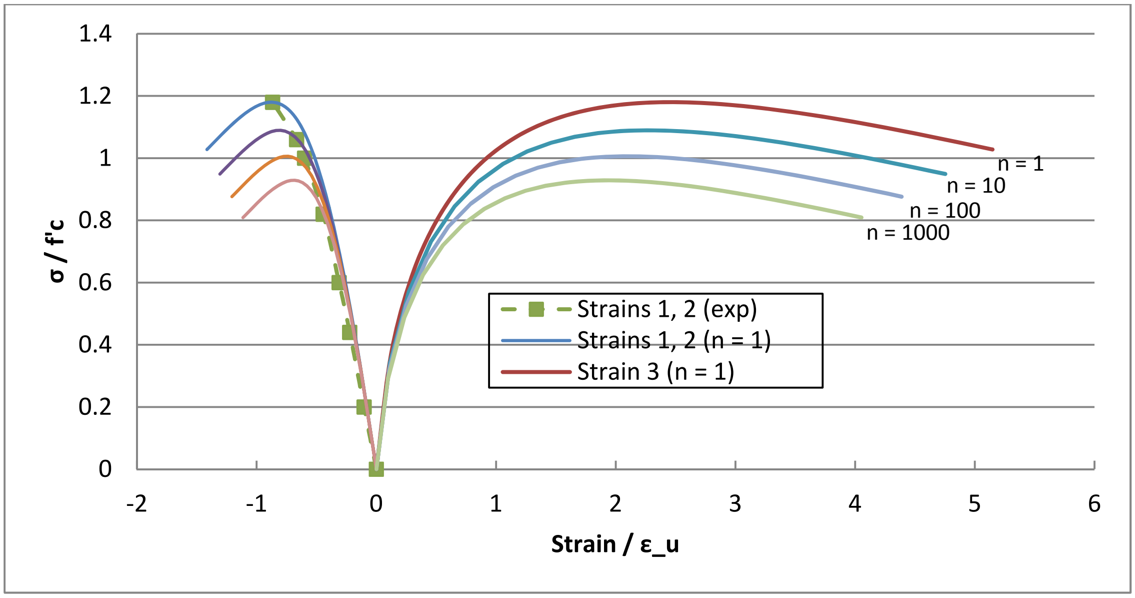

Fig. 5.8. Stress vs. strain for equal-biaxial compression for multiple number of cyclic loads (Experimental data by Litewka and Dubinski, 2003)

5.3.1. Sensitivity Analysis

The effects the model parameters α and β_2 have on the strength surface are shown in Figure 5.9 and are compared with experimental results.

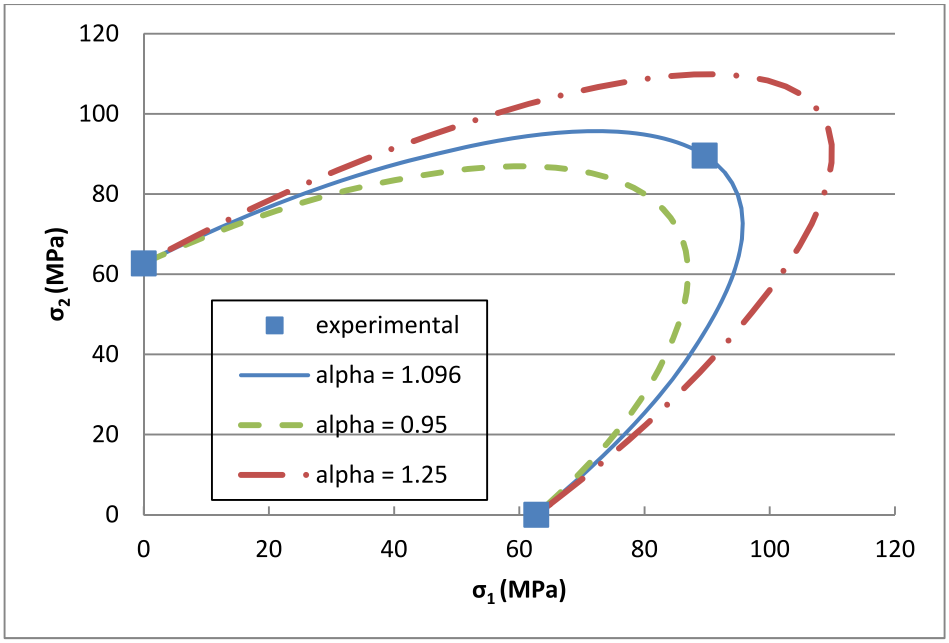

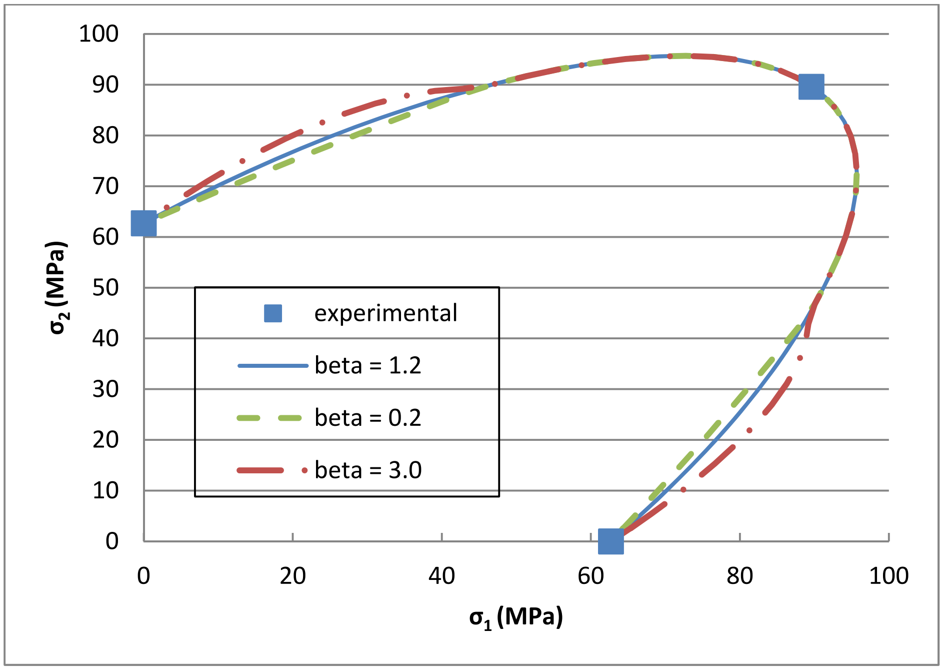

Fig. 5.9. Limit surface comparison for various values of α and β_2 parameters (Experimental data by Nelson et al., 1988)

The effects the model parameters *A* and *B* have on the S-N curves for various load ratios are shown in the following figures. Note that *B* has no effect for uniaxial loading.

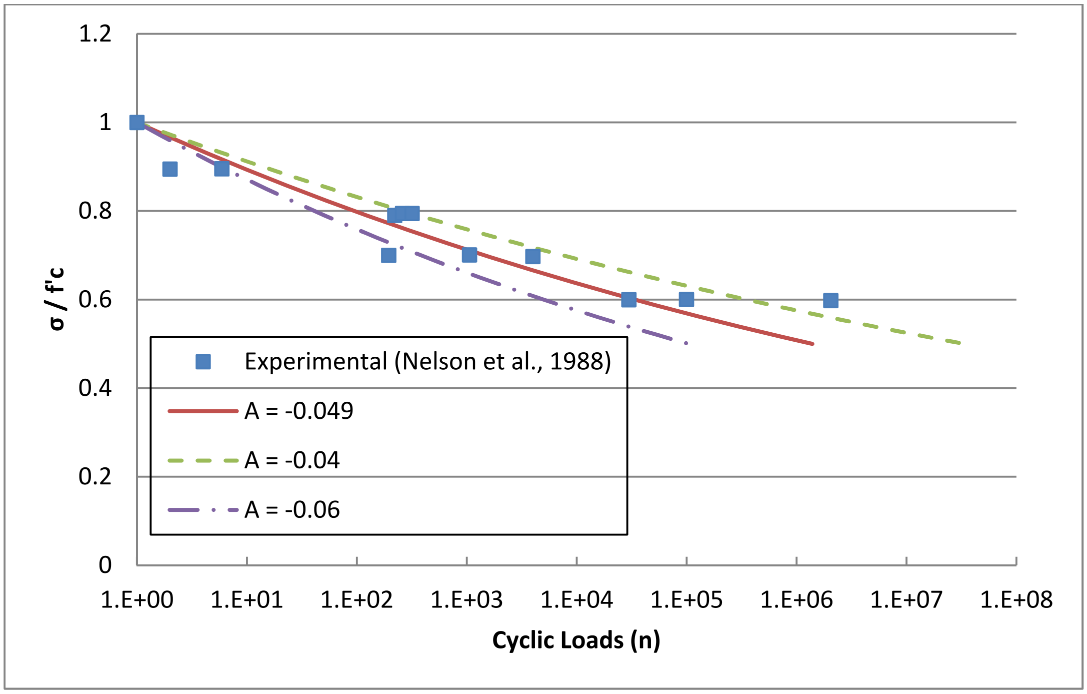

Fig. 5.10. S-N curve for stress ratio 1:0, varying parameter *A*

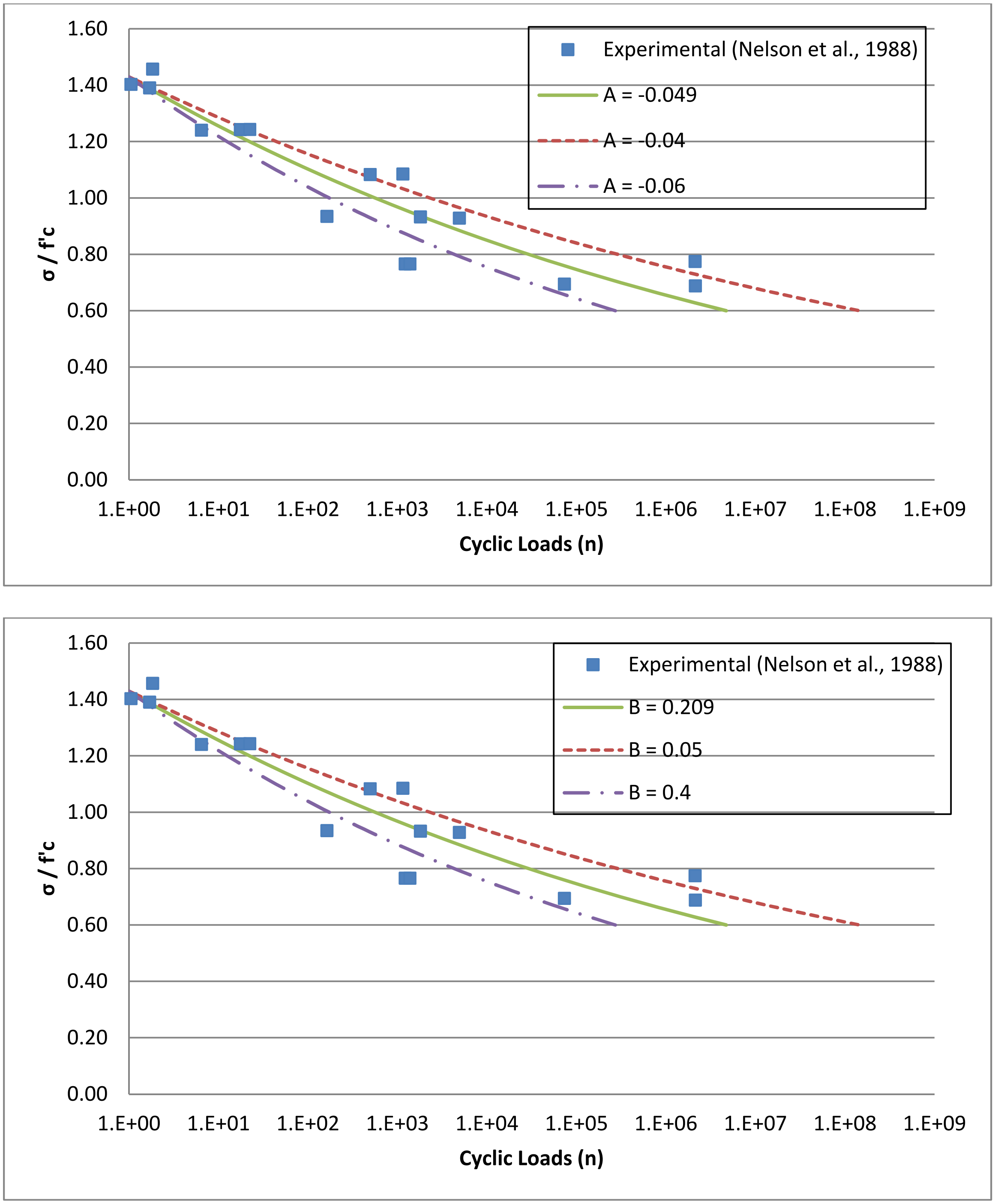

Fig. 5.11. S-N curve for stress ratio 1:1, varying parameter *A* and *B*

5.4. The Bounding Surface Approach Extended

Part of what makes the bounding surface approach so appealing is the versatility it has when it comes to its application. The bounding surface approach has the inherent ability to be applied to any limit surface. So far in this paper it has been applied to a limit surface that has been established using continuum damage mechanics theory. To demonstrate the versatility of the bounding surface approach, it will be applied to a completely different limit surface. With simplicity in mind, Schreyer's model (1983) based on the third-invariant plasticity theory for frictional materials will be used. A brief description of the model will be given.

This model's purpose is an attempt to capture the essential behavioral properties of concrete and other frictional materials using the theory of plasticity, while not resorting to a large number of model parameters. Because concrete is a frictional material the third invariant is used to capture its dependence on shear stress. The limit surface for brittle and quasi-brittle materials including concrete, are also dependent on the first invariant of stress, also known as pressure. In Schreyer's model (1983) the following invariants are used together to for a limit surface:

$$P = -\frac{1}{3} tr(\boldsymbol{\sigma}) \tag{5.21}$$

$$L = -[\det(\boldsymbol{\sigma} - \boldsymbol{\sigma_s}) + \det(\boldsymbol{\sigma_s})]^{\frac{1}{3}} \tag{5.22}$$

where P and L are the mean pressure (first invariant) and third invariant, respectively. σ_s is defined as the shift stress and is the strength of concrete for purely shear loading. The shift stress can be obtained experimentally. If the principle stresses are considered and if $\boldsymbol{\sigma_s} = \sigma_s I$, the first and third stress invariants become the following:

$$P = -\frac{1}{3}(\sigma_1 + \sigma_2 + \sigma_3) \tag{5.23}$$

$$L = -[(\sigma_1 - \sigma_s)(\sigma_2 - \sigma_s)(\sigma_3 - \sigma_s) + \sigma_s^3]^{\frac{1}{3}} \tag{5.24}$$

It is then convenient to define the limit surface as a line related to the first invariant, third invariant, and the shift stress.

$$L = \gamma_L P - \sigma_s \tag{5.25}$$

γ_L is the limit slope and is a function of the uniaxial strength of the material and shift stress. From the experimental data shown one can see that the equation for the limit surface in L-P space represents the behavior of concrete quite well. This can be seen in Figure 5.12.

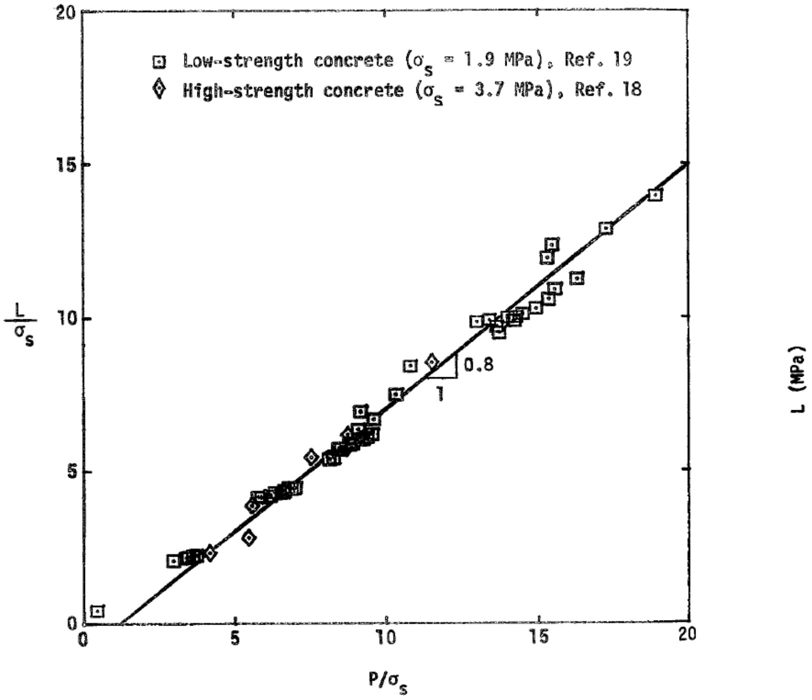

Fig. 5.12. Limit surface for low and high-strength concrete (Schreyer, 1983; Green and Swanson, 1973; Traina, 1983)

In addition, the ability of this model to represent concrete behavior for biaxial compression is shown in principle stress space. The principle stresses can be solved for in biaxial compression by some algebraic manipulation.

$$\sigma = \begin{bmatrix} \sigma_1 \\ \gamma\sigma_1 \\ 0 \end{bmatrix} \tag{5.26}$$

$$\begin{gathered}\sigma_1^3 + \left[-\left(\frac{\gamma_L(1+\gamma)}{3}\right)^{-3}\left(-3\left(\frac{\gamma_L(1+\gamma)}{3}\right)^2\sigma_s - \gamma\sigma_s\right)\right]\sigma_1^2 + \\ \left[-\left(\frac{\gamma_L(1+\gamma)}{3}\right)^{-3}\left(-3\left(\frac{\gamma_L(1+\gamma)}{3}\right)^2\sigma_s^2 + \sigma_s^2 + \gamma\sigma_s^2\right)\right]\sigma_1 - \sigma_s^3\left[-\left(\frac{\gamma_L(1+\gamma)}{3}\right)^{-3}\right] = 0\end{gathered} \tag{5.27}$$

where γ is ratio of stress in the principle directions 1 and 2. For this numerical example the values used for the shift stress, σ_s, and limit slope, γ_L, are 15.27 MPa and 0.74, respectively. The model's comparison with monotonic biaxial compression loading can be seen in Figure 5.13 below. One can see that because there are only two model parameters the biaxial behavior of concrete for the model and experimental data is not well matched. This is apparent for biaxial load ratios between 0 (uniaxial loading) and 1 (equal-biaxial loading).

Applying the bounding surface approach to this model, the same softening function is used as in the previous section (see Equation 5.16). The same softening equation is used because the equation itself is not dependant on the model being use, but rather it is dependent on the type of behavior being modeled (in this case fatigue loading behavior). Similar to the previous section, the softening function is applied to the variable associated with the strength of the material; the shift stress in this case. The limit surface then becomes the following:

$$L = \gamma_L P - \sigma_s * f(n, \boldsymbol{\sigma}) \tag{5.28}$$

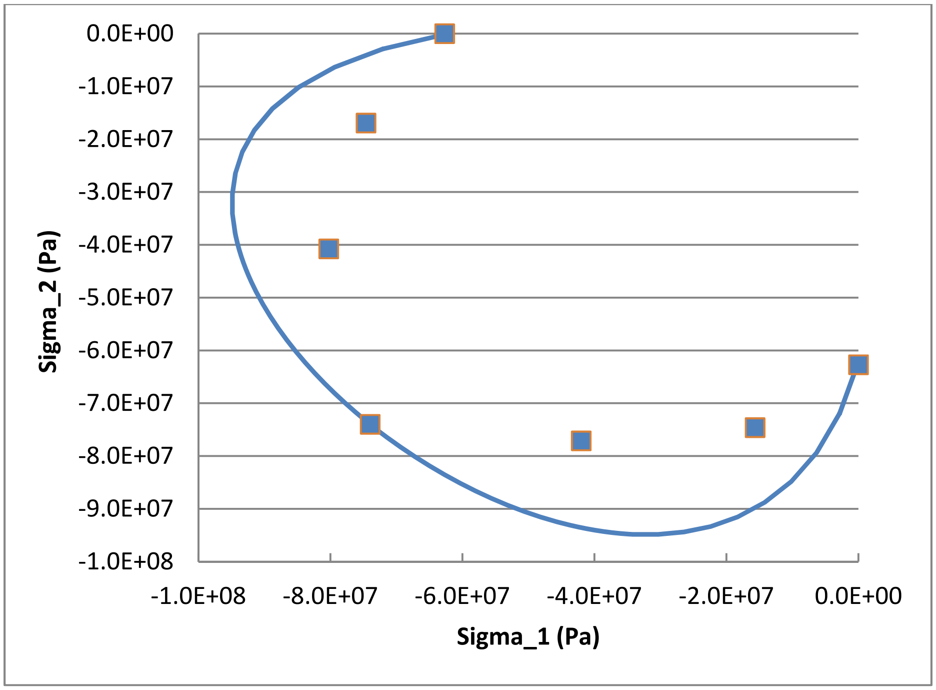

Fig. 5.13. Limit surface for high-strength concrete for biaxial compression, monotonic loading (Experimental data: Kupfer et al., 1969)

To look at the ability of the Schreyer model (1983), in combination with the bounding surface approach, to model the fatigue behavior of concrete it will be compared to experimental data presented by Nelson et al. (1988). Because this is a new set of experimental data new model parameters are needed. For this numerical example the following parameters are used:

$$\sigma_s = 13.18\ MPa, \qquad \gamma_L = 0.63, \qquad A = -0.049, \qquad B = 2.356$$

A common theme is that the model does not match the experimental data well across the entire biaxial compression stress regime. On the other hand, one can see the capabilities of the softening function to capture the fatigue life of the concrete for various load paths. An obvious outcome is that the better the model matches the experimental data for monotonic loading, the better it will match fatigue data using the bounding surface approach.

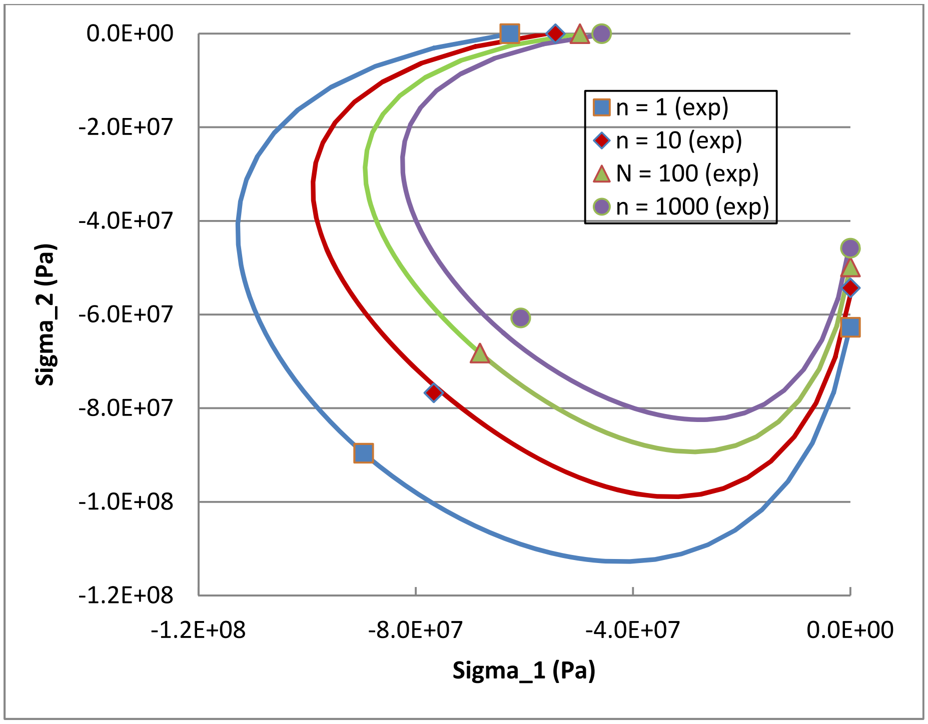

Fig. 5.14. Limit surface for high-strength concrete for biaxial compression, fatigue loading (Experimental data: Nelson et al., 1988)

5.5. Conclusion

In this chapter the monotonic concrete model was extended to include fatigue loading with good correlation to the available experimental results. Of significance discussed in this research is the need for more comprehensive multiaxial test data for the fatigue failure in concrete and concrete-like materials. Part of the difficulty is understandably the complexity of the testing apparatus in performing such experimental studies. Nonetheless, such data is deemed necessary for reliable analysis of concrete design, as in many applications of concrete design such as bridge decks and pavements, the material is subjected to a variety of multiaxial load paths. The bounding surface theory discussed by Wen (2011) was extended in this section and applied to the monotonic model for plain concrete. The softening function presented by Wen (2011) was shown to be less adequate in predicting the softening behavior of concrete for various load paths. A new softening function was therefore presented which incorporates the effect the load paths on strength and stiffness degradation for biaxial loading. The model prediction is compared to the experimental results of Nelson et al. (1988) and Litewka and Dubinski (2003) with good correlation. A sensitivity analysis is performed on the model to show the effect the various model parameters have on the model output.

In addition to the extension of the Yazdani model, the versatility of the bounding surface approach is highlighted by the extension of another concrete model created primarily for monotonic loading. By using the same softening function, which works well for fatigue compressive loading, any limit surface can be extended to predict the fatigue behavior of a material.

CHAPTER 6. MODELING OF CONCRETE FOR FREEZE-THAW PROCESSES USING THE BOUNDING SURFACE APPROACH

6.1. Introduction

Freeze-thaw processes are prominent in many concrete structures, and in particular, hydraulic structures in cold weather regions. Because freeze-thaw processes have such a damaging effect on concrete it is important that some amount of accountability for this damage be taken by engineers. Similar to the measure and prediction of the fatigue life of a material, it is logical for engineers to desire the residual strength of concrete for a given amount of freeze-thaw processes the concrete has withstood.

In this chapter the bounding surface approach is applied to a continuum damage mechanics model in a similar fashion to the previous chapter. It is shown in this chapter that using the bounding surface approach the model is capable of producing residual strength curves for a given number of freeze-thaw processes and a given load path (similar to S-N curves for fatigue processes). In addition, a limit or strength surface for the undamaged material along with residual strength surfaces for the corresponding number of freeze-thaw processes can systematically be developed. Finally, stress-strain behavior for a given load path and freeze-thaw processes are obtained.

In its current state this model is in some danger of oversimplification when concerned with freeze-thaw damage in concrete. The extent of damage occurring within the material is a function of many things including the characteristics of the material itself, freeze duration, and the degree of saturation. In its current state the model parameters are capable of accounting for the material characteristics, while the duration of the freeze is assumed to be relatively short (a few hours) and the concrete is assumed to be completely saturated. It is known that for concrete, longer duration of freeze will result in increased damage in the material, while a lesser degree of saturation will result in decreased damage in the material.

The aforementioned simplifications to the model can be addressed in the future if and only if there is sufficient experimental data to support said effects. Currently there is a lack of experimental data pertaining to the effect the duration of freeze has on the mechanical characteristics of concrete as well as the effect the degree of saturation has on concrete. Though the state of the model presented in this chapter is a good starting point, these are important factors in the performance of concrete in a freeze-thaw environment and need to be addressed in the future.

As stated earlier, in this chapter the bounding surface approach is used to incorporate the effect freeze-thaw processes have on the performance of concrete. The reader should reference Section 5.1.1 for an introduction to the bounding surface approach.

6.2. Formulation of Model with the Bounding Surface Approach

Several assumptions are made in the development of the model for freeze-thaw processes. As in previous chapters a continuum approach is used and it is assumed that a neighboring equilibrium state exists for all irreversible processes concerned in this paper. Furthermore, the freeze-thaw processes are assumed to occur over a short period of only several hours and the concrete specimen is assumed to be completely saturated upon freezing. Another significant assumption that is made in this approach is that in the temperature ranges considered, the temperature and the gradient of the temperatures do not contribute to the development of damage in concrete. In other words, the range of temperatures considered for short duration freeze-thaw cycles are not significantly high or low to induce damage. Therefore, the damage inflicted on the material is due to the freeze-thaw cycles and not due to the temperature.

Using the general formulation and in the previous chapter the following form of the damage surface is given:

$$\begin{aligned}\psi(\boldsymbol{\sigma},k) = \tfrac{1}{2}(1+\beta_1)\boldsymbol{\sigma}^{+}:\boldsymbol{\sigma}^{+} + \tfrac{1}{2}\boldsymbol{\sigma}^{-}:\tfrac{\tilde{\boldsymbol{\sigma}}\otimes\tilde{\boldsymbol{\sigma}}}{\tilde{\boldsymbol{\sigma}}:\tilde{\boldsymbol{\sigma}}}:\boldsymbol{\sigma}^{-} + \tfrac{1}{2}\left(\gamma H(\lambda_1\,) + \alpha H\left(-\bar{\lambda}\right)\right)\boldsymbol{\sigma}:\boldsymbol{\sigma} - \\ \tfrac{1}{2}\left(\gamma H(\lambda_1) + \alpha H\left(-\bar{\lambda}\right)\right) tr^2\,(\boldsymbol{\sigma}) + (\boldsymbol{S}^{-} + \beta_2\boldsymbol{S}^{+}\,):\boldsymbol{\sigma} - \tfrac{1}{2}t^2\,(k) = 0\end{aligned} \tag{6.1}$$

It should be emphasized that although the general form of the damage surface is similar to the previous chapter, the damage and the resulting softening function will be different for the freeze-thaw processes being modeled. In particular, the specifics of the parameters and the forms of the function used will depend on the experimental observations for freeze-thaw cycles. The softening function, which is part of the damage function, needs to be of a form which accurately represents the strength softening which occurs with freeze-thaw processes.

6.2.1. Softening Function

It can be seen in Chapter 2 that concrete subjected to freeze-thaw processes experiences a reduction in strength. Experimental data presented by Shang et al. (2006, 2009) shows that concrete strength and the number of freeze-thaw cycles being experienced, have a nearly linear relationship for a given load path. Similar to the softening behavior of concrete for fatigue processes, concrete's strength degradation is dependent on the load path in. It is apparent from Figure 6.2 that the strength of concrete decreases at a higher rate for uniaxial compression than

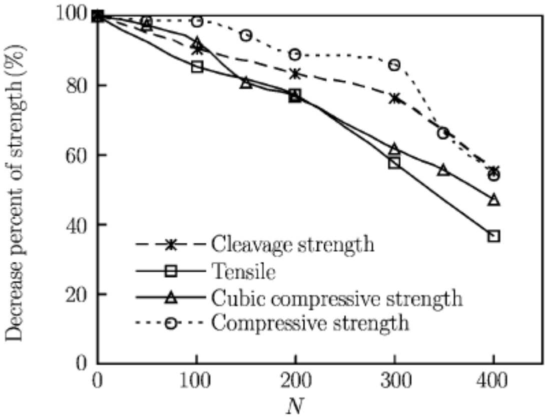

Fig. 6.1. Strength vs. number of freeze-thaw cycles for uniaxial tension and compressive loading of air-entrained concrete (Shang et al., 2009)

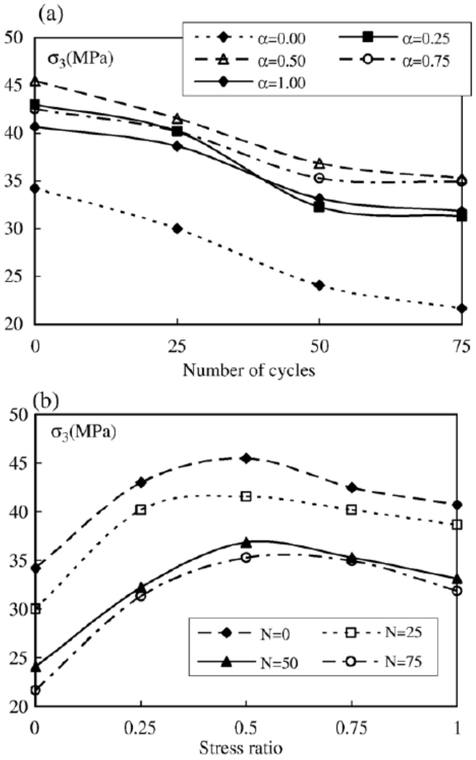

Fig. 6.2. Strength vs. number of freeze-thaw cycles for biaxial compression (top) and strength vs. stress ratio (bottom) (Shang et al., 2006)

for biaxial compression. For this reason, a softening function is proposed in this section that provides a linear softening relationship that is also a function of the load path.

Utilizing a similar argument as in Wen (2011) a softening function *f(n)* can be defined that effectively reduces the strength of concrete as the number of freeze-thaw cycles increases. As the softening function affects the strength properties of the material, it is logical to incorporate it into the strength function, *t*. For uniaxial compression and at the limit state the following is obtained from Eq. (6.1):

$$t^2(\boldsymbol{\sigma}, k) = \frac{7}{3} f_c^2 f^2(n) \tag{6.2}$$

which can be shown to result in our expression for the softening function as

$$f(n) = \frac{\sigma}{f_c} \tag{6.3}$$

where σ (without bold type) is the residual strength of the concrete for a given number of freeze-thaw cycles. Eq. (6.3) shows that the softening function can be considered as the ratio of the residual strength after *n* freeze-thaw cycles and the ultimate compressive strength under monotonic loading. As previously stated, from experimental data it is concluded that the strength of concrete has a linear relationship with the number of freeze-thaw cycles (Figure 6.1 and 6.2).

Guided by the experimental results, a softening function is proposed below in the form of a linear function of the number of freeze-thaw cycles and the load path:

$$f(\boldsymbol{\sigma}, n) = 1 - B\left[\frac{\boldsymbol{\sigma}:\boldsymbol{\sigma}}{tr^2(\boldsymbol{\sigma})}\right]^C n \tag{6.4}$$

where *B* and *C* are material parameters that can be obtained by solving for them from the damage surface, Eq. (6.1), under uniaxial compression and equal-biaxial compression, respectively. Solving for parameters *B* and *C* the following is obtained:

$$B = \left(1 - \frac{\sigma}{f_c}\right) n^{-1} \tag{6.5}$$

$$C = \ln\left\{\left[1 - \frac{\sigma\left(\frac{10}{3} - 2\alpha\right)^{\frac{1}{2}}}{\left(\frac{7}{3}\right)^{\frac{1}{2}} f_c}\right](Bn)^{-1}\right\}\left(\ln\left(\frac{1}{2}\right)\right)^{-1} \tag{6.6}$$

where σ (without bold type) is the residual strength at the given number of freeze-thaw cycles.

Figures 6.3, 6.4, 6.5, and 6.6 demonstrate the effect of the softening function on the model for various load paths in compression. The ultimate compression strength of concrete is decreased to its residual strength for a given number of freeze-thaw cycles. The correlation between the model and the experimental data obtained from Shang et al. (2006, 2008) is good.

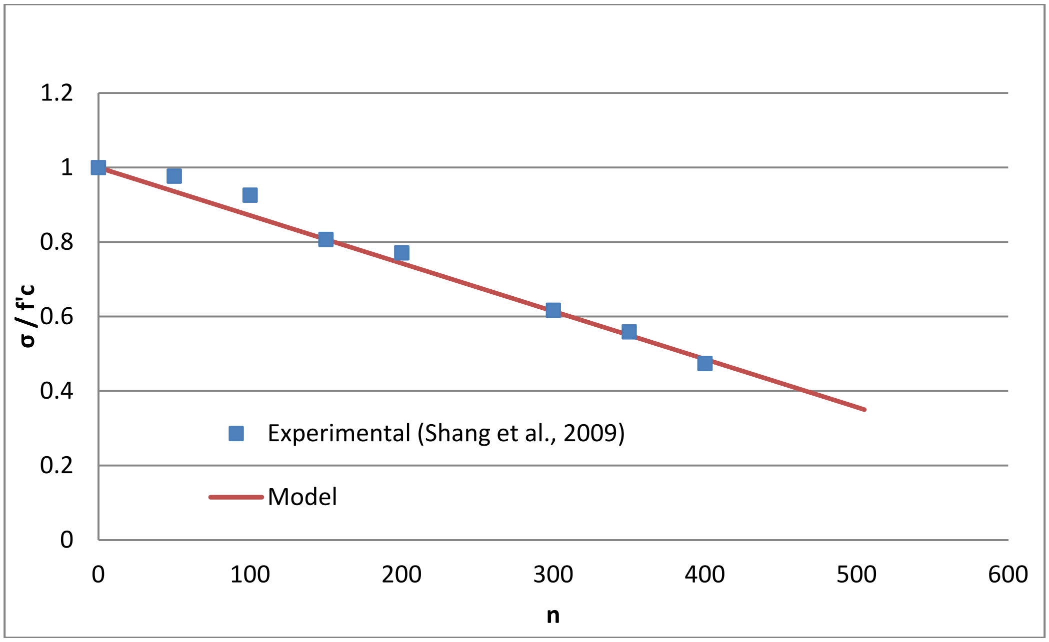

Fig. 6.3. Residual strength vs. number of freeze-thaw cycles for stress ratio 1:0 (uniaxial compression)

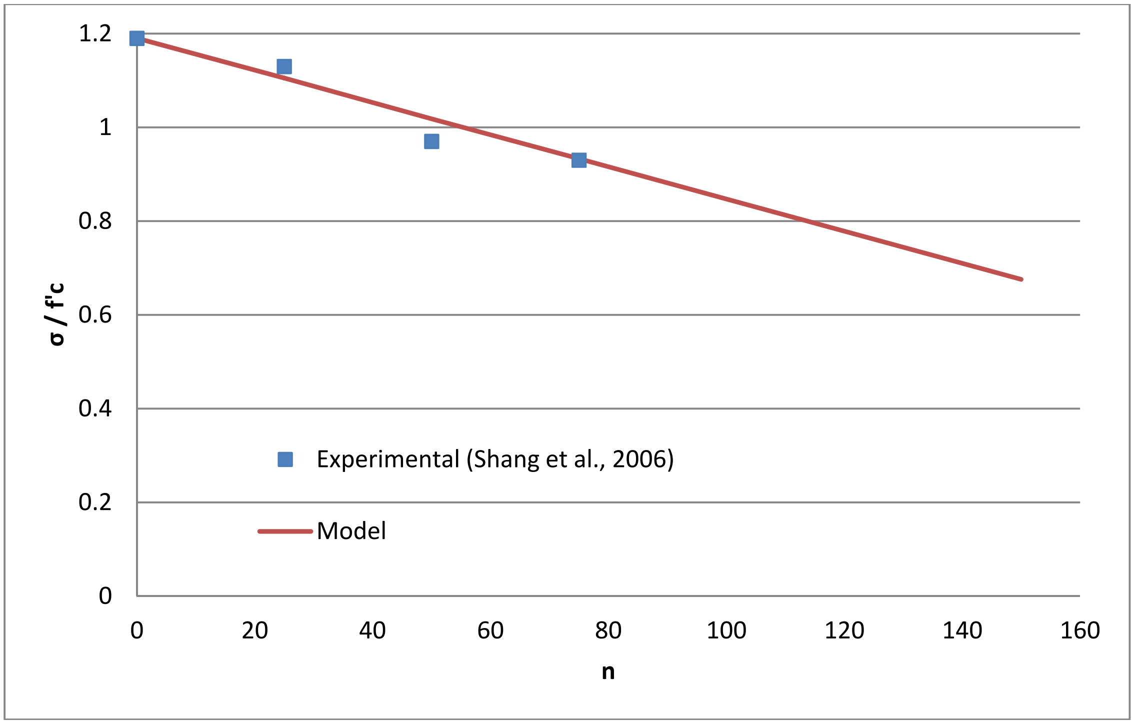

Fig. 6.4. Residual strength vs. number of freeze-thaw cycles for stress ratio 1:1 (equal-biaxial compression)

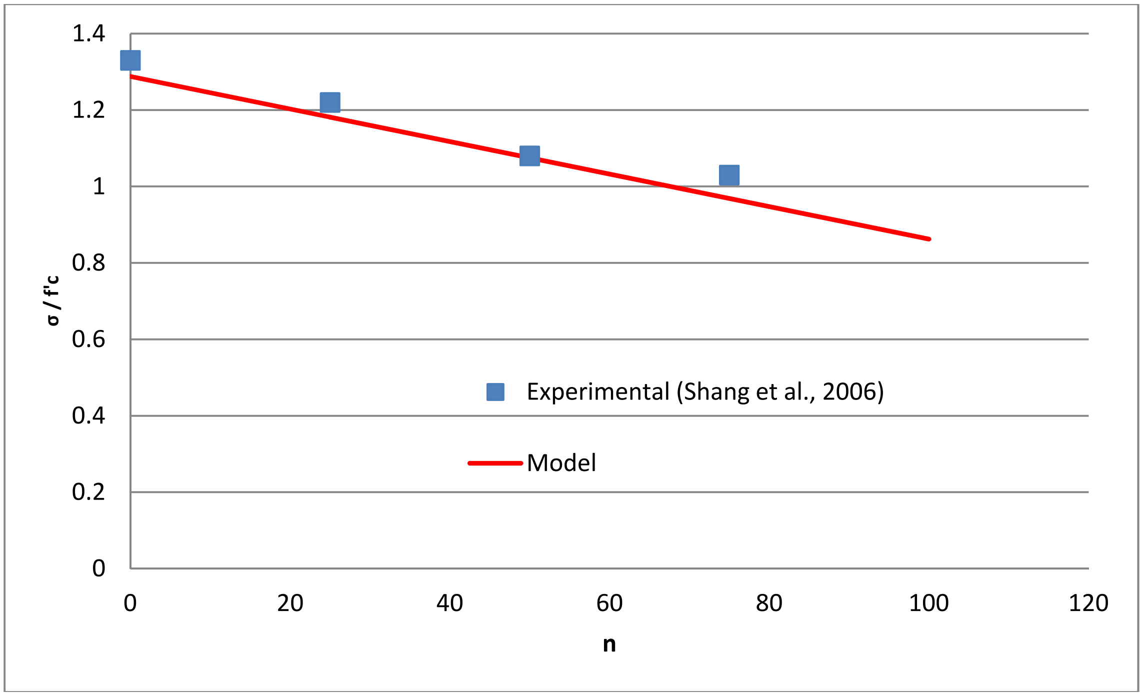

Fig. 6.5. Residual strength vs. number of freeze-thaw cycles for stress ratio 1:0.5 (biaxial compression)

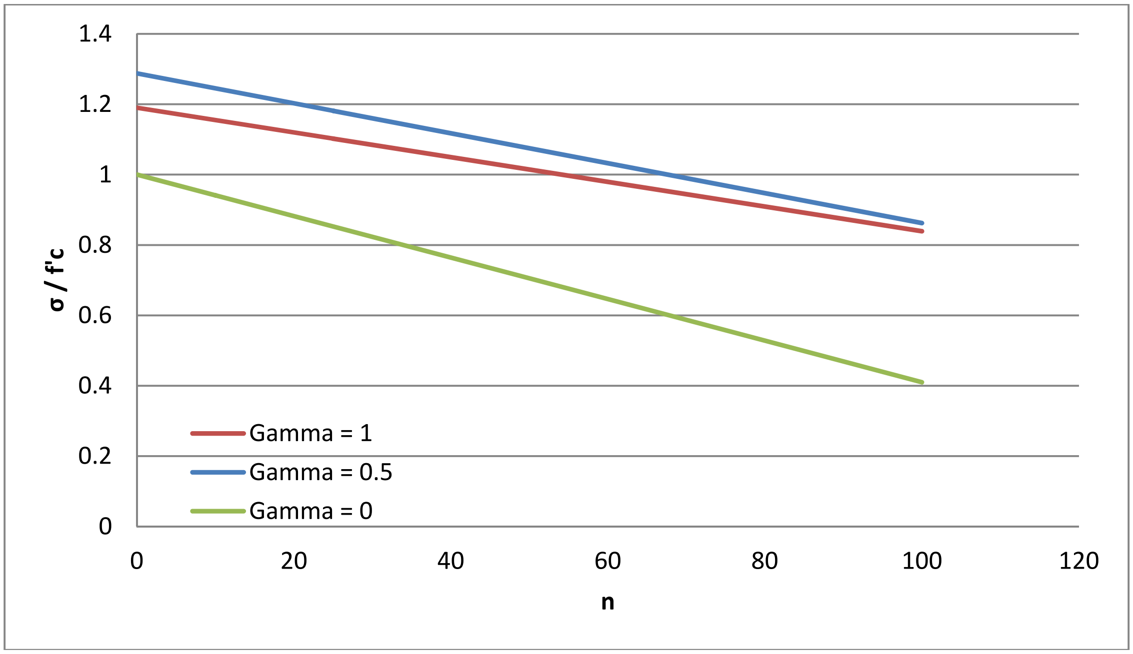

Fig. 6.6. Residual strength vs. number of freeze-thaw cycles for various load paths in compression

6.3. Numerical Example

The Yazdani model (1993), which was presented in detail in Chapter 3 is expanded in this chapter to include the effect freeze-thaw damage has on concrete using the bounding surface theory. Similar to the previous chapter where fatigue processes are modeled, for a given number of freeze-thaw cycles a residual strength surface is produced which describes the reduced strength which develops within the concrete for various load paths in 2-dimensional space. In Section 6.2 the capabilities of the model with respect to freeze-thaw processes is demonstrated in detail for various load paths and number of freeze-thaw cycles. Model parameters are obtained from experimental data presented by Shang et al. (2006, 2009) for uniaxial and biaxial loading and the model output is verified using the experimental results. The compressive strength and Young's modulus of the concrete used in the Shang et al. (2006, 2009) experimental program are

34.2 MPa (5000 psi) and 26.8 GPa (3886 ksi), respectively. The Poisson's ratio used is assumed to be 0.3.

The residual strength surface for in biaxial compressive stress space is shown in Figure 6.6 for 0, 25, 50, and 75 freeze-thaw cycles. A residual strength surface can be obtained from Equation 6.1 and is given below.

$$\begin{gathered}\psi(\boldsymbol{\sigma},k)=\frac{1}{2}\boldsymbol{\sigma}^{-}:\frac{\tilde{\boldsymbol{\sigma}}\otimes\tilde{\boldsymbol{\sigma}}}{\tilde{\boldsymbol{\sigma}}:\tilde{\boldsymbol{\sigma}}}:\boldsymbol{\sigma}^{-}+\frac{1}{2}\left(\alpha H\left(-\bar{\lambda}\right)\right)\boldsymbol{\sigma}:\boldsymbol{\sigma}-\frac{1}{2}\left(\alpha H\left(-\bar{\lambda}\right)\right)tr^{2}(\boldsymbol{\sigma})\\ +\left(\boldsymbol{S}_{2}^{\mp\beta}\boldsymbol{S}^{+}\right):\boldsymbol{\sigma}-\frac{1}{2}\left(\frac{7}{3}\right)f_c^2(1-B\left[\frac{\sigma:\sigma}{tr^{2}(\sigma)}\right]^{C}n)=0\end{gathered}\tag{6.7}$$

where f_c is the uniaxial compressive strength of concrete. Four material parameters are used in biaxial compression: α, β_2, B, and C. The parameters can be obtained experimentally. α can be solved for from the strength surface for monotonic equal-biaxial compressive loading and for this example is the following:

$$\alpha=\frac{5}{3}-\frac{1}{2}\left[\frac{\left(\frac{7}{3}\right)^{0.5}f_c}{\sigma}\right]=0.843\tag{6.8}$$

β_2 is a material parameter related to permanent deformations and is taken to be 1.2 for this example. The fatigue parameters B and C can be obtained from Equations (6.5) and (6.6), respectively. For this example B is equal to 0.0059 and C is equal to 1.025.

Figure 6.7 shows the effectiveness of the model in creating residual strength surfaces for various number of freeze-thaw cycles in biaxial compression space. The softening function, which is a function of both the number of freeze-thaw cycles and the load path, does a good job of recreating realistic strength loss in concrete for different load paths. This is apparent when the experimental data of Shang et al. (2006) is compared with the model results.

The deformation of concrete is also affected by damage caused by freeze-thaw processes. In the following numerical examples the stress-strain curves for various load paths are shown for concrete prior to freeze-thaw damage and after 25, 50, and 75 freeze-thaw cycles. This is shown in Figure 6.8. One can see that the increased plasticity seen in the experimental data is not adequately captured by the model. While the model shows increased compliance with increasing freeze-thaw cycles, the experimental data shows larger ultimate strains as the number of freeze-thaw cycles increases.

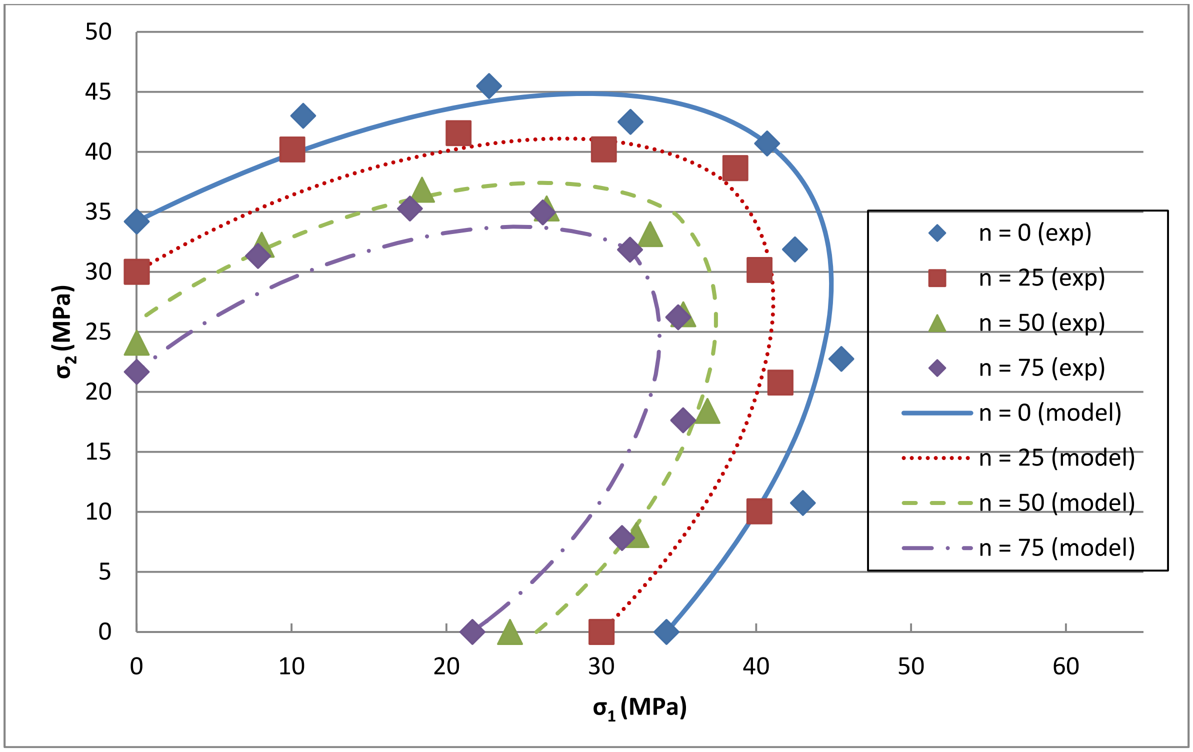

Fig. 6.7. Residual strength surfaces for various number of freeze-thaw cycles in biaxial compression

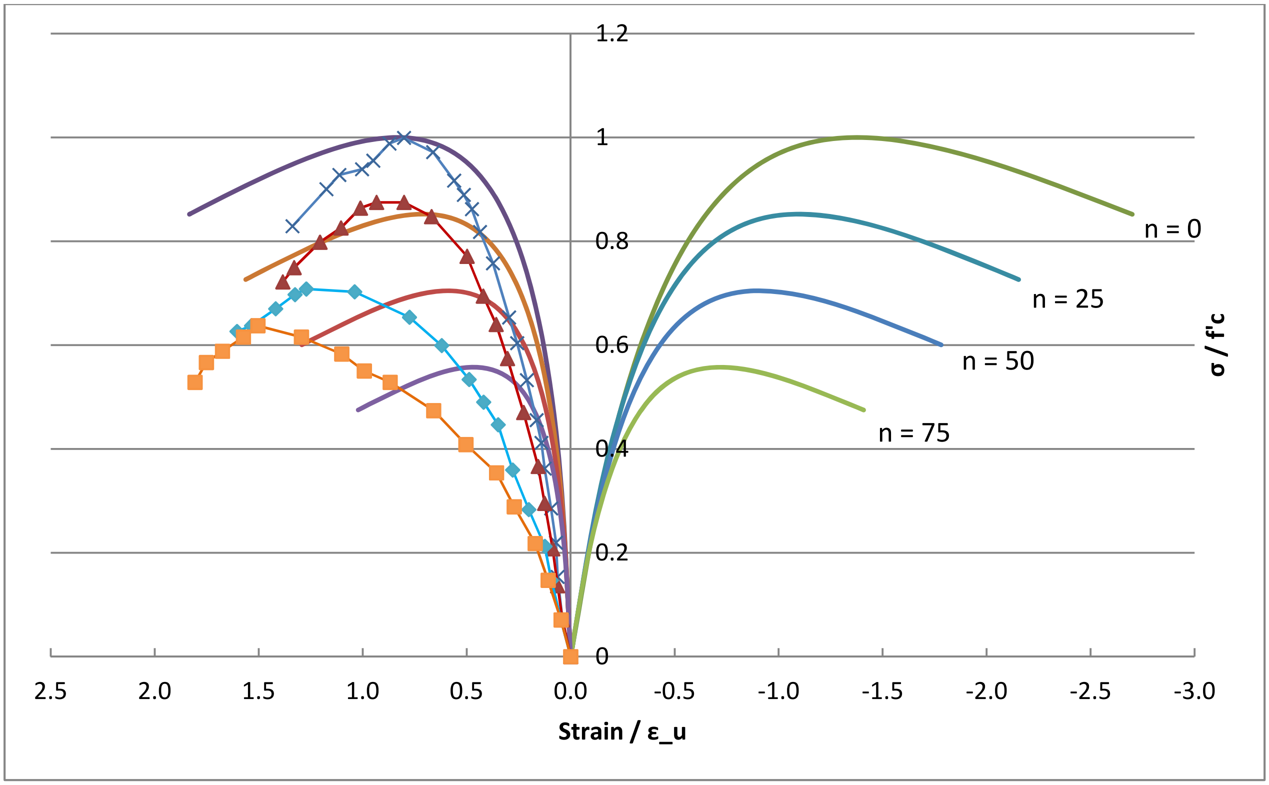

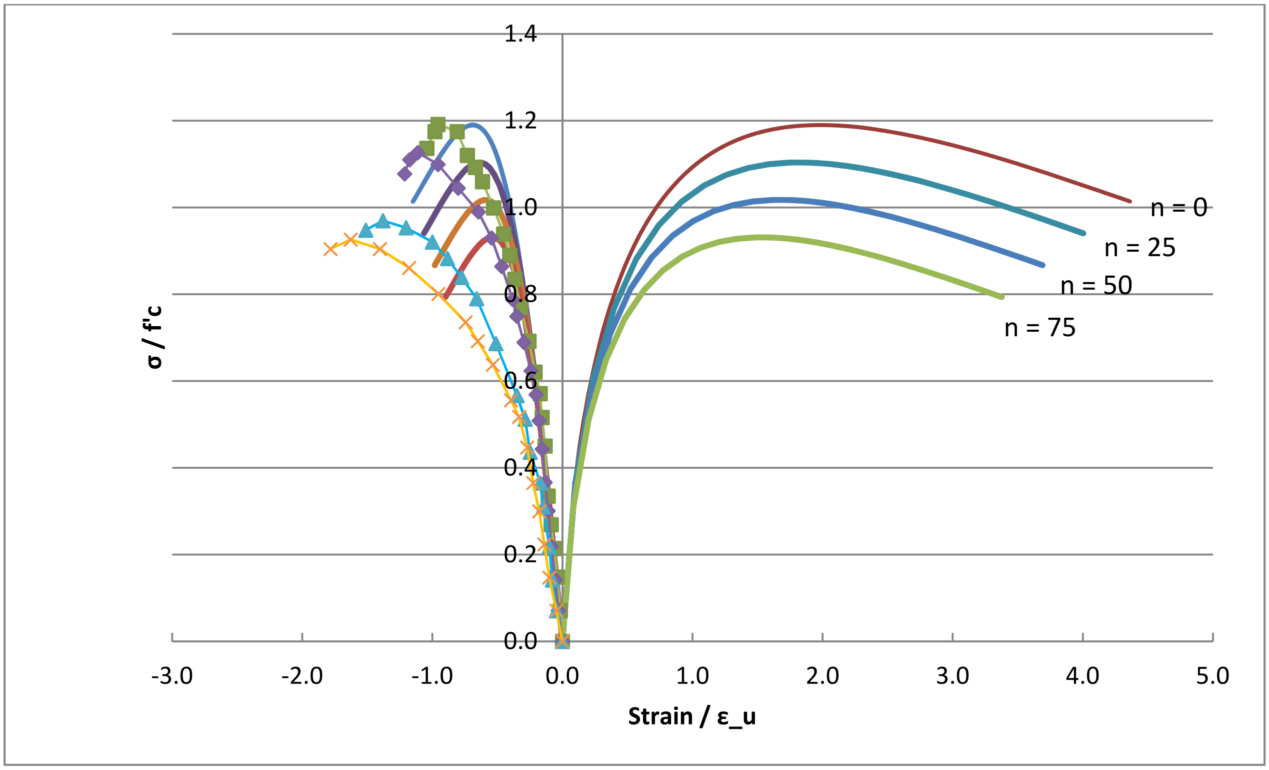

Fig. 6.8. Stress vs. strain for uniaxial (top) and equal-biaxial (bottom) compression, model output (line) and experimental data (marker and line) (Shang et al., 2006)

6.3.1. Sensitivity Analysis

As shown in Chapter 5, the effect of various parameters on the model is shown in the following section.

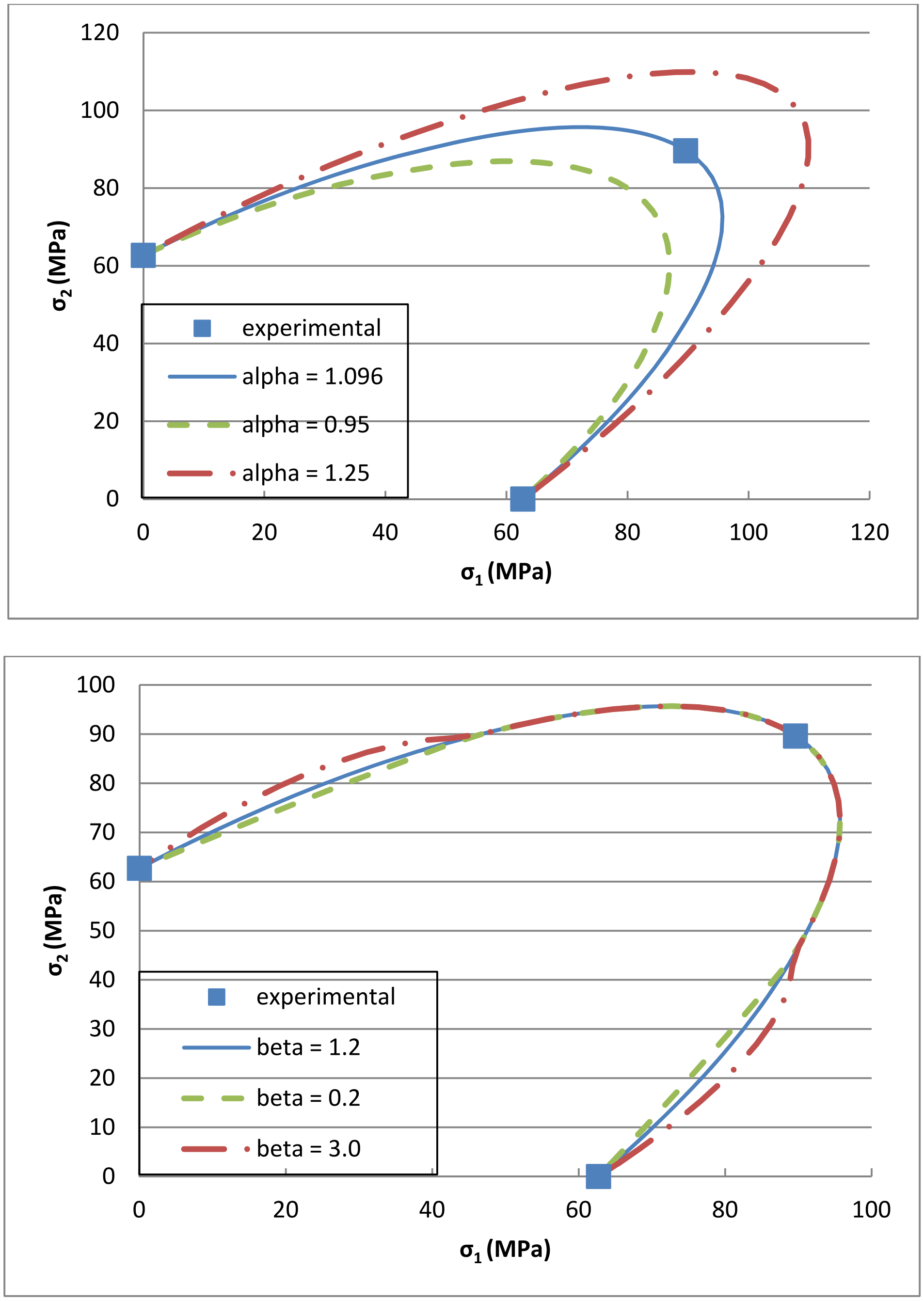

Fig. 6.9. Limit surface comparison for various values of α and β_2 parameters (Experimental data by Nelson et al., 1988)

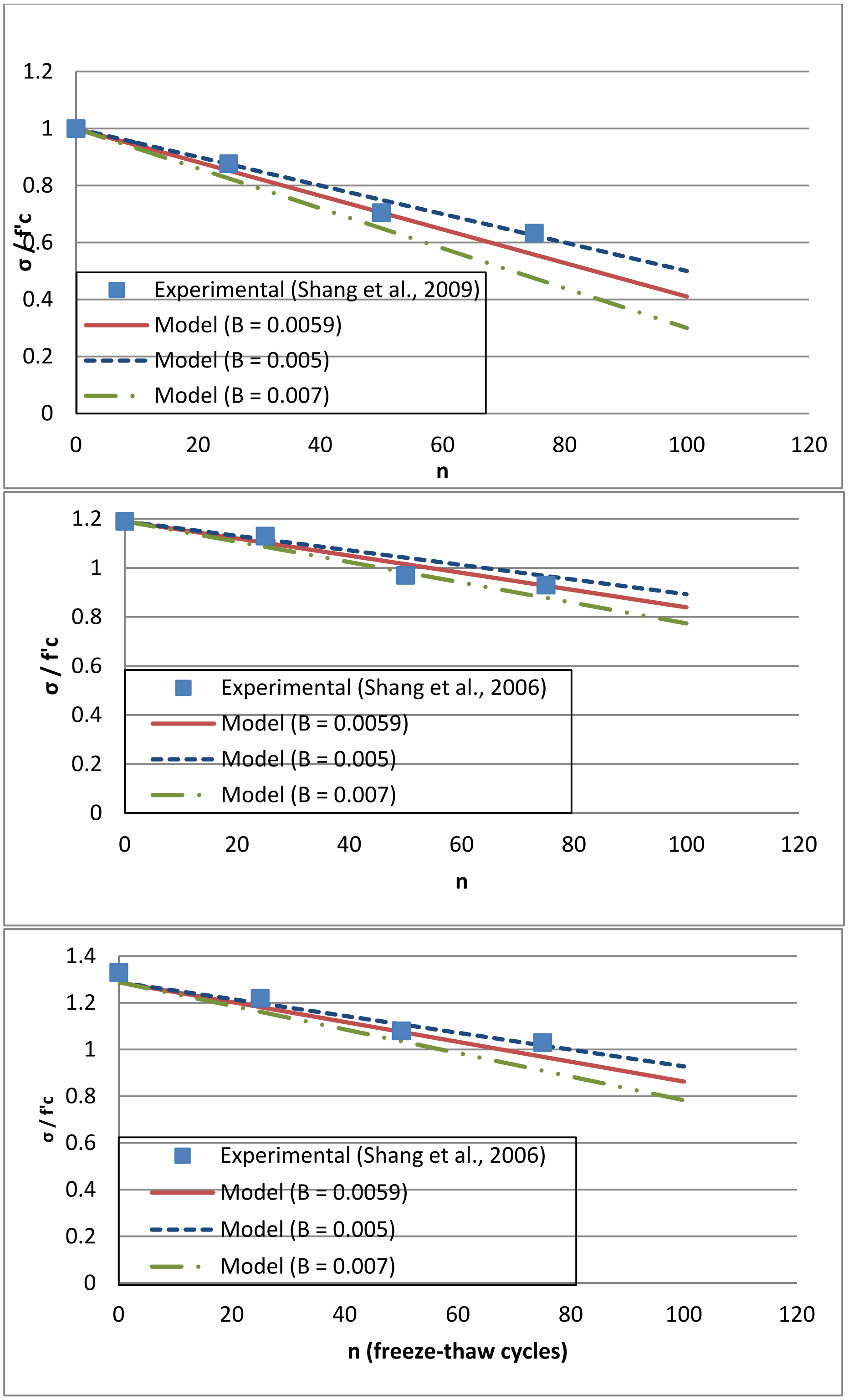

Fig. 6.10. S-N curves for uniaxial (top), equal-biaxial (middle), and 1:0.5 biaxial compression (bottom) with various values of *B*

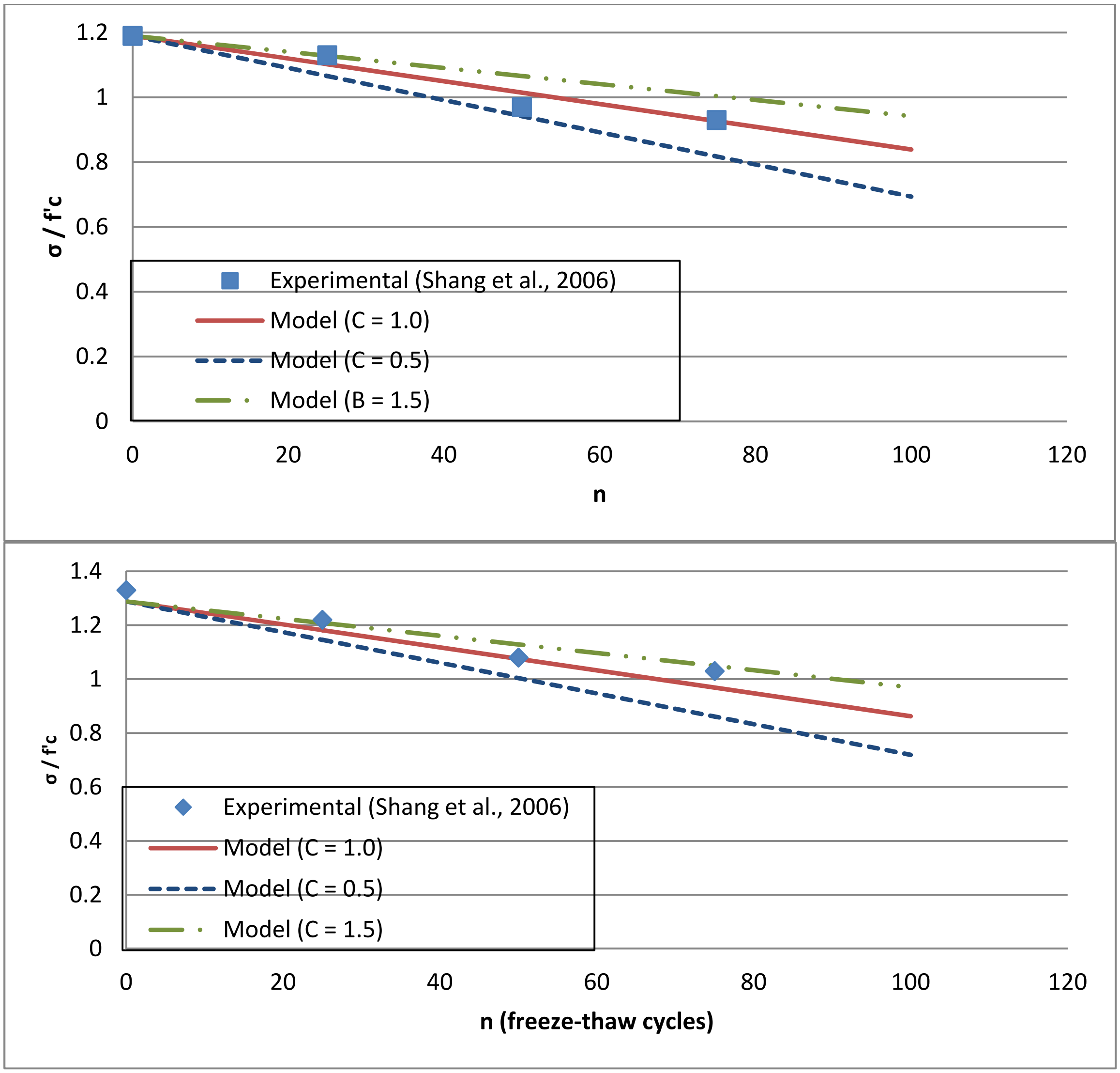

Fig. 6.11. S-N curves for equal-biaxial (top) and 1:0.5 biaxial compression (bottom) with various values of *C*

6.4. Conclusion

In this chapter the monotonic model which was introduced in Chapter 3 and 4 is extended to incorporate freeze-thaw damage. The bounding surface theory, which was similarly used to model fatigue processes, is used to develop residual strength surfaces that are the product of freeze-thaw damage occurring in concrete. This shows the versatility of the bounding surface approach once again. The softening function can take a form which will best represent the behavior which is being investigated (in this case, freeze-thaw processes). The original limit surface which corresponds with the undamaged material collapses in on itself as the number of freeze-thaw cycles increases. A numerical example is shown which demonstrates the new capabilities of the model and is compared with experimental results found by Shang et al. (2006 and 2009) and Nelson et al. (1988). The residual strength surfaces and S-N curves show good correlation with the experimental data. One weakness of the model is its inability to reproduce the increased ultimate strain of concrete that occurs with increasing freeze-thaw cycles. This issue may be addressed in future work.

The present study is considered a first step in developing a comprehensive model for freeze-thaw damage in concrete. Several key factors have not been considered in the present study. These include, the duration of freeze, the rate of freezing, and the degree of saturation. Although, it can be argued that the degree of saturation at the time of freezing could be reflected or modeled appropriately in the limit surface, nonetheless, the duration of freezing and the rate of freezing are important design considerations and need to be studies further and incorporated in this model in future studies.

REFERENCES

Alliche A. (2004). Damage model for fatigue loading of concrete. *International Journal of Fatigue*, 26, 915-921.

Au F. T. K., & Bai Z. Z. (2007). Two-dimensional non-linear finite element analysis of monotonically and non-cyclically loaded RC beams. *Engineering Structures*, *29*(11), 2921-2934.

Bahn B. Y. & Hsu C. T. T. (1998). Stress-strain behavior of concrete under cyclic loading. *ACI Materials Journal.* 95, No. 2, 178-193.

Chen Y., Ni J., Zheng P., Azzam R., Zhou Y., & Shao W. (2011). Experimental research on the behaviour of high frequency fatigue in concrete. *Engineering Failure Analysis*,18, 1848-1857.

Cordan W.A. (1966). Freezing and thawing of concrete – mechanisms and control, ACI Monograph No. 3. *ACI/Iowa State University Press.* Pg. 99.

Detwiler R.J., Dalgleish B.J., Williamson R.B. (1989). Assessing the durability of concrete in freezing and thawing. *ACI Materials Journal.* January-February: 29-35.

Dhir R. K. & Sangha C. M. (1974). Development and propagation of microcracks in plain concrete. *Materials Construction*. 7, 17.

Green S.J. & Swanson S.R. (1973). Static constitutive relations for concrete. *AFWL-TR-72-244*. Air Force Weapons Laboratory, Kirtland Air Force Base, New Mexico.

Hanson J. et al. (1997). Considerations for design of concrete structures subjected to fatigue loading. *ACI Committee 215*.

Hanson U. (1999). Damage development in woven fabric composites during tension-tension fatigue. *Journal of Composite materials*, 33, 614-639

Krajcinovic D. (1989). Damage mechanics. *Mech. Of Materials*. 8, 117.

Kupfer H., Hilsdorf H.K., Rusch H. (1969). Behaviour of concrete under biaxial Stress. *Proc. ACI*, 66, 656-666.

Lee M. K. & Barr B. I. G. (2002). An overview of the fatigue behaviour of plain and fibre reinforced concrete. *Cement and Concrete Composites*, *26*, 299-305.

Lee S. K., Song Y.C., Han S. H. (2004). Biaxial behavior of plain concrete of nuclear containment building. *Nuclear Engineering and Design*, *26*, 299-305.

Litewka A. & Debinski J. (2003). Load induced-oriented damage and anisotropy of rock-like materials. *International Journal of Plasticity*, *227*(2), 143-153.

Luccioni B.M. & Rougier V.C. (2005). A plastic damage approach for confined concrete. *Computers and Structures*, *83*(27), 2238-2256.

Mai S.H. et al. (2012). A continuum damage modeling of quasi-static fatigue strength of plain concrete. *International Journal of Fatigue*, 37, 79-85.

Mao, H. and Mahadevan S. (2002). Fatigue damage modeling of composite materials. *Composite Structures*, 58, 405-410.

Mehta P. K. & Monteir P. J. M. (1993). Concrete: structure, properties, and materials. (2nd ed.). Englewood Cliffs: Prentice-Hall, Inc.

Miao C, Mu R., Tian Q, Sun W. (2002). Effect of sulfate solution on the frost resistance of concrete with and without steel fiber reinforcement. *Cement and Concrete Research*. 32(31).

Nemat-Nasser S. & Horii H. (1982). Compression-induced nonplanar crack extension with application to splitting, exfoliation, and rockburst. *Journal of Geophysics*. *Res. 87*, 6805.

Ortiz M. (1985). A constitutive theory for the inelastic behavior of concrete. *Mechanics of Materials*, *4*(1), 67-93.

Papanikolaou V. K. & Andreas J. K. (2007). Confinement-sensitive plasticity constitutive model for concrete in triaxial compression. *International Journal of Solids and Structures*, *44*(21), 7021-7048.

Price W. H. (1951). Proceeding, ACI. Vol. 47, 417-432.

Schreyer H. L. (1983). A third-invarient plasticity theory for frictional materials. *Journal of Structural Mechanics*, 11(2), 177-196.

Shang H. S. & Song Y. P. (2006). Experimental study of strength and deformation of plain concrete under biaxial compression after freezing and thawing cycles. *Cement and Concrete Research*, 36, 1857-1864.

Shang H. S., Song Y. P., & Qin L. K. (2008). Experimental study on strength and deformation of plain concrete under triaxial compression after freeze-thaw cycles. *Building and Environment*, *43*, 1197-1204.

Shang H. S., Song Y. P., & Qin L. K. (2008). Behavior of Air-Entrained Concrete After Freeze-Thaw Cycles. *Acta Mechanica Solida Sinica*, *22(3)*, 261-266.

Shkolnik I. E. (2005). Influence of high strain rates on stress-strain relationship, strength and elastic modulus of concrete. *Cement and Concrete Composites*, *30*(10), 1000-1012.

Smith E.W. & Pascoe K.J. "Biaxial fatigue of a glass-fibre reinforced composite. Part 1: Fatigue and fracture behavior." *Mechanical Engineering Publications*. (1989): 367-396.

Song Y., Cao W., & Meng X. (2005). Fatigue properties of plain concrete under triaxial constant-amplitude tension-compression cyclic loading. *Journal of Shanghai University*, *9*(2), 127-133.

Subramaniam K. & Shah S. (2003). Biaxial tension fatigue response of concrete. *Cement and Concrete Composites*, 25, 617-623.

Thapa K. B. (2010). Dissertation: A new strain based damage model for structural concrete. Fargo: North Dakota State University.

Traina L.A. (1983). Experimental stress-strain behavior of a low-strength concrete under multiaxial states of stress. *AFWL-TR-82-92*, Air Force Weapons Laboratory, Kirtland Air Force Base, New Mexico.

Van Paepegem W. and Degriek (2003). Modeling damage and permanent strain in fiber-reinforced composites under in-plane fatigue. *Composites Science and Tech*, 63, 677-694.

Wen C. (2011). Dissertation: Bounding surface approach to the fatigue modeling of engineering materials with applications to woven fabric composites and concrete. Fargo: North Dakota State University.

Yang Z. (2004). Dissertation: Assessing cumulative damage in concrete and quantifying its influence on life cycle performance modeling. Purdue University.

Yazdani S. (1993). On a class of continuum damage mechanics. *International Journal of Damage Mechanics*, *2*, 162-176.

Yazdani S. & Karnawat S. (1996). A constitutive theory for brittle solids with application to concrete. *Internation Journal of Damage Mechanics*, *5*, 93-110.

Yazdani S. & Schreyer H. L. (1988). An anisotropic damage model with dilation for concrete. *Mechanics of Materials*, *7*, 231-244.

Yurtdas I., Burlion N., & Skoczylas F. (2004). Triaxial mechanical behavior of mortar: effects of drying. *Cement and Concrete Research*, *34*(7), 1131-1143.

APPENDIX

Matlab code for biaxial strength surface using the Yazdani model (1993) shown in Figure 3.3.

```
% Yazdani Schreyer Model
clear
% Model parameters
ft=3.5*10^6;
a=0.86;
w=0.0067;
B=1;
u=3.0;

% Load ratios, L=[zheta,gamma,mu]
L=[0;0;0];
n=1;
% Tension-compression loading
for z=1:-0.05:-1
    for g=1:-0.1:-1
        for m=1:-0.1:-1
           L=[z;g;m];
           % 1st term, sp=positive stress
           sp=L;
           if z<0
               sp(1,1)=0;
           end
           if g<0
               sp(2,1)=0;
           end
           if m<0
               sp(3,1)=0;
           end

           % sn=negative stress
           sn=L;
           if z>0
               sn(1,1)=0;
           end
           if g>0
               sn(2,1)=0;
           end
           if m>0
               sn(3,1)=0;
```

```
            end

            % 2nd term, t
            t=sn;
            if z>g & z>m
                t=t-z*[1;1;1];
            end
            if g>z & g>m
                t=t-g*[1;1;1];
            end
            if m>z & m>g
                t=t-m*[1;1;1];
            end

            % deviatoric stress
            dsn=1/3*[2*sn(1,1)-sn(2,1)-sn(3,1);-
sn(1,1)+2*sn(2,1)-sn(3,1);-sn(1,1)-sn(2,1)+2*sn(3,1)];
            if dsn(1,1)>0
                dsn(1,1)=B*dsn(1,1);
            end
            if dsn(2,1)>0
                dsn(2,1)=B*dsn(2,1);
            end
            if dsn(3,1)>0
                dsn(3,1)=B*dsn(3,1);
            end

            % unit pressure, P
            P=(L(1,1)+L(2,1)+L(3,1))/3;
            if min(t)>=0
                P=0;
            end

            L1=L;
            if min(t)>=0
                L1=0;
            end


x=(ft^2/((sp'*sp)+w*(sn'*t)*(t'*sn)/(t'*t)+2*w*dsn'*L+w*a*u*L1'*
L1-w*a*9*P^2))^.5;
            stress3(1,n)=x*L(1,1);
            stress3(2,n)=x*L(2,1);
            stress3(3,n)=x*L(3,1);
            n=n+1;
        end
    end
```

```
end
x3=stress3(1,:)/ft;
y3=stress3(2,:)/ft;
z3=stress3(3,:)/ft;
```